Metal Structures for Photonics and Plasmonics

A DISSERTATION
SUBMITTED TO THE FACULTY OF THE GRADUATE SCHOOL
OF THE UNIVERSITY OF MINNESOTA
BY

Jong Hyuk Park

IN PARTIAL FULFILLMENT OF THE REQUIREMENTS
FOR THE DEGREE OF
DOCTOR OF PHILOSOPHY

David J. Norris, Adviser

July, 2013

Acknowledgements

I am grateful to many people who have supported me over the last five years. This thesis would not have been completed without their help. I would first like to thank my adviser, David Norris. Owing to his guidance and support, I could enjoy research to solve scientific issues during my Ph.D. I feel very proud to work with such a creative adviser with professional insight.

I would like to appreciate Sang-Hyun Oh and Chris Leighton for the valuable discussions during our meetings which enrich my scientific knowledge. I thank my collaborators: Prashant Nagpal, Sang Eon Han, Kevin McPeak, Sriharsha Jayanti, Nathan Lindquist, Michael Manno, and Palak Ambwani for their significant contributions to my research. I wish to express gratitude to my group members who created enjoyable working environment: Moon Sung Kang, Ayaskanta Sahu, Stephan Kress, Yasmina Ries, Michael Heinrich, Florian Ott, Daniele Braga, Vincent Holmberg, David Kim, Stefan Meyer, and Pascale Bachmann for all their help in the lab and office.

I am indebted to my previous advisers in Korea, Jae Young Jho and Yong Soo Kang. They have been excellent mentors for me. I also appreciate my previous colleagues at KIST: Junkyung Kim, Soonho Lim, Min Park, and Sang-Soo Lee. I look forward to working together soon.

I am grateful to my friends in Minnesota: Keun Hyung Lee, Han Seung Lee, Soo-Hyung Choi, Sangwoo Lee, Jaewook Nam, Hyunwoo Kim, Jin-Oh Song, Pyung-Soo Lee, Sangwon Kim, and Dong Seong Cho for making my time in Minnesota exciting. I owe a great debt of gratitude to my best friends in Korea: Taek Sung Jung, Chul Eun Choi, Sunguk Lee, Jinho Ro, Taewook Yang, Jeong Gon Son, Hyunki Cho, and Man Jae Han. Thank you all the time.

My sister, Ji Yeon, and her husband, Jeong Wook, as well as my aunts and my cousins deserve a special thank for their care and consideration. Finally, I am always indebted to my dearest parents who have given me constant love throughout my life. Their encouragement made me what I am today.

Dedicated to my dearest family

Abstract

The goal of this thesis is to investigate metal structures for photonics and plasmonics and to provide theoretical and experimental bases for their practical applications. Engineered micro- and nanostructures of a metal can efficiently manipulate surface plasmon polaritons (SPPs) – coupled photon-electron waves propagating along a metal-dielectric interface. Since SPPs are able to contain both characteristics of light and charge, exploiting SPPs can lead to novel optical behaviors, for example, concentration of light below the optical diffraction limit, generating large electric-field enhancements in confined regions. This unique characteristic of SPPs has opened up new opportunities for photonic and plasmonic applications such as surface-enhanced spectroscopy, subwavelength waveguides, optical antennas, solar cells, and thermophotovoltaics. However, while many fabrication techniques have been developed and utilized to prepare metal structures, some applications would still benefit from improved methods because SPPs are extremely sensitive to inhomogeneities on a metallic surface arising from roughness, impurities and even grain boundaries of a metal. To minimize the surface inhomogeneities of the metal structures and thus to exploit SPPs effectively, we introduced novel fabrication methods. First, the template-stripping method was employed to obtain high-quality silver films for SPPs in the visible wavelengths. The template-stripped films showed very smooth surfaces, leading to the improved dielectric function with high electrical conductivity and low optical loss. The dielectric function of the template-stripped films was compared with that of conventional films. As a result, the relation between the surface roughness and dielectric function of metal films could be derived. As another approach to reduce the inhomogeneities on a metal surface, we prepared single-crystalline silver films via epitaxial growth. Under controlled deposition conditions, single-crystalline silver films exhibited ultrasmooth surfaces with a root mean square roughness of 0.2 nm. Moreover, we observed that the absence of the grain boundaries can lead to an increase in SPP propagation length as well as precise patterning for metal structures. Beyond noble metals, we then introduced an effective route to obtain smooth patterned structures of refractory metals, semiconductors, and oxides via template

stripping. The smooth structures of such materials can be favorable for many applications including thermal emitters, metamaterials, solar absorbers, and photovoltaics. We demonstrated that a variety of desired materials deposited on a thin noble metal layer can be peeled from silicon templates. After removing the noble metal layer, the revealed surfaces had very small roughness. This approach could easily reproduce structures via reuse of templates, leading to a low-cost and high-throughput process in micro- and nanofabrication. Finally, we showed that thermal excitation of SPPs in patterned metallic structures can provide tailored thermal emission. Typically, SPPs on metal structures are generated by using an optical source and then re-radiated as light, of which the emission angle and wavelength are determined by the geometry of the metal structures. However, since thermal energy can be another excitation source to create SPPs, heating of properly designed metal structures can result in tailored thermal emission. We experimentally demonstrated that at high temperatures, tungsten films with bull's-eye patterns exhibit tailored thermal emission with a unidirectional and monochromatic beam. In addition, since the thermal stability of the structures could be enhanced by coating with a protective oxide layer on the metal surface, the bull's-eye structures can be utilized as a novel radiation source. Overall, we pursued efficient engineering of SPPs in metal structures and development of improved fabrication methods for the metal structures. We believe that these results will promote the practical application of SPPs for electronic, photonic and plasmonic devices.

Table of Contents

List of Tables

List of Figures

Chapter 1.
Introduction

Metal is a very important material for mankind. It is solid at room temperature with excellent properties such as hardness, ductility, malleability, reflectivity of light, and electrical and thermal conductivity.[1] Humans have achieved revolutionary breakthroughs since the Stone Age by means of using different metals upon entering the Bronze and the Iron Ages. Recently, the advancement in modern science has opened a large variety of novel opportunities for utilizing metals. The discovery of the electron[2] and the development of the Drude model,[3] for example, led to the use of metals as electrical materials. Understanding of the photoelectric effect[4] and thermionic emission[5] stimulated scientists to investigate metals for photonic applications. Moreover, plasmonics, an emerging research topic in nanoscience, proved that metallic structures allow engineering of light to interact with charges in the metal.[6-7]

The unique electronic, photonic and plasmonic characteristics of metals are based on the delocalized states of the electrons in the material.[8-9] While all electrons in dielectric materials are tightly bound to the atoms, the electrons in metals can readily escape from the atoms and become free to move within the material. In other words, a metal can be treated as a fixed array of atoms in a sea of free electrons.[3] Due to the contribution of the free electrons, metals are able to transmit electricity and heat easily and thereby exhibit high electrical and thermal conductivities. Furthermore, the delocalized nature of electrons in metals results in a dielectric function, which describes the polarizability of the material in response to an applied electric field, that is very different from that of dielectric materials. Due to the phase difference between the applied field and the response of the material, the dielectric function can be expressed as a complex function of the field frequency.[8-9]

Non-absorbing dielectric materials typically have dielectric functions with a positive real part and a negligible imaginary part over a wide range of frequencies. This

implies that polarization of dielectric materials in response to an external electric field is nearly instantaneous. On the contrary, the dielectric functions of metals are strongly dependent on the frequency of the applied electric field.[10-11] Above the plasma frequency of metals, their dielectric functions show the same behavior as those of dielectric materials. However, below the plasma frequency, the dielectric functions of metals have a negative real part and a positive imaginary part. Also, if the applied field frequency is decreased, the real part becomes more negative while the imaginary part becomes more positive.

Interesting optical behaviors of metals are observed below their plasma frequency where the real part of the dielectric function is negative. Light within this frequency range including visible light cannot penetrate through the metal but is totally reflected from its surface. This explains why most metals have such shiny colors. Moreover, only when the real part is more negative than -1, surface plasmon polaritons (SPPs), hybrid photon-electron waves propagating along metallic surfaces, can be excited.[6-7] Since manipulating SPPs allows concentration of light below the optical diffraction limit and generation of large electric-field enhancements in confined regions, many scientists have investigated SPP engineering in structured metals.[12-15] The quality of any metallic surface can be indicated by its SPP propagation length, the distance over which the intensity of SPPs decreases to 1/e. An increase in SPP propagation length can lead to desirable engineering of SPPs and thereby the improved performance of plasmonic devices. However, the SPP propagation length in metals is restricted by the energy loss due to ohmic heating within the material.[6-7] Also, inhomogeneities of metallic surfaces arising from surface roughness and grain boundaries act as scattering centers which hinder the propagation of SPPs.

In this thesis, metals with enhanced SPP propagation length are pursued. SPPs are highly confined at metallic surfaces because SPP intensity decays exponentially from the surfaces.[6-7] In other words, the characteristics of SPPs are predominantly determined by only a few top surface layers of the metal. Therefore, we introduce effective approaches to improve the surface layers and enhance the SPP propagation length. First, the roughness of metallic surfaces was decreased significantly by using a fabrication

approach known as template stripping. The smooth surfaces lead to a reduction of both ohmic loss and SPP scattering during the propagation. Second, the scattering of electrons and SPPs occurring at grain boundaries of a metal were avoided completely by forming single-crystalline metallic films. We demonstrate that metallic structures fabricated via these approaches can increase the SPP propagation length and provide a route to successful manipulation of SPPs. These results will promote practical applications of plasmonic devices including subwavelength waveguides,[16] optical antennas,[17] solar cells,[18] and thermophotovoltaics.[19-20]

1.1 Motivation

Changing energy from one form to another is an important step in applying physical sciences to practical use.[21] The desirable form of energy can be obtained by using energy-conversion devices. However, considering all the demands for energy cost reduction, improvements on the efficiency of current energy-conversion devices are necessary. For example, the energy-conversion efficiencies of an incandescent lamp and a gas engine are only 3%[22] and 30%[23], respectively. The unusable energy mostly changes into thermal energy and dissipates. Thus, if the wasted thermal energy can be recycled, considerable improvement on the overall energy conversion efficiency will be achieved.

One strategy of recycling thermal energy is by using thermophotovoltaics,[24-26] a thermal emitter and a photovoltaic device in series. The thermal emitter converts absorbed heat into radiant energy which can be employed as a light source for the photovoltaic device (Figure 1.1a). This would enable one to generate electricity from the wasted thermal energy. However, simply utilizing the natural thermal emission by itself may not be the most effective method. This is because natural thermal emission features a broad emission angle and wavelength range.[27-28] Due to the non-directionality of natural thermal emission, only a small fraction of light is collected by the photovoltaic device (Figure 1.1a). Also, thermal emission with a wavelength longer than the bandgap of the

photovoltaic device would not excite any electrons, whereas thermal emission with a wavelength shorter than the bandgap would not be fully converted into electricity (Figure 1.1b). On the contrary, an ideal thermal emitter with tailored emission angle and wavelength can optimize electron generation in the photovoltaic device. Therefore, well-controlled thermal emission with a narrow emission angle and wavelength range is an essential requirement to enhance energy-conversion efficiency.

Exploiting SPPs with periodic metal structures is a promising solution to achieve simultaneous control of both the emission angle and wavelength in thermal emission. In this strategy, the energy conversion from thermal energy to radiant energy can be done by the following procedure. First, thermal energy generates SPPs in metallic structures. Then, these SPPs propagate along the metallic surfaces. During the propagation, the SPPs are converted into photons, of which the emission angle and wavelength are determined by the geometry of the metallic structure. In summary, if thermally excited SPPs are desirably manipulated via metallic structures, tailored thermal emission can be obtained. This research will have significant implications for efficient thermal-energy conversion and energy recycling.

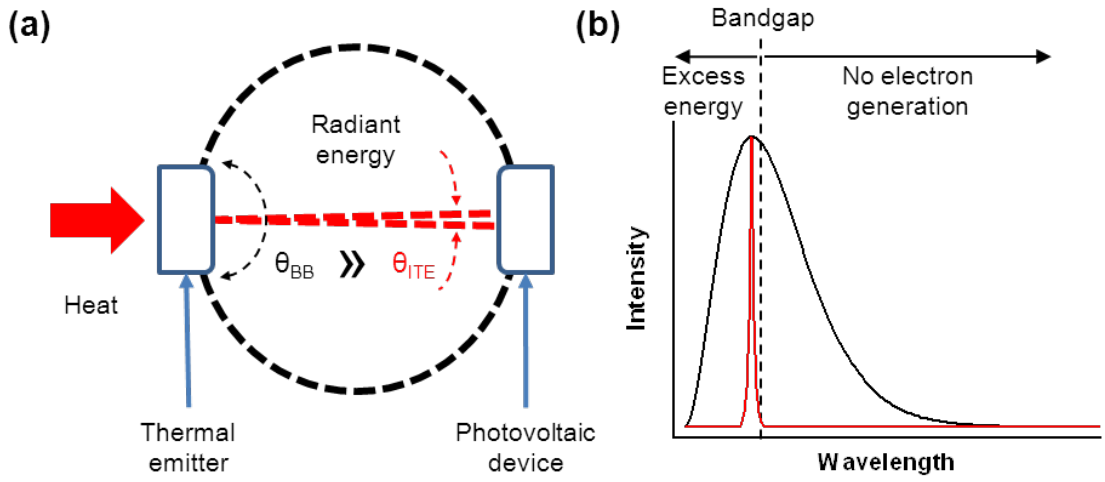

Figure 1.1 Energy recycling with thermal emission from a black body (black) and an ideal thermal emitter (red). Here, the black body radiation denotes natural thermal emission without any manipulation. An ideal emitter shows optimized emission (a) angle and (b) wavelength range to generate electricity in a photovoltaic device.

1.2 Thesis Overview

This thesis offers a fundamental understanding of SPP engineering via periodic metal structures, particularly focused on (i) the influence of inhomogeneities on the metallic surfaces on the SPP propagation length, (ii) novel fabrication methods for improved metallic structures, leading to a successful manipulation of SPPs, and (iii) tailored thermal emission from the metallic structures. Accordingly, the remaining chapters are organized as follows.

In Chapter 2, the relation between the surface roughness and the dielectric function of metallic films is discussed. This chapter has been published as Jong Hyuk Park, Prashant Nagpal, Sang-Hyun Oh, and David J. Norris, "Improved Dielectric Functions in Metallic Films Obtained via Template Stripping," *Applied Physics Letters* **2012**, *100*, 081105 (DOI: 10.1063/1.3687910). In this work, we compare the dielectric functions of silver surfaces obtained via thermal evaporation with those obtained with template stripping. Ellipsometry measurements show that the smoother template-stripped surfaces exhibit effective dielectric functions with a more negative real component and a smaller imaginary component, implying higher conductivity and less energy loss, respectively. These results agree with the relation between dielectric function and surface roughness derived from combining the effective-medium model and the Drude-Lorentz model. The improvement in the effective dielectric properties shows that metallic films prepared via template stripping can be favorable for applications in electronics, nanophotonics, and plasmonics.

In Chapter 3, the influences of grain boundaries of a metal on the dielectric function and SPP propagation length are investigated. This chapter has been published as Jong Hyuk Park, Palak Ambwani, Michael Manno, Nathan C. Lindquist, Prashant Nagpal, Sang-Hyun Oh , Chris Leighton, and David J. Norris, "Single-Crystalline Silver Films for Plasmonics," *Advanced Materials* **2012**, *24*, 3988 (DOI: 10.1002/adma.201200812). In this work, we demonstrate a simple route to flat, large-area, single-crystalline films for plasmonics by sputter deposition of silver onto mica substrates at elevated temperatures.

We show that the absence of grain boundaries significantly reduces ohmic losses and scattering, leading to improved dielectric properties and increased propagation lengths for SPPs. Further, the films allow more precise patterning of high-quality nanostructures.

In Chapter 4, a novel fabrication method for smooth structures consisting of refractory metals, semiconductors, and oxides beyond noble metals is described. The main portion of this chapter has been prepared for submission as Jong Hyuk Park, Prashant Nagpal, Kevin M. McPeak, Nathan C. Lindquist, Sang-Hyun Oh, and David J. Norris, "Fabrication of Smooth Patterned Structures of Refractory Metals, Semiconductors, and Oxides via Template Stripping." In this work, we offer an effective route to prepare smooth patterned structures of refractory metals, semiconductors, and oxides via template stripping. We demonstrate that a variety of desired materials can be deposited on a thin layer of noble metal and then peeled from silicon templates. This allows patterning of technologically important materials, such as tungsten and indium tin oxide, which is difficult to achieve with conventional methods. In addition, this approach can easily reproduce structures via the reuse of templates, leading to a low-cost and high-throughput process in micro- and nanofabrication.

In Chapter 5, tailored thermal emission via manipulating SPPs with patterned metal structures is studied. The main portion of this chapter has been prepared for submission as Jong Hyuk Park, Sang Eon Han, Prashant Nagpal, and David J. Norris, "Tailored Thermal Emission from Metallic Bull's Eye Structures." In this work, we prepare a tungsten film with bull's-eye patterns, a series of circular concentric grooves. When the patterned films are heated to 900 ^{o}C, the bull's-eye patterns generate monochromatic directional beams of light with a peak wavelength of 3.532 micrometer which is similar to the periodicity of the structures. Also, we can enhance the thermal stability of the structures via a HfO_2 coating prepared by atomic layer deposition. We prove that a simple thermal process, that is heating periodic metal structures, can result in tailored thermal emission. This ability can play an important role in effective exploitation of thermal energy.

1.3 References

[1] Encyclopedia Britannica, http://www.britannica.com.

[2] J. J. Thomson, "Cathode Rays," *The Electrician* **1897,** *39*, 104.

[3] P. Drude, "Zur Elektronentheorie der Metalle," *Annalen der Physik* **1900,** *306*, 566.

[4] A. Einstein, "Über einen die Erzeugung und Verwandlung des Lichtes betreffenden heuristischen Gesichtspunkt," *Annalen der Physik* **1905,** *322*, 132.

[5] O. W. Richardson, "The Emission of Electrons from Tungsten at High Temperatures: An Experimental Proof That the Electric Current in Metals Is Carried by Electrons," *Science* **1913,** *38*, 57.

[6] H. Raether, *Surface Plasmons on Smooth and Rough Surfaces and on Gratings*. Springer-Verlag: Berlin, 1988.

[7] W. L. Barnes, A. Dereux, T. W. Ebbesen, "Surface Plasmon Subwavelength Optics," *Nature* **2003,** *424*, 824.

[8] C. Kittel, *Introduction to Solid State Physics*. Wiley: New York, 1966.

[9] N. W. Ashcroft, N. D. Mermin, *Solid State Physics*. Saunders College: Philadelphia, 1976.

[10] E. D. Palik, *Handbook of Optical Constants of Solids*. Academic Press: Orlando, 1985.

[11] M. J. Weber, *Handbook of Optical Materials*. CRC Press: Boca Raton, 2003.

[12] E. Ozbay, "Plasmonics: Merging Photonics and Electronics at Nanoscale Dimensions," *Science* **2006,** *311*, 189.

[13] H. A. Atwater, "The Promise of Plasmonics," *Sci. Am.* **2007,** *296*, 56.

[14] A. Polman, "Applied Physics: Plasmonics Applied," *Science* **2008,** *322*, 868.

[15] M. L. Brongersma, V. M. Shalaev, "The Case for Plasmonics," *Science* **2010,** *328*, 440.

[16] S. I. Bozhevolnyi, V. S. Volkov, E. Devaux, J. Y. Laluet, T. W. Ebbesen, "Channel Plasmon Subwavelength Waveguide Components Including Interferometers and Ring Resonators," *Nature* **2006,** *440*, 508.

[17] P. Muhlschlegel, H. J. Eisler, O. J. Martin, B. Hecht, D. W. Pohl, "Resonant Optical Antennas," *Science* **2005,** *308*, 1607.

[18] H. A. Atwater, A. Polman, "Plasmonics for Improved Photovoltaic Devices," *Nat. Mater.* **2010,** *9*, 205.

[19] S. E. Han, *Ph.D. Thesis: Thermal Emission Control with Periodic Microstructures*. University of Minnesota: Minneapolis, 2009.

[20] P. Nagpal, *Ph.D. Thesis: Metal Photonics and Plasmonics for Energy Generation*. University of Minnesota: Minneapolis, 2009.

[21] D. Y. Goswami, F. Kreith, *Energy Conversion*. Taylor & Francis: Boca Raton, 2008.

[22] T. J. Keefe, *The Nature of Light*. http://www.ccri.edu/physics/keefe/light.htm, 2007.

[23] M. P. Boyce, *Gas Turbine Engineering Handbook*. Gulf Professional Pub.: Boston, 2006.

[24] M. A. Green, *Third Generation Photovoltaics: Advanced Solar Energy Conversion*. Springer: 2005.

[25] T. Bauer, *Thermophotovoltaics: Basic Principles and Critical Aspects of System Design*. Springer-Verlag: Berlin, 2011.

[26] T. J. Coutts, M. C. Fitzgerald, "Thermophotovoltaics," *Sci. Am.* **1998,** *279*, 90.

[27] C. Kittel, H. Kroemer, *Thermal Physics*. W. H. Freeman: San Francisco, 1980.

[28] F. Reif, *Fundamentals of Statistical and Thermal Physics*. McGraw-Hill: New York, 1965.

Chapter 2.

Improved Dielectric Functions in Metallic Films Obtained via Template Stripping[*]

The template-stripping method can offer smooth patterned metals for plasmonics and metamaterials. While reduced surface roughness through this approach has previously been demonstrated, its ability to improve the dielectric function and electrical resistivity of the obtained metals has not been thoroughly investigated. Here, we report the effect of template stripping on the physical properties of silver films. Films were prepared with different surface roughness using conventional metal deposition and template stripping. The dielectric functions of the resulting films were compared using ellipsometry. The template-stripped surfaces with the smallest roughness exhibited dielectric functions with the largest negative real component and the smallest imaginary component. This indicates that the template-stripped surface will exhibit higher conductivity and less optical loss. These results agree with the relation between dielectric function and surface roughness derived from combining the effective-medium model and the Drude-Lorentz model. The total electrical resistivity of the template-stripped films, even including the contribution due to electron scattering at surfaces, is close to that of bulk silver, while conventionally-deposited surfaces have much higher values. As a result of the improved surface properties, the propagation length of surface plasmon polaritons on the template-stripped surfaces is estimated to be 10 times longer than the conventionally-deposited surfaces.

[*] This chapter is reproduced with permission from Jong Hyuk Park, Prashant Nagpal, Sang-Hyun Oh, and David J. Norris, "Improved Dielectric Functions in Metallic Films Obtained via Template Stripping," *Applied Physics Letters* **2012**, *100*, 081105 (DOI: 10.1063/1.3687910).

2.1 Introduction

The optical characteristics of metals play an important role in plasmonics.[1-2] In this field, devices are designed to exploit surface plasmon polaritons (SPPs), which are hybrid electron-photon waves that propagate along a metal interface.[1] In most devices, the losses for the SPPs should be minimized for optimal performance. This occurs for metals with high conductivity and low optical absorption, properties that are related to the dielectric function. Therefore, the dielectric characteristics of the metal are critical for many plasmonic applications, including molecular sensing, subwavelength waveguides, and solar cells.[3-5]

To enhance SPP propagation, the dielectric function should have: (i) a negative real component with a magnitude that is as large as possible and (ii) an imaginary component that is as small as possible. It is often assumed that metallic films of the same material will exhibit the same dielectric function. In other words, given a metallic film with a specified purity, it is assumed that the dielectric function is an intrinsic material property. In reality, variations in tabulated values exist.[6-8] Moreover, for Ag, a heavily studied plasmonic metal, measured values are rarely as good as those reported by Johnson and Christy,[6] which are nevertheless frequently assumed for theoretical simulations. Thus, simple approaches are needed to optimize the dielectric properties of thin films for a given material.

Here, we show such an approach. The effective dielectric properties of metallic films are strongly affected by their surface morphology due to their small skin depth. Since light interacts mainly with the top layers of the metal, nanometer-scale roughness changes the interaction of light with metallic surfaces. Moreover, electron scattering on the surface also affects the optical losses. Thus by decreasing the roughness of the film, its effective dielectric function can be improved. Since smooth films are also desirable to avoid scattering of SPPs as they propagate,[1] our results add another motivation to decrease roughness. Namely, smooth surfaces can also enhance plasmonic device performance by improving the effective dielectric properties of the film itself.

2.2 Results and Discussion

To obtain smooth metallic surfaces, we used a simple technique known as template stripping.[9] A noble-metal film is first deposited on a flat substrate (*e.g.*, polished silicon) and then covered with an epoxy adhesive as a backing layer. If the adhesion between the noble metal and the substrate is weak, the backing layer along with the metallic film can be easily peeled from the substrate. The metallic surface that is exposed replicates the smooth interface of the flat substrate. Consequently, surface roughness as low as a few angstroms can be obtained. In addition to flat films, more recently, this same approach was extended to obtain ultrasmooth patterned films for plasmonics.[10-12] Furthermore, some of these results suggested that the dielectric functions of the template-stripped films were improved.[11, 13]

To perform a more detailed experimental analysis, we prepared a series of 200-nm-thick Ag films on Si wafers by thermal evaporation. The deposition rate and substrate temperature were varied to generate Ag surfaces with different roughness. We then compared the "conventional" top surfaces with template-stripped surfaces exposed from the same films. The latter were obtained by curing an epoxy backing layer at 150 °C for 1 h and then detaching the films from the substrates. Figure 2.1 shows the surface morphology of six interfaces, observed using atomic force microscopy (AFM). As previously reported,[9-13] the template-stripped surfaces had much lower roughness than the conventional ones. Smoother surfaces were also obtained at slower deposition rates (0.01-0.02 nm/s), presumably because the grains could then distribute more uniformly. Interestingly, the template-stripped surfaces also became smoother with increased substrate temperature, while the conventional surfaces showed the opposite trend (Table 2.1). This can be attributed to more rapid diffusion of Ag on the substrate at higher temperatures. As the template-stripped interface is geometrically confined by the substrate, the diffusion removes the grain boundaries and defects, thereby reducing the surface roughness (figure 2.1d and 2.1f). In contrast, the conventional surface undergoes grain growth without confinement resulting in increased surface roughness (figure 2.1c

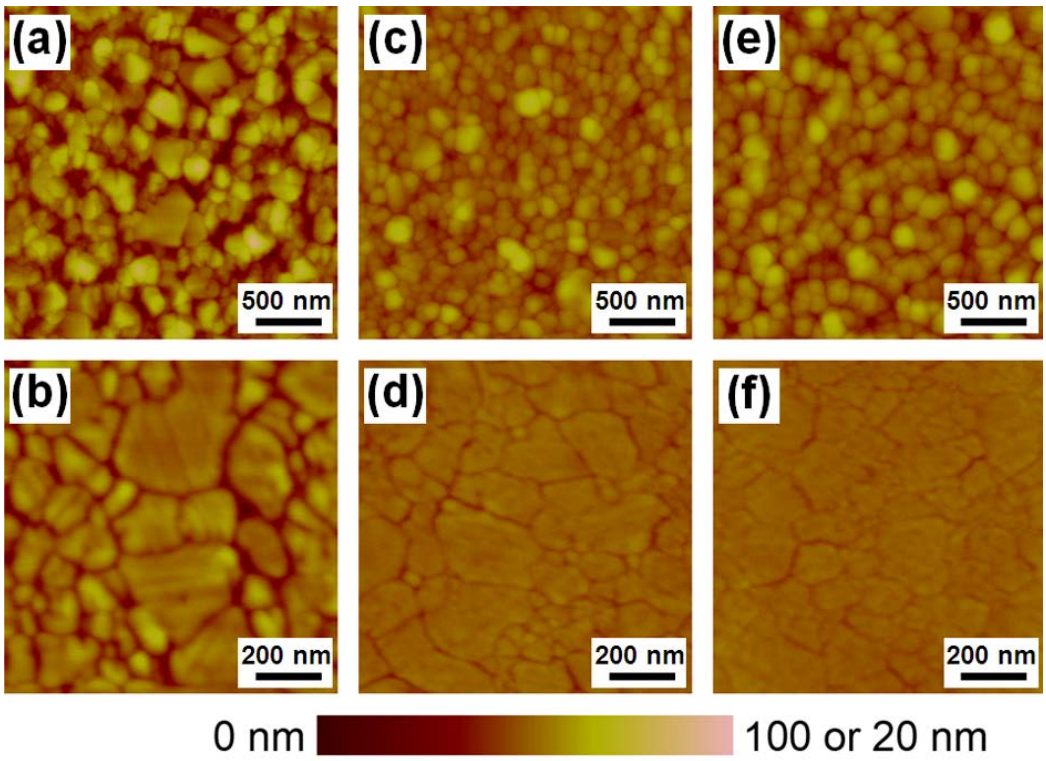

Figure 2.1 Atomic force micrographs of conventional evaporated Ag surfaces (a, c, and e) and template-stripped Ag surfaces (b, d, and f). The height scale bars are 0 to 100 nm (a, c, and e) and 0 to 20 nm (b, d, and f). The letter on each panel corresponds to the interface label in Table 2.1.

Table 2.1 Preparation conditions for three Ag evaporated films. The surface properties of the six interfaces used in the measurements, labeled (a) through (f), are listed, including the measured RMS roughness, the RMS height Δ and the lateral correlation length ξ extracted from a Gaussian fit of the power spectral density function to atomic force micrographs, and the electrical surface resistivity ρ_s estimated from Δ and ξ. The roughness of the Si wafer was 0.17 nm, and the bulk resistivity ρ_b of Ag at 295 K is 1.61 μΩcm.

Interface	Deposition rate (nm/s)	Substrate temperature (°C)	Surface type	Measured roughness (nm)	Δ (nm)	ξ (nm)	ρ_s (μΩcm)
(a)	0.1-0.2	25-30	Conventional	10.9 ± 0.37	15.1	104	3.54
(b)			Template-stripped	1.34 ± 0.12	2.62	84.1	0.13
(c)	0.01-0.02	25-30	Conventional	5.53 ± 0.43	8.84	106	1.19
(d)			Template-stripped	0.46 ± 0.03	1.23	42.2	0.06
(e)	0.01-0.02	75-80	Conventional	6.38 ± 0.28	9.32	112	1.25
(f)			Template-stripped	0.35 ± 0.02	0.96	40.1	0.04

and 2.1e). Table 2.1 summarizes the preparation conditions and surface parameters for each of our interfaces, including the root mean square (RMS) height (Δ) and the lateral correlation length (ξ) extracted from a Gaussian fit of the power spectral density function to the AFM data.[1, 11]

We then used a multi-angle-spectroscopic ellipsometer (V-VASE, J. A. Wollam Co.) to quantify the dielectric function of these Ag surfaces. Polarized light was scanned in the wavelength range from 450 to 750 nm, with an interval of 1 nm, and the reflected light from each sample was analyzed at incidence angles of 65, 70, and 75°. We extracted the experimental dielectric functions by assuming a two-layer model (air and Ag) with a perfectly flat interface and solving the Fresnel equations with numerical iteration to a mean square error less than 0.5.[14] Although it is well known that even nanometer-scale roughness can cause errors in the ellipsometric determination of dielectric functions,[15-17] this roughness is often neglected in practice. In this case, ellipsometry yields the effective dielectric function of the film. Figure 2.2 shows such results for our Ag samples. The standard deviations for the real part ε_1^{exp} and the imaginary part ε_2^{exp} of the effective dielectric functions were estimated as ±0.05 and ±0.01, respectively. As seen in the data, ε_1^{exp} (figure 2.2a) and ε_2^{exp} (figure 2.2b) become more negative and smaller, respectively, as the roughness decreases. The larger negative ε_1^{exp} suggests higher conductivity and the smaller ε_2^{exp} relates to less absorption.

To compare these results with expected values, we calculated the effective dielectric function using a simple effective-medium model.[16-17] Because the scale of the roughness is much smaller than the optical wavelength, the roughness can be included by treating the film as a homogeneous layer containing both Ag and air components. Assuming the Ag films are two-dimensionally isotropic, the effective dielectric function can be estimated as[16]

$$\varepsilon^{em} = \frac{\varepsilon^{air}\varepsilon^{Ag} + \varepsilon^{em}(f^{air}\varepsilon^{air} + f^{Ag}\varepsilon^{Ag})}{\varepsilon^{em} + (f^{Ag}\varepsilon^{air} + f^{air}\varepsilon^{Ag})}, \qquad (2.1)$$

where ε^{air}, ε^{Ag}, and ε^{em} are the dielectric functions of the air, Ag, and the effective medium (the Ag film with roughness), and f^{air} and f^{Ag} are the volume fractions of the

air and Ag, respectively. If we treat the roughness as a two-dimensional sinusoid and we assume an optical interaction depth of 100 nm, f^{Ag} values for our interfaces are 0.870, 0.924, 0.934, 0.984, 0.995, and 0.996, increasing with decreasing roughness.

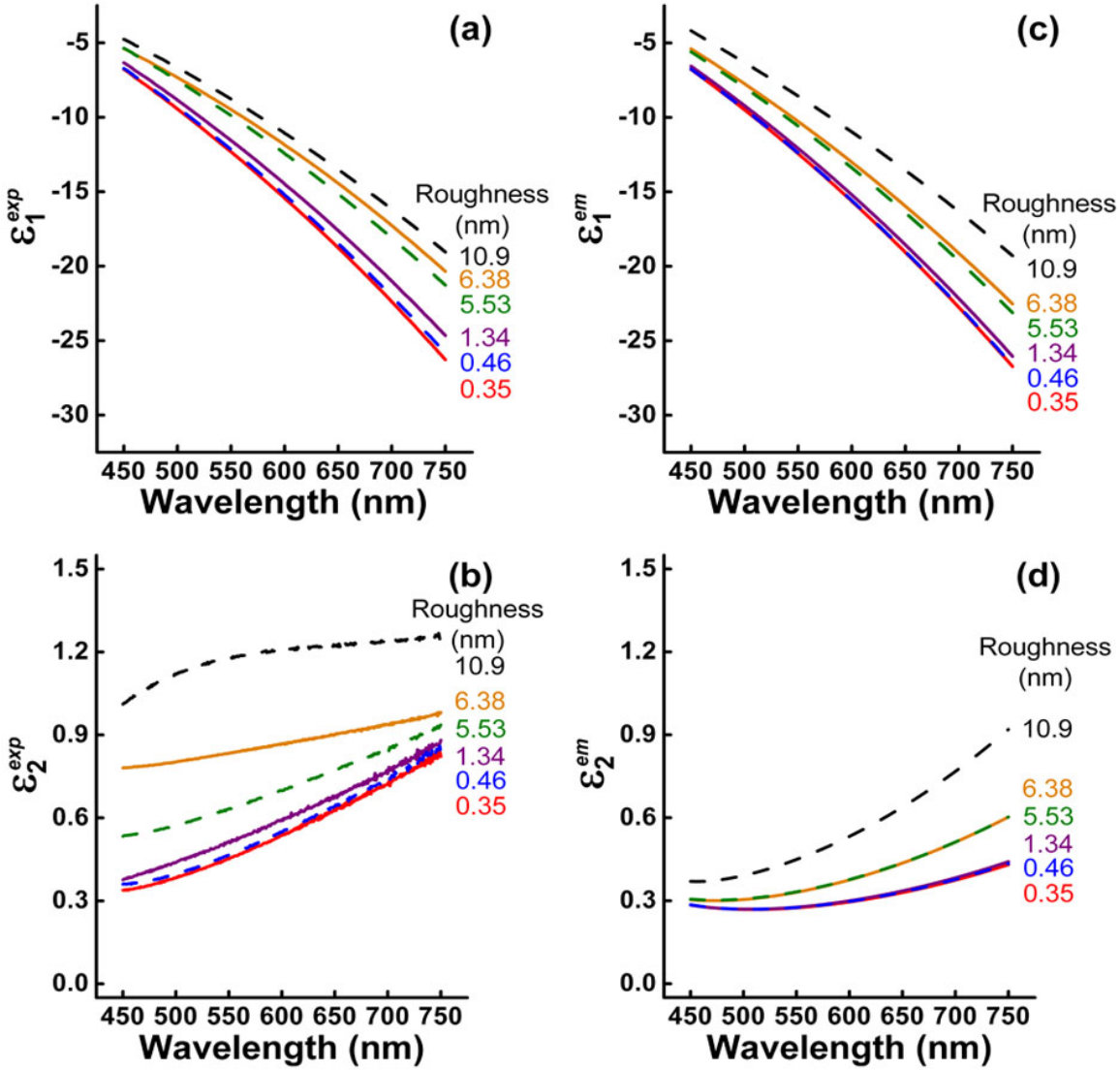

Figure 2.2 The measured real (a) and imaginary (b) components and the predicted real (c) and imaginary (d) components of the effective dielectric function for Ag films with different surface roughness. The standard deviations of ε_1^{exp} and ε_2^{exp} were estimated as ±0.05 and ±0.01, respectively. The legends indicate the RMS roughness for the experimental films. For the predictions, the RMS heights Δ and the lateral correlation lengths ξ extracted from a Gaussian fit of the power spectral density function to atomic force micrographs of the corresponding films were used. The predictions utilize a combination of the effective medium and Drude-Lorentz models. Drude-Lorentz parameters that fit data from Johnson and Christy (reference 6) were used.

However, to proceed with Eq. (2.1) we also need ε^{Ag}. For this, the Drude-Lorentz model gives[18]

$$\varepsilon^{Ag}(\omega)=\varepsilon_1^{Ag}(\omega)+i\varepsilon_2^{Ag}(\omega)=\left[\varepsilon_\infty^{Ag}-\frac{\left(\omega_p^{Ag}\right)^2}{\omega^2+i\omega\gamma_p^{Ag}}\right]+\left[\sum_{j=1}^{5}\frac{s_j\omega_j^2}{\omega_j^2-\omega^2-i\omega\gamma_j}\right], \tag{2.2}$$

where ω is the frequency, ε_∞^{Ag} is the dielectric constant of Ag at infinite frequency, ω_p^{Ag} is the plasma frequency of Ag, and γ_p^{Ag} is the damping constant of Ag for the Drude (free-electron) term. For the Lorentz (bound-electron) term we include five oscillators with frequency ω_j, strength s_j, and damping constant γ_j.[18] γ_p^{Ag} can be rewritten as $\rho ne^2/m_e$ where n is the electron density, e is the electron charge, m_e is the effective electron mass, and ρ is the electrical resistivity.[19] Since ρ can be affected by electron scattering at the surface of the Ag, we can write ρ as the sum of a bulk (ρ_b) and surface (ρ_s) resistivity.[20-21] ρ_s can then be approximated as[20]

$$\rho_s=\frac{3\pi\hbar}{e^2dk_f}\times\frac{\Delta^2}{\xi}\ \text{for}\ k_f\xi>>5, \tag{2.3}$$

where $\hbar$ is Planck's constant, d is the film thickness, and k_f is the Fermi wave vector. Consequently, for visible frequencies where $\omega>>\gamma_p^{Ag}$, ε_1^{Ag} and ε_2^{Ag} are given by

$$\varepsilon_1^{Ag}(\omega)\approx\varepsilon_\infty^{Ag}-\frac{\left(\omega_p^{Ag}\right)^2}{\omega^2}+\mathrm{Re}\left[\sum_{j=1}^{5}\frac{s_j\omega_j^2}{\omega_j^2-\omega^2-i\omega\gamma_j}\right]\ \text{and} \tag{2.4}$$

$$\varepsilon_2^{Ag}(\omega)\approx\frac{\left(\omega_p^{Ag}\right)^2ne^2}{\omega^3m_e}\times\left(\rho_b+\frac{3\pi\hbar}{e^2dk_f}\times\frac{\Delta^2}{\xi}\right)+\mathrm{Im}\left[\sum_{j=1}^{5}\frac{s_j\omega_j^2}{\omega_j^2-\omega^2-i\omega\gamma_j}\right]. \tag{2.5}$$

With Eqs. (2.1), (2.4), and (2.5), we can now calculate the expected values for ε^{em} as a function of surface roughness using f^{Ag} and the measured values of Δ and ξ. All other parameters are taken from the literature.[18-19] Specifically, we used Drude-Lorentz parameters that fit the data from Johnson and Christy.[6] The values obtained for ε_1^{Ag} and ε_2^{Ag} from Eqs. (2.4) and (2.5) are shown in figure 2.3. The final calculated values for ε_1^{em}

and ε_2^{em} from Eq. (2.1) are then plotted in figure 2.2c and 2.2d for direct comparison with experiment.

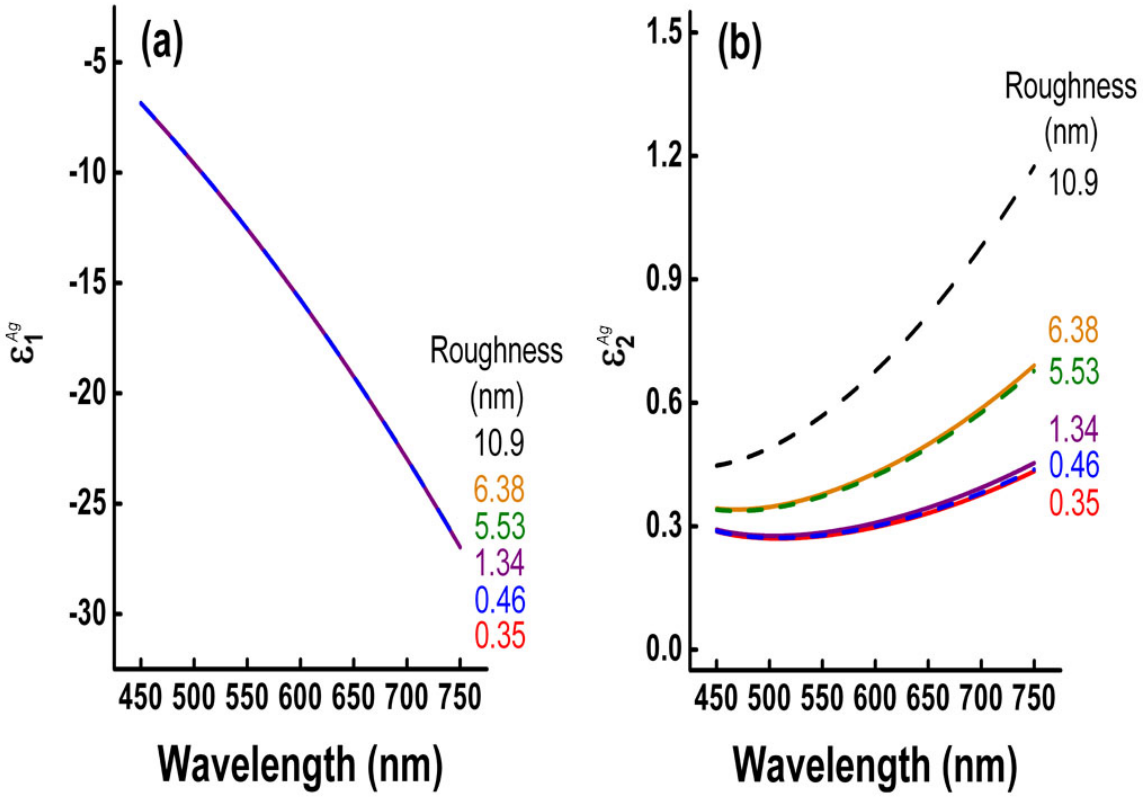

Figure 2.3 The calculated ε_1^{Ag} (a) and ε_2^{Ag} (b) of Ag films with different surface roughness using the Drude-Lorentz model. The ε_1^{Ag} curves have the same value regardless of roughness, but the ε_2^{Ag} increases with increasing surface roughness due to an additional resistivity (ρ_s) caused by electron scattering at the surfaces. In template-stripped films, this additional surface resistivity is small compared to the bulk resistivity. Note also that the resistivity difference between surfaces with a roughness of 5.53 and 6.38 nm is only 0.06 μΩcm. This explains why there are three groupings of curves in (b).

Despite the simplicity of the model, ε_1^{em} and ε_2^{em} reproduce the experimental trends. They become more negative and smaller, respectively, with decreasing surface roughness. Indeed, the calculated ε_1^{em} curves show strong quantitative agreement. However, the ε_2^{exp} curves (figure 2.2b) are typically higher than the calculated ε_2^{em} (figure 2.2d) for the same roughness. We note that this discrepancy depends on the parameters

used in the calculation. It is relevant that Johnson and Christy[6] reported values of ε_2^{Ag} with a sizeable error, *e.g.*, ~0.3 at 650 nm. If parameters that fit the data from Palik[7] are

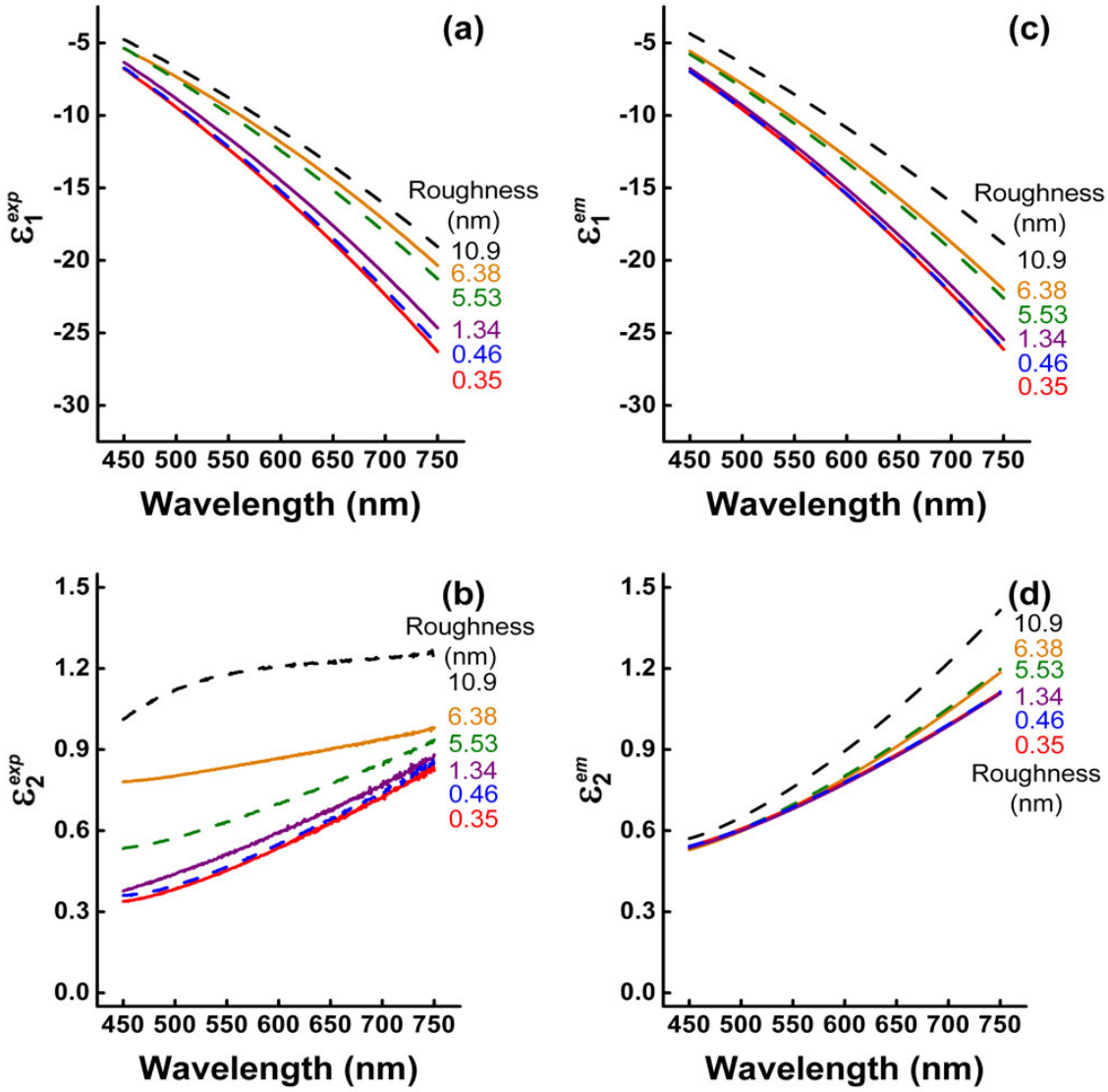

Figure 2.4 The measured real (a) and imaginary (b) components and the predicted real (c) and imaginary (d) components of the effective dielectric function for Ag films with different surface roughness. The standard deviations of ε_1^{exp} and ε_2^{exp} were estimated as ±0.05 and ±0.01, respectively. The legends indicate the RMS roughness for the experimental films. For the predictions, the RMS heights Δ and the lateral correlation lengths ξ extracted from a Gaussian fit of the power spectral density function to atomic force micrographs were used. The predictions utilize a combination of the effective medium and Drude-Lorentz models. Drude-Lorentz parameters that fit data from E. D. Palik (reference 7) were used.

employed instead of those from Johnson and Christy, we obtain much higher calculated ε_2^{em} values (see figure 2.4). While additional loss mechanisms not included in our model might also be required to match the experimental data (such as electronic scattering at grain boundaries), it is likely that the actual imaginary dielectric function for Ag and consequently the true Drude-Lorentz parameters lie between references 6 and 7. In other words, our results indicate that even ultrasmooth Ag interfaces that exhibit reduced losses, do not match those in Johnson and Christy.

It is interesting to consider the origin of the changes in the effective dielectric function with roughness. Within the effective medium model, one might expect both ε_1^{em} and ε_2^{em} simply to decrease in magnitude with increasing roughness as more air is introduced into the effective medium. This effect can indeed explain the origin of the observed trend in ε_1^{exp}. However, it fails with ε_2^{exp}, which increases in magnitude with increasing roughness. In contrast, the Drude-Lorentz model predicts that with increasing roughness ε_1^{Ag} is unaffected [Eq. (2.4)] while ε_2^{Ag} increases [Eq. (2.5)]. The origin of this increase is the additional losses introduced by electronic surface scattering, quantified in Δ^2 [Eq. (2.3)]. (Changes in ξ have a smaller effect.) Therefore, our model suggests that template stripping can reduce losses by minimizing electronic scattering at the interface. As seen in Table 2.1, ρ_s can be negligible compared to ρ_b in template-stripped films. Consequently, the ε_2^{Ag} for the template-stripped surfaces is mainly determined by ρ_b, which is an intrinsic material property for Ag of a given purity. This explains the small differences in ε_2^{exp} between the different template-stripped interfaces (figure 2.2b).

Finally, we can consider the impact of these changes on the propagation length of SPPs, which is an important characteristic for the performance of plasmonic devices. The propagation length can be calculated from the measured effective dielectric function and surface parameters.[1] Figure 2.5 illustrates the predicted SPP propagation lengths at the wavelengths of 488, 532, and 632 nm for Ag surfaces with different roughness. As the surface roughness decreases, the propagation length increases significantly at all three wavelengths. The propagation length of the template-stripped surface with the smallest

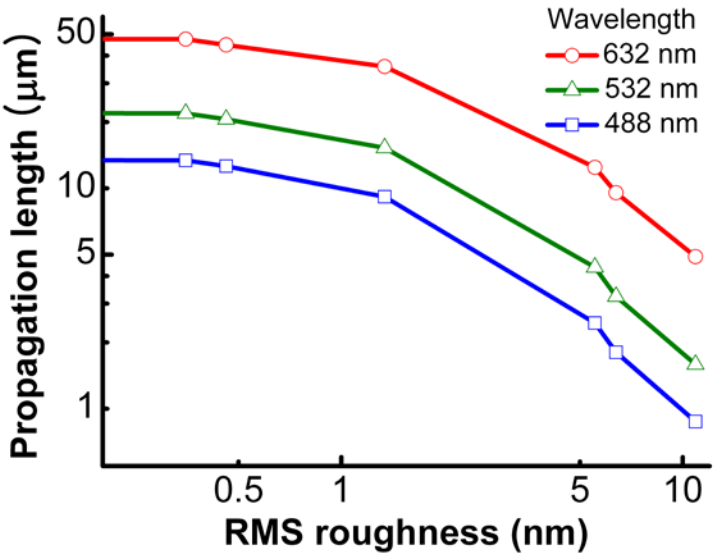

Figure 2.5 Predicted SPP propagation lengths for Ag surfaces as a function of roughness at different wavelengths. The *y*-intercepts of each curve imply the propagation length of the surface with zero roughness. The curves are calculated using the measured effective dielectric function and surface parameters.

roughness is estimated to be 10 times longer than a conventional surface. This is not only due to reduced SPP scattering but also the improved dielectric function.

2.3 Conclusions

In conclusion, we have demonstrated that template stripping can improve the effective dielectric function of Ag surfaces. This observation agrees with the relation between dielectric function and surface roughness using the effective-medium model and the Drude-Lorentz model. This result can be useful for the fabrication of plasmonic devices with enhanced SPP propagation length.

2.4 References

[1] H. Raether, *Surface Plasmons on Smooth and Rough Surfaces and on Gratings*. Springer-Verlag: Berlin, 1988.

[2] W. L. Barnes, A. Dereux, T. W. Ebbesen, "Surface Plasmon Subwavelength Optics," *Nature* **2003,** *424*, 824.

[3] E. Ozbay, "Plasmonics: Merging Photonics and Electronics at Nanoscale Dimensions," *Science* **2006,** *311*, 189.

[4] H. A. Atwater, "The Promise of Plasmonics," *Sci. Am.* **2007,** *296*, 56.

[5] A. Polman, "Applied Physics: Plasmonics Applied," *Science* **2008,** *322*, 868.

[6] P. B. Johnson, R. W. Christy, "Optical constants of the noble metals," *Phys. Rev. B* **1972,** *6*, 4370.

[7] E. D. Palik, *Handbook of Optical Constants of Solids*. Academic Press: Orlando, 1985.

[8] M. J. Weber, *Handbook of Optical Materials*. CRC Press: Boca Raton, 2003.

[9] M. Hegner, P. Wagner, G. Semenza, "Ultralarge Atomically Flat Template-Stripped Au Surfaces for Scanning Probe Microscopy," *Surf. Sci.* **1993,** *291*, 39.

[10] C.-H. Sun, N. C. Linn, P. Jiang, "Templated Fabrication of Periodic Metallic Nanopyramid Arrays," *Chem. Mater.* **2007,** *19*, 4551.

[11] P. Nagpal, N. C. Lindquist, S.-H. Oh, D. J. Norris, "Ultrasmooth Patterned Metals for Plasmonics and Metamaterials," *Science* **2009,** *325*, 594.

[12] N. C. Lindquist, P. Nagpal, A. Lesuffleur, D. J. Norris, S.-H. Oh, "Three-Dimensional Plasmonic Nanofocusing," *Nano Lett.* **2010,** *10*, 1369.

[13] A. Rueda, N. Vogel, M. Kreiter, "Characterization of Gold Films by Surface Plasmon Spectroscopy: Large Errors and Small Consequences," *Surf. Sci.* **2009,** *603*, 491.

[14] J. A. Woollam, B. Johs, C. M. Herzinger, J. Hilfiker, R. Synowicki, C. L. Bungay, "Overview of Variable Angle Spectroscopic Ellipsometry (VASE), Part I: Basic Theory and Typical Applications," *SPIE Proc.* **1999,** *CR72*, 3.

[15] C. A. Fenstermaker, F. L. McCrackin, "Errors Arising from Surface Roughness in Ellipsometric Measurement of the Refractive Index of a Surface," *Surf. Sci.* **1969,** *16*, 85.

[16] D. E. Aspnes, "Optical Properties of Thin Films," *Thin Solid Films* **1982,** *89*, 249.

[17] D. E. Aspnes, J. B. Theeten, F. Hottier, "Investigation of Effective-Medium Models of Microscopic Surface Roughness by Spectroscopic Ellipsometry," *Phys. Rev. B* **1979,** *20*, 3292.

[18] X. Ni, Z. Liu, A. V. Kildishev PhotonicsDB: Optical Constants, http://nanohub.org/resources/PhotonicsDB.

[19] N. W. Ashcroft, N. D. Mermin, *Solid State Physics*. Saunders College: Philadelphia, 1976.

[20] E. Z. Luo, S. Heun, M. Kennedy, J. Wollschläger, M. Henzler, "Surface Roughness and Conductivity of Thin Ag Films," *Phys. Rev. B* **1994,** *49*, 4858.

[21] A. Kaser, E. Gerlach, "Scattering of Conduction Electrons by Surface Roughness in Thin Metal Films," *Z. Phys. B* **1995,** *97*, 139.

Chapter 3.
Single-Crystalline Silver Films for Plasmonics*

Precisely patterned nanostructures with low damping of surface plasmon polaritons (SPPs) are of critical importance in plasmonic applications. However, grain structure in conventional polycrystalline metallic films can decrease the quality of desired patterns due to induced roughness and increased SPP losses on the films. Herein, we report a simple approach to obtain precise nanostructures with improved dielectric properties based on single-crystalline metallic films. These films were prepared by epitaxial growth of silver on mica substrates at elevated temperatures. Under controlled deposition conditions, the films had extremely flat surfaces over large areas. The dielectric functions of the resulting films were compared with those of polycrystalline films with identical surface roughness. The dielectric functions of the single-crystalline films showed a larger negative real component and a smaller imaginary component, giving higher electrical conductivity and smaller optical absorption, respectively. These results indicate that the absence of grain boundaries significantly reduces ohmic losses and scattering, leading to improved dielectric properties and increased propagation lengths for SPPs. Furthermore, when nanostructures were fabricated by focused-ion-beam milling, the uniform nature of the single-crystalline films allowed more precise patterning of high-quality nanostructures, while the different grain orientations in the polycrystalline films resulted in increased roughness within the patterned areas. The single-crystalline films can therefore provide an effective route to plasmonic devices with enhanced performance.

---

* This chapter is reproduced with permission from Jong Hyuk Park, Palak Ambwani, Michael Manno, Nathan C. Lindquist, Prashant Nagpal, Sang-Hyun Oh, Chris Leighton, and David J. Norris, "Single-Crystalline Silver Films for Plasmonics," *Advanced Materials* **2012**, *24*, 3988 (DOI: 10.1002/adma.201200812).

3.1 Introduction

Surface plasmon polaritons (SPPs) are hybrid photon-electron waves that propagate along a metal-dielectric interface.[1] Due to their hybrid nature, SPPs can be exploited to control and concentrate light below the optical diffraction limit, generating large electric fields in confined regions.[2-4] This unique characteristic of SPPs has led to their application in many areas including surface-enhanced spectroscopy,[5-7] molecular sensing,[8-10] nanofocusing,[11-13] subwavelength waveguides,[14-15] optical antennas,[16-17] data storage,[18-19] and photovoltaics.[20] In many cases, patterned metals are employed to generate and manipulate SPPs. The precision of these structures and the dielectric properties of the metal are critical factors in determining the performance of plasmonic devices.[1-2] Surface inhomogeneities should be minimized to avoid SPP scattering during propagation, and the metal should have high conductivity and low optical absorption to enhance optical confinement and reduce losses.

To obtain patterned metallic films, a two-step procedure is typically utilized. Metals are first deposited via evaporation or sputtering on a substrate and then patterned with focused-ion-beam (FIB) milling.[21-22] However, since the deposited films are polycrystalline and etch rates vary for different grain orientations,[23] the patterning procedure can lead to increased surface roughness. One possible solution is to prepare single-crystalline metals, which will etch more uniformly and lead to precise patterns. To address this possibility, single-crystalline silver and gold samples have been prepared by several approaches, including the Czochralski process,[24] colloidal chemistry,[25-29] and nanoskiving.[30] The resulting samples have demonstrated great promise for plasmonics. However, they also have disadvantages. The Czochralski process requires specialized equipment and additional polishing to obtain smooth surfaces, leading to high costs. Colloidal chemistry leads to micrometer-scale flakes or nanowires that are dispersed in a solvent. Consequently, they are susceptible to aggregation, are inhomogeneous in size and shape, and are inconvenient to place and manipulate for device fabrication. It would be preferable to have a simple approach to produce continuous, smooth, and inexpensive

single-crystalline metallic films, which could then be used as the starting material for a variety of plasmonic devices.

Herein, we demonstrate that epitaxial growth can provide an effective route to obtain smooth single-crystalline metallic films for plasmonics.[31-35] In epitaxy, the crystalline structure and orientation of the growing films are strongly influenced by those of the underlying substrate. Compared to single-crystalline films obtained via the Czochralski process or colloidal chemistry, epitaxial metallic films can provide many advantages: a flat surface over a large area, an accurately controlled thickness, and high crystallinity. Epitaxial growth is also a simple and reproducible process that offers lower cost. Finally, it is applicable to both silver and gold, which are the most widely studied metals for plasmonic applications.

3.2 Results and Discussion

In this work, we focus on silver because it has better optical properties at visible wavelengths at less expense. For the substrate, several reasonably well lattice-matched materials such as mica, MgO, Al_2O_3, and silicon have already been used for epitaxial growth of silver films.[32-35] We chose mica due to its flat surface, high chemical stability, low cost, and propensity for smooth epitaxial growth of Ag and Au. We deposited nominally 100-nm-thick silver films epitaxially on mica substrates by dc magnetron sputtering under controlled conditions. It is known that the surface morphology and crystalline structure of such epitaxial films are strongly influenced by the deposition rate and substrate temperature.[31-33] Since a high deposition rate is needed to make the surface continuous and flat,[33] i.e. to avoid surface-diffusion-enabled agglomeration, we utilized the maximum deposition rate (1.65 nm/s) that was achievable via simple means in our sputtering system. As expected, a high substrate temperature of over 300 °C was necessary to form a single-crystalline structure. Table 3.1 reports the deposition conditions for our samples. The film (denoted SC1) deposited with a substrate temperature of 350 °C was particularly smooth over large areas, as detailed further below.

Table 3.1 Surface roughness and microstructure of sputtered Ag films as a function of deposition temperature. The pressure in the sputtering chamber was maintained at 6 mTorr with argon during deposition. Root mean square (RMS) roughness was determined from atomic force microscopy scans over an area of 2.5 × 2.5 μm^2.

Substrate temperature (°C)	Deposition rate (nm/s)	Measured thickness (nm)	Crystalline structure	RMS roughness (nm)	Sample
30	1.65	96	Polycrystalline	1.28 ± 0.06	
300	1.65	98	Single-crystalline	1.20 ± 0.10	
350	1.65	97	Single-crystalline	0.82 ± 0.05	SC1
500	1.65	94	Single-crystalline	1.26 ± 0.24	
350	1.65	201	Single-crystalline	1.30 ± 0.10	SC2

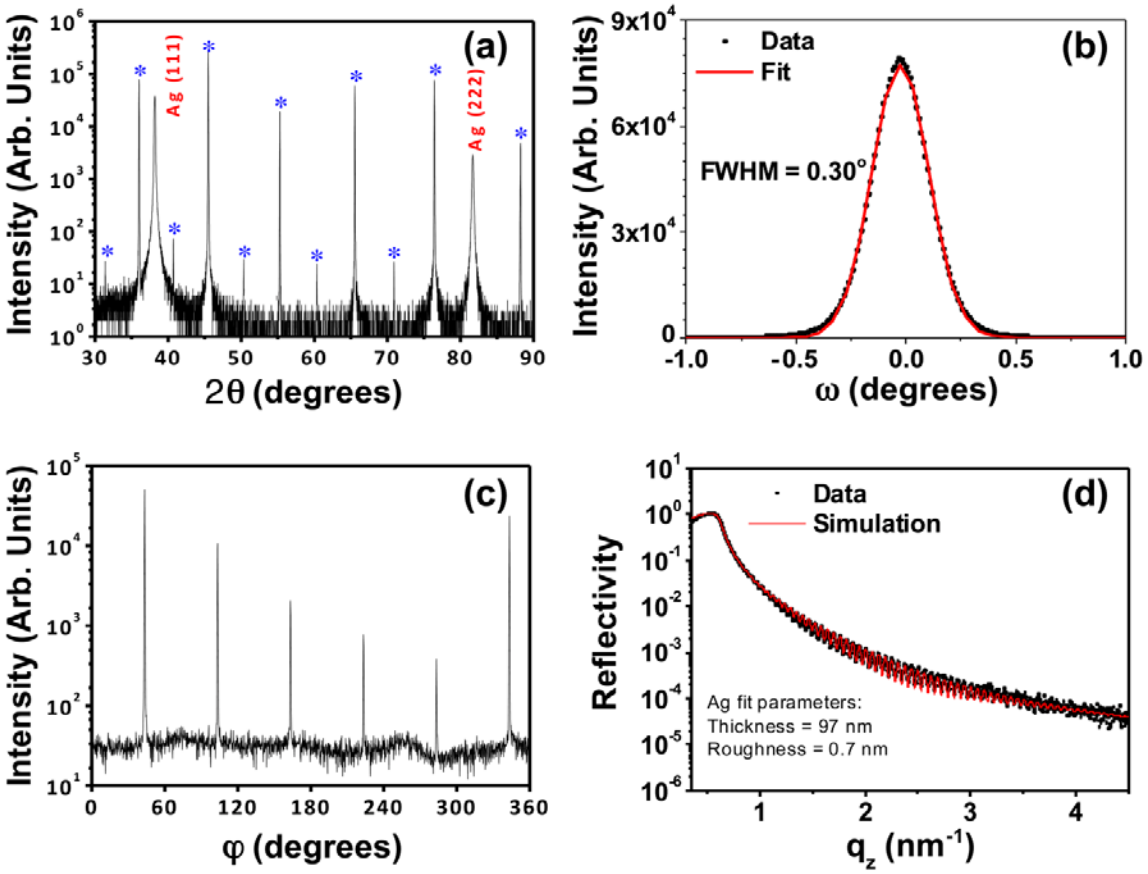

Figure 3.1 Structural characterization of a 97-nm-thick c-axis mica/Ag(111) film (SC1) deposited at 350 °C. (a) High-resolution specular X-ray diffraction (XRD) (θ-2θ) scan with asterisk symbols indicating substrate diffraction peaks. (b) Transverse scan (rocking curve) through the Ag(111) diffraction peak. The measured transverse scan and a fitted Gaussian profile are represented by black dots and a solid red line, respectively. (c) Grazing-incidence in-plane XRD scan (ϕ-scan) of the Ag(220) plane. (d) Measured (black circles) and simulated (solid red line) grazing-incidence specular X-ray reflectivity. The Ag surface roughness and thickness, extracted from the fit, are shown.

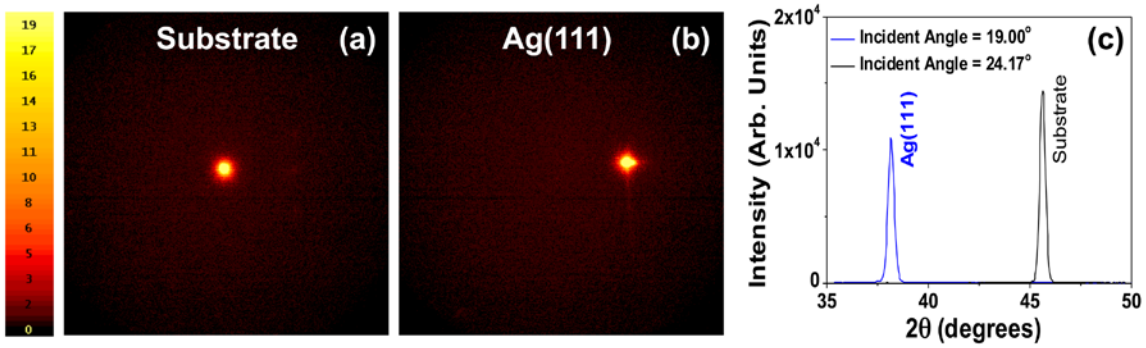

Figure 3.2 Two-dimensional XRD patterns of a 97-nm-thick c-axis mica/Ag(111) film (SC1) deposited at 350 °C. (a) Area-detector image of the highest intensity c-axis mica diffraction peak centered on a 2θ angle of 45° and an X-ray incidence angle of 24.17° (Bragg angle of the mica peak). (b) Ag(111) area detector image centered on a 2θ angle of 38° and an X-ray incidence angle of 19.00° [Bragg angle of Ag(111) peak]. (c) Integrated XRD patterns of the highest intensity c-axis mica diffraction peak (solid black line) and Ag(111) diffraction peak (solid blue line) from parts (a) and (b), respectively.

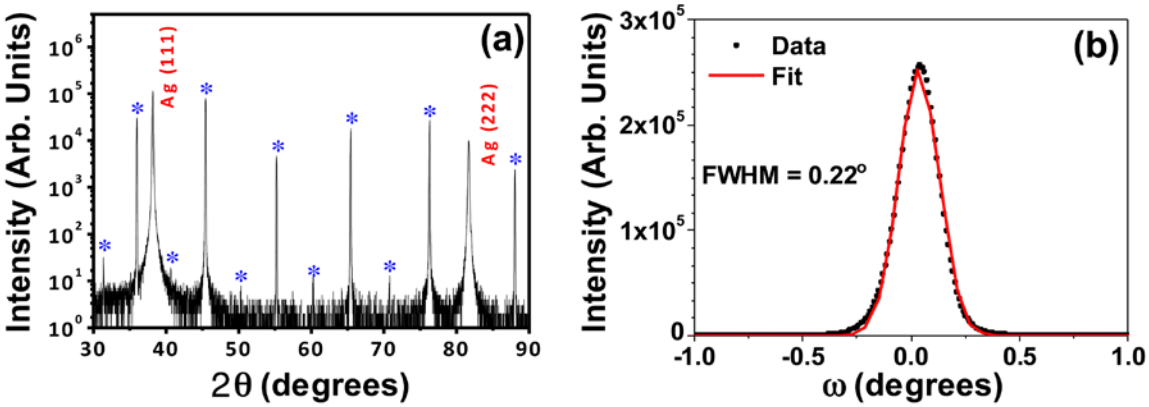

Figure 3.3 Structural characterization of a 201-nm-thick c-axis mica/Ag(111) film (SC2) deposited at 350 °C. (a) High-resolution specular XRD (θ-2θ) scan with asterisk symbols indicating substrate diffraction peaks. (b) Transverse scan (rocking curve) through the Ag(111) diffraction peak. The measured transverse scan and a fitted Gaussian profile are represented by black dots and a solid red line, respectively.

The microstructure of our films was characterized via high-resolution wide-angle X-ray diffraction (XRD). Figure 3.1a shows that the wide-angle XRD pattern of SC1 contains only the Ag(111) and Ag(222) peaks in addition to those from the substrate. This indicates that the film is single crystalline in the z (growth) direction and aligned (111) out-of-plane. This is expected from prior work on Ag grown on c-axis mica,[33] as well as simple lattice-matching models. The rocking curve through the Ag(111) peak has a full-width-at-half-maximum (FWHM) of 0.3°, indicative of a low mosaic spread in the

film (figure 3.1b). A grazing-incidence in-plane X-ray scan was also performed on the Ag(220) peak and it showed the 6-fold symmetry expected for (111) oriented films (figure 3.1c). These results demonstrate that SC1 is also single crystalline in plane. Furthermore, figure 3.1d shows the grazing-incidence X-ray reflectivity of SC1. Simulations suggest Ag surface roughness of 0.7 nm over the long lateral length scale probed. When the film thickness was increased up to 200 nm under the same growth conditions (film SC2 in table 3.1), single crystallinity was maintained (see figure 3.3).

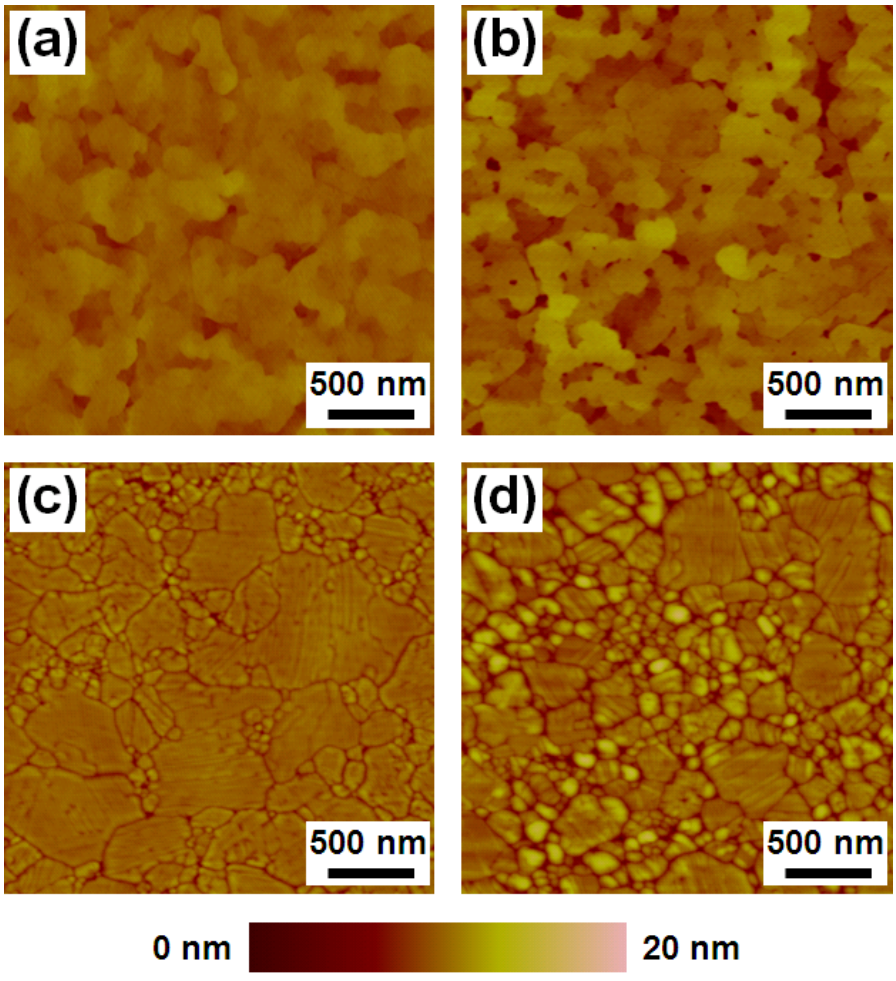

Figure 3.4 AFM images of single-crystalline Ag films [(a) SC1 and (b) SC2] and polycrystalline Ag films [(c) PC1 and (d) PC2]. These films have RMS roughness of 0.82, 1.30, 0.81, and 1.39 nm, respectively. All scanned areas are 2.5 × 2.5 μm^2.

The surface morphology of our films was further quantified with atomic force microscopy (AFM). The surface of SC1 was continuous without pinholes or islands, and no grain boundaries were found (figure 3.4a). The contrast observed in the AFM image of SC1 is due to mild height variations arising from the epitaxial growth mechanism.[33] The root mean square (RMS) roughness was 0.82 nm measured over 2.5 × 2.5 μm^2, very close to the 0.7 nm extracted from X-ray reflectivity in figure 3.1d. For the thicker sample grown under the same conditions (SC2), the surface was still continuous without any grain boundaries, with only a small increase in surface roughness (see table 3.1 and figure 3.4b).

Recently, we could obtain single-crystalline silver films with much smoother surfaces by optimizing the deposition conditions and employing pre- and post-annealing processes. We will discuss this result in Appendix A.

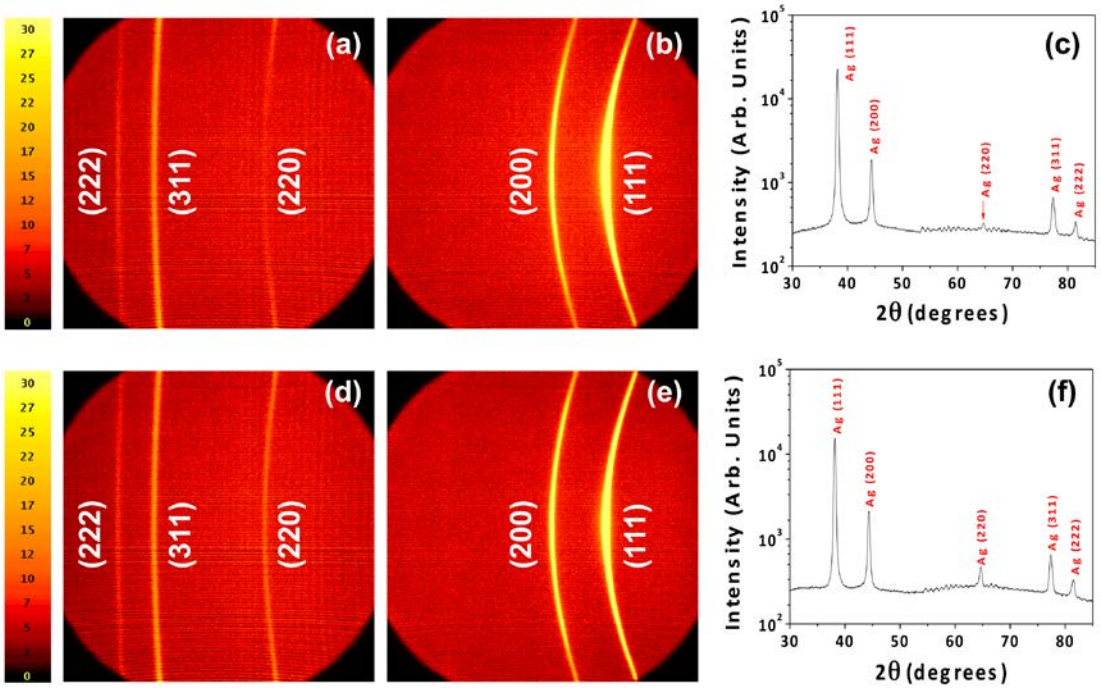

Figure 3.5 Two-dimensional XRD patterns of 200-nm-thick Si(001)/Ag polycrystalline films. Area-detector images of polycrystalline sample PC1 with a 2θ angle centered at (a) 70° and (b) 45°. (c) Integrated XRD pattern of sample PC1 from area-detector scans. Area-detector images of polycrystalline sample PC2 with a 2θ angle centered at (d) 70° and (e) 45°. (f) Integrated XRD pattern of sample PC2 from area-detector scans. Note the slight texture in the (111) Debye ring. The weak apparent oscillations near the Ag(220) reflection are a detector artifact.

Since flat single-crystalline films can result in reduced SPP propagation losses, these films should exhibit good performance for plasmonic applications. To demonstrate this, we compared our single-crystalline films with polycrystalline films with identical surface roughness. Because it is difficult to obtain extremely flat surfaces with a roughness of less than 1 nm through conventional evaporation, the template-stripping method was used.[36-39] 200-nm-thick silver films were deposited on clean silicon wafers and then stripped from the substrates using an epoxy backing layer. The roughness of the stripped surfaces was controlled by the deposition and stripping conditions. These template-stripped films showed Debye ring XRD patterns with a two-dimensional area detector (figure 3.5), implying a randomly oriented polycrystalline grain structure. The conditions were also adjusted so that these films had nearly identical surface roughness (figure 3.4c and 3.4d) as the epitaxial films, SC1 and SC2. The polycrystalline films with a roughness of 0.81 and 1.39 nm are denoted PC1 and PC2, respectively.

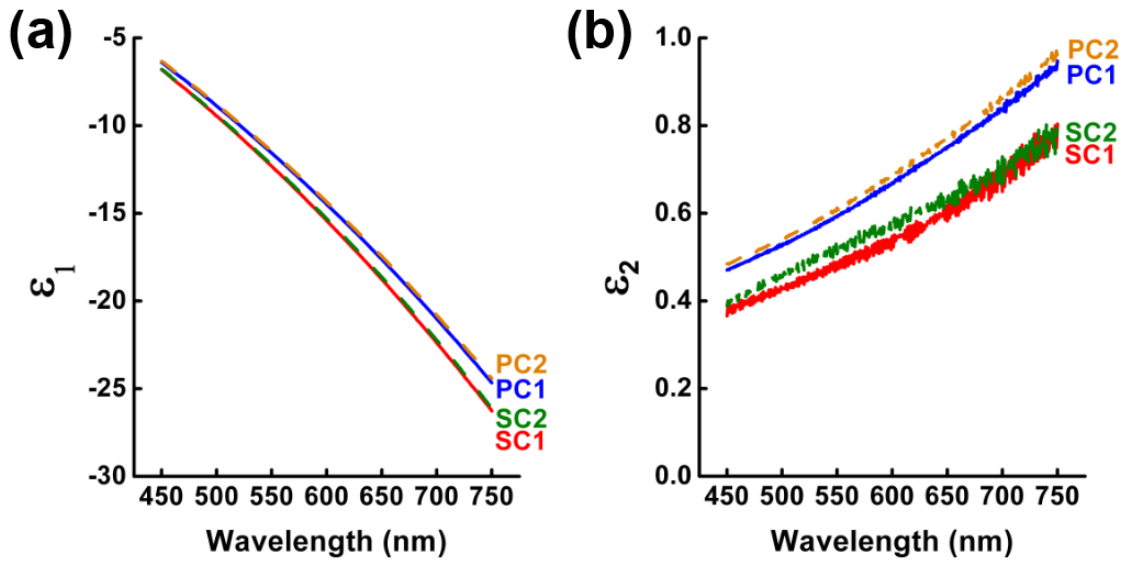

Figure 3.6 Real component (a) and imaginary component (b) of the dielectric functions of single-crystalline Ag films (SC1 and SC2) and polycrystalline Ag films (PC1 and PC2). Polarized incident light in the wavelength range of 450-750 nm was reflected from the films and detected. Three different incidence angles were used: 65, 70, and 75°. The dielectric functions were fitted using numerical iteration and the Fresnel equations. The standard deviations for ε_1 and ε_2 were estimated as ± 0.05 and ± 0.02, respectively.

Using a multi-angle spectroscopic ellipsometer, we compared the dielectric functions of the single-crystalline and polycrystalline films. The epitaxial films exhibited dielectric functions with a larger negative real component (ε_1) and a smaller imaginary component (ε_2) than the polycrystalline films, as shown in figure 3.6. The larger negative ε_1 indicates higher conductivity. Indeed, the dc electrical resistivity of SC2 was measured to be less than that of PC2 (table 3.2). The smaller ε_2 in the epitaxial films indicates a lower energy loss, which is important to enhance the propagation length of SPPs. Furthermore, the dielectric functions of the films were also affected by surface roughness. Even though this effect was not significant in the tested films due to a small difference in the surface roughness, films with smoother surfaces showed higher conductivity and lower optical absorption, consistent with previous work.[40]

Table 3.2 Electrical properties of SC2 and PC2.

Sample	Thickness (nm)	Temperature (K)	Electrical resistivity, ρ (μΩcm)	Mean free path (Å)	Residual resistivity ratio [= ρ(300 K) / ρ(5.5 K)]
SC2	200	5.5	6.02×10^{-2}	1.4×10^{4}	25.6
		300	1.54	550	
PC2	200	5.5	2.71×10^{-1}	3.1×10^{3}	6.1
		300	1.65	510	

Four-terminal quasi-dc (16 Hz) resistance measurements were used to determine the resistivity of films. Au wires were soldered onto the films, using indium point contacts, to connect the sample to an in-house measurement probe. Resistance was measured as a function of temperature, which was varied from room temperature to liquid He temperature. The van der Pauw method was used to convert sheet resistance to resistivity. The mean free path was calculated from the resistivity, using the Drude model and a carrier concentration of 6×10^{22} cm^{-3}, estimated from the electron count and lattice parameter.

To demonstrate the improved plasmonic properties of single-crystalline films over polycrystalline films, we measured the SPP propagation length in both types of films. Figure 3.7a shows a schematic of the experimental setup for the measurement.[41] A series of identical slits were patterned on both epitaxial and polycrystalline silver films via FIB milling. Then, a parallel groove was added adjacent to each slit at a distance, *d*. The slits

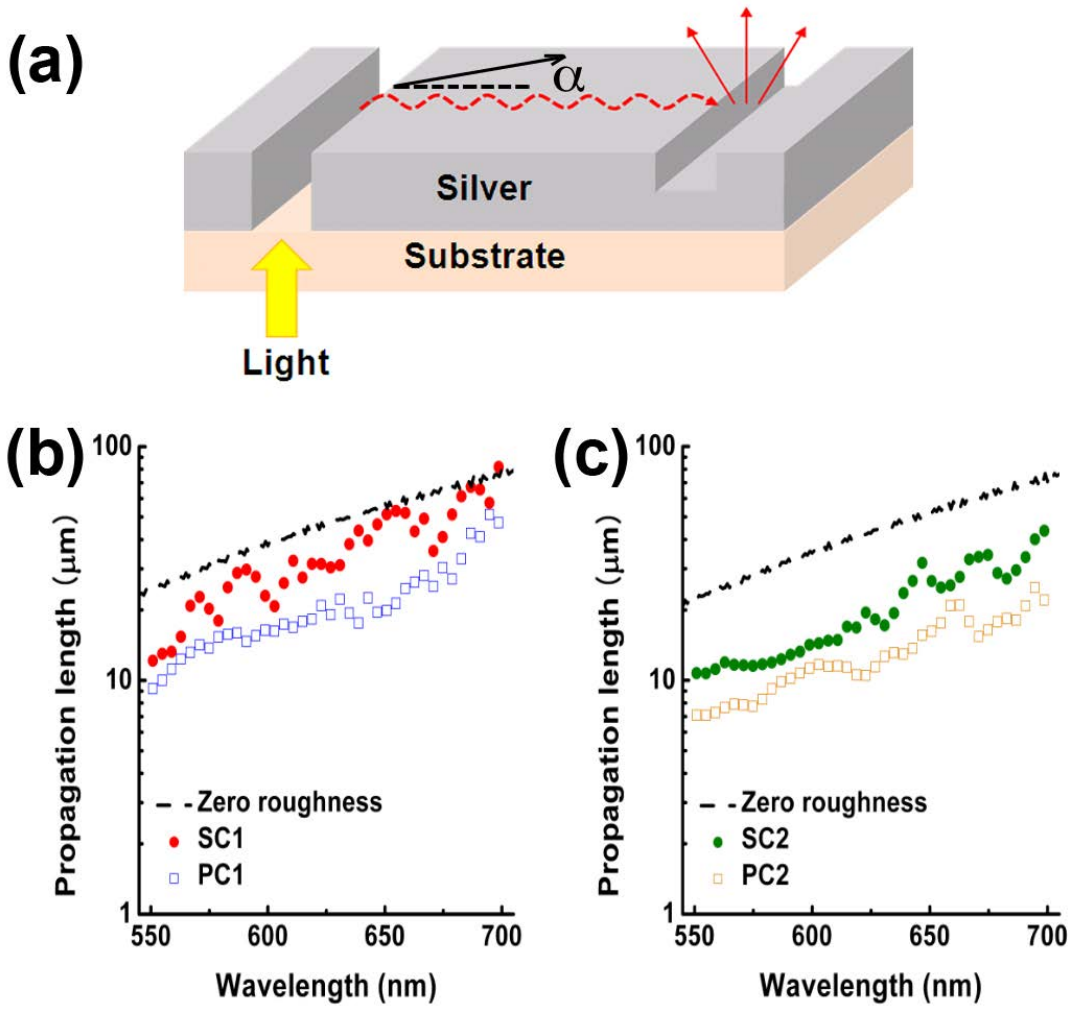

Figure 3.7 (a) Schematic diagram of the experimental setup for the measurement of the propagation length of SPPs on Ag films. (b) SPP propagation lengths on a single-crystalline Ag film (SC1) and a polycrystalline Ag film (PC1). The surface roughness of the films is almost identical (0.82 and 0.81 nm, respectively). The dashed line is the predicted propagation length using the measured dielectric function of SC1 when assuming only ohmic losses and no roughness. Roughness would decrease this curve by ~5%. (c) SPP propagation lengths on a single-crystalline Ag film (SC2) and a polycrystalline Ag film (PC2). The surface roughness of the films is almost identical (1.30 and 1.39 nm, respectively). The dashed line is the predicted propagation length using the measured dielectric function of SC2 when assuming only ohmic losses and no roughness. Roughness would decrease this curve by ~10%. In (b) and (c) the experimental data are corrected for SPPs that propagate at various angles, α.

and grooves were each 200 nm wide and 40 μm long, and *d* was varied from 10 to 40 μm. When the sample was illuminated with white light from the substrate side, transmitted light through the slit generated SPPs that propagated along the silver surfaces. When

these SPPs struck the adjacent groove, they were partially scattered into the far field and the resulting light was collected with an optical microscope. We measured the spectrum of the scattered light for all slit-groove pairs, and by fitting the data to an exponential decay of intensity versus distance *d*, we extracted the propagation length of the SPPs as a function of optical wavelength.[38]

For each film, we determined two sets of values. To obtain the first set, we assumed that all of the SPPs propagated along the shortest path between the slit and groove (the dashed red arrow in figure 3.7a). The results are plotted in figure 3.8. However, this approach underestimates the propagation length.[22, 38] Some SPPs will be launched from the slit at an angle α (figure 3.7a) and yet still strike the groove. Thus, at

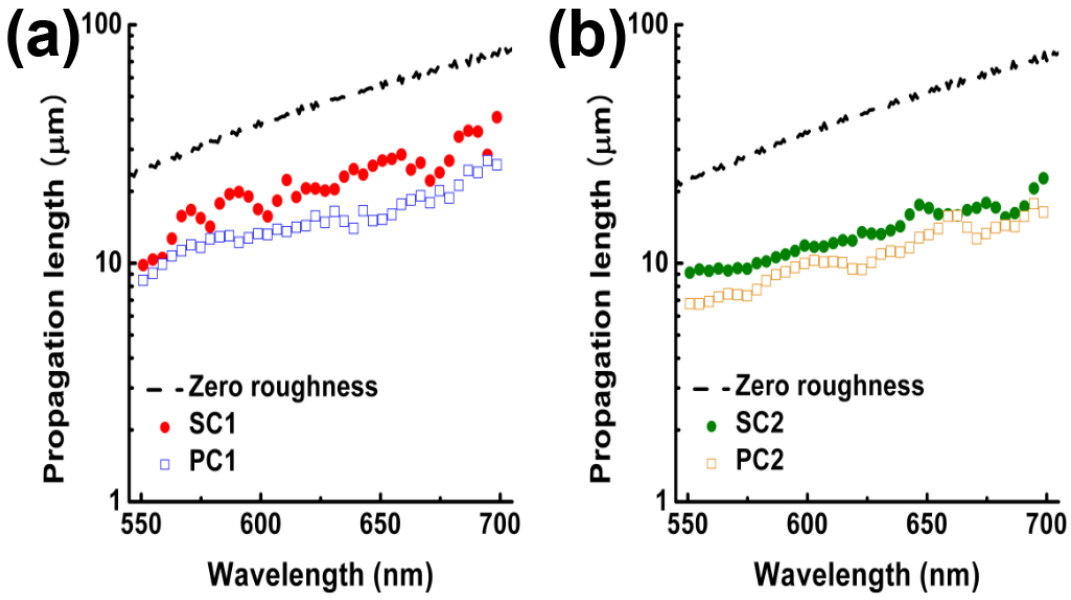

Figure 3.8 (a) SPP propagation lengths on a single-crystalline Ag film (SC1) and a polycrystalline Ag film (PC1). The values were extracted using Equation (3.1) and are therefore underestimated. The surface roughness of the films is almost identical (0.82 and 0.81 nm, respectively). The dashed line is the predicted propagation length using the measured dielectric function of SC1 and assuming only ohmic losses and no roughness. (b) SPP propagation lengths on a single-crystalline Ag film (SC2) and a polycrystalline Ag film (PC2). The values were extracted using Equation (3.1) and are therefore underestimated. The surface roughness of the films is almost identical (1.30 and 1.39 nm, respectively). The dashed line is the predicted propagation length using the measured dielectric function of SC2 and assuming only ohmic losses and no roughness.

short slit-groove separations, more SPPs will be scattered and detected. Due to the fixed length of the slits and grooves (40 μm), the range of angles α that will be collected decreases as the slit-groove separation increases. This causes an additional decay of the signal with *d*, which is purely geometrical, and leads to an underestimation of the SPP propagation length. Our second set of values is corrected for this effect. By assuming that the SPPs can be launched from the slit with equal probability at any angle α, a geometrical factor that accounts for the average acceptance angle of each slit-groove pair was included in the model (see the Experimental Section for details). The resulting SPP propagation lengths for single-crystalline and polycrystalline films are shown in figure 3.7b (SC1 and PC1) and 3.7c (SC2 and PC2).

We observe that SPPs propagate further on epitaxial films, which lack grain boundaries. With similar surface roughness, SC1 exhibited on average a ~70% improvement in the SPP propagation length over PC1 (figure 3.7b). The propagation length with SC2 increased on average ~55% compared to PC2 (figure 3.7c). This shows that the effect of the grain boundaries on the propagation length is critical for smooth surfaces. On rougher surfaces, SPP scattering by the surface roughness dominates. For this reason, compared to a polycrystalline film, the smoother epitaxial film (SC1) exhibited a larger relative improvement in the propagation length than the rougher one (SC2). Also, as previously reported,[1, 38] smooth films (SC1 and PC1) have longer SPP propagation lengths than rough films (SC2 and PC2).

Assuming that the surface has zero roughness and the SPPs are damped only by ohmic losses, we can estimate the theoretical propagation lengths using the measured dielectric functions from the same films. As shown in figure 3.7b and 3.7c, the theoretical values of the propagation lengths are slightly larger than the actual SPP propagation lengths. If the roughness is incorporated into the theory,[38] the theoretical curves decrease by ~5% and ~10% for SC1 and SC2, respectively. In addition, subtle surface contamination or oxidation, which is not included in the model, could lead to a decrease in the experimental curves.

Because we have measured the propagation lengths on both single-crystalline and polycrystalline films of the same roughness, we can in principle estimate the contribution of grain boundary scattering to the overall SPP propagation length. (In practice, extracting L_{gb} is complicated by the discrepancy between experiment and theory, as well as the fact that the crystallinity also affects the dielectric functions. See the Experimental Section for details). This contribution can be quantified in terms of a grain boundary scattering length, L_{gb}. This is the length that SPPs would propagate if no other loss mechanisms were active. It was previously reported for gold films,[24] where L_{gb} was approximated as g/S_{gb}, with g the average grain size and S_{gb} the grain boundary scattering coefficient. For 20 nm grains in gold, S_{gb} was determined to be 0.2%. If we estimate S_{gb} using films SC1 and PC1 (with g~180 nm), we obtain an average L_{gb} of 120 μm with S_{gb} of ~0.15%. Similarly, SC2 and PC2 (with g~140 nm) yield an average L_{gb} of 80 μm with S_{gb} of ~0.18%. However, these values must be considered as rough estimates.

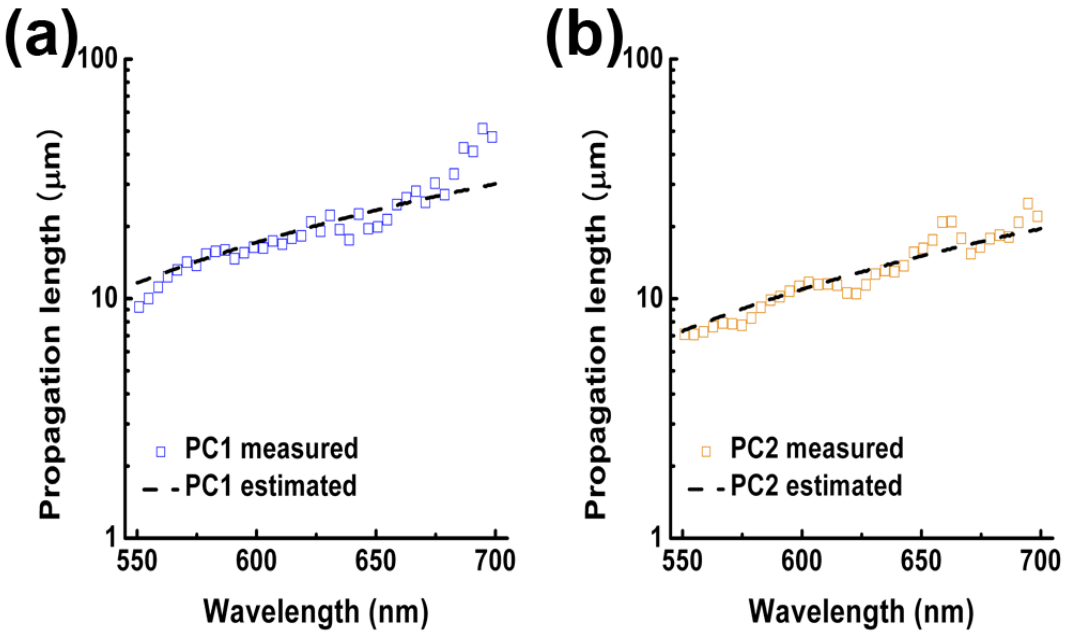

Figure 3.9 Comparison of the measured SPP propagation lengths and a fit. From the fit, a rough estimate for the grain boundary contribution, L_{gb}, to the propagation length could be extracted. (a) data for PC1 with L_{gb} of 120 μm, g of 180 nm, and S_{gb} of 0.15%, and (b) data for PC2 with L_{gb} of 80 μm, g of 140 nm, and S_{gb} of 0.18%.

Another important advantage of single-crystalline samples is that they are well suited to precise patterning.[42] Figure 3.10 shows scanning electron microscopy (SEM) images of nanostructures fabricated in SC1 and PC1 patterned via FIB milling. A significant difference in the surface morphology of the nanostructures is observed (figure 3.10a,3.10c, and 3.10b,3.10d, respectively). Even though both films had nearly identical surface roughness before patterning, the obtained structures on PC1 were very rough

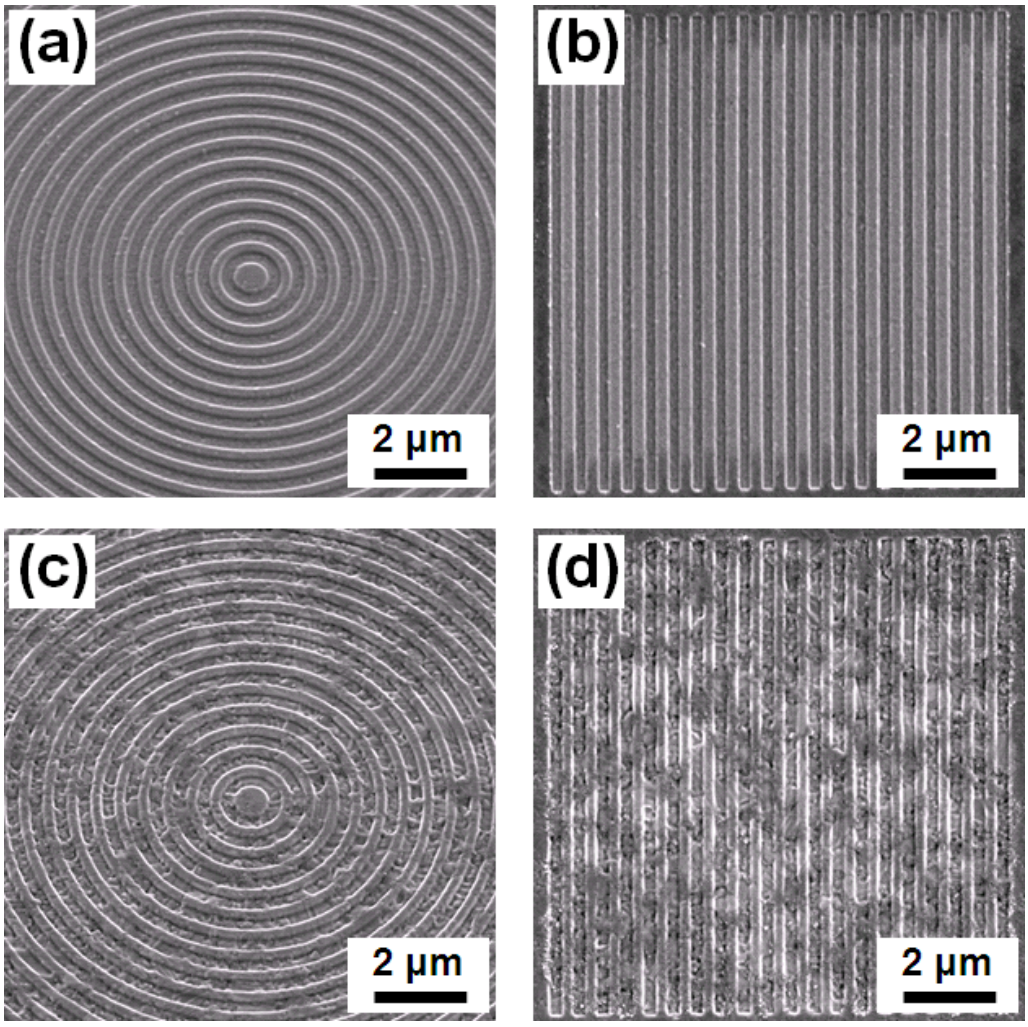

Figure 3.10 Scanning electron micrographs of nanostructures patterned on a single-crystalline Ag film (SC1) and a polycrystalline Ag film (PC1) via FIB milling. (a) Bull's eye and (b) grating structures on SC1. (c) Bull's eye and (d) grating structures on PC1. Images (a) and (c) were recorded with the sample tilted 30° from normal. The periodicity and milling depth of the structures are 580 and 60 nm, respectively.

while precise nanostructures could be obtained for SC1. Since epitaxial films have a highly-oriented, single-crystalline structure, the entire surface has essentially the same etching rate during FIB milling. Therefore, the milling depth of the patterned areas is almost identical across the surface, and the increase in surface roughness is limited. On the other hand, different etching rates of the randomly oriented grains in the polycrystalline films cause a variation in the milling depth across the patterned areas and, thus, a deterioration of the desired pattern.

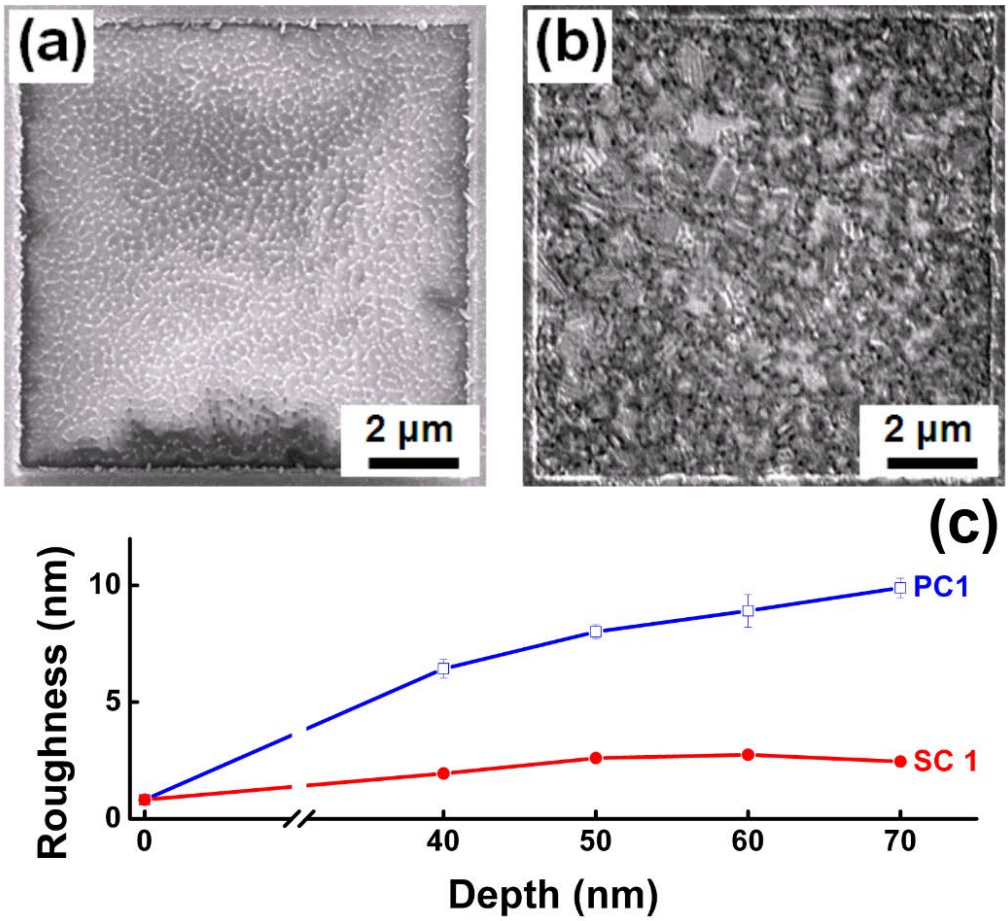

Figure 3.11 Scanning electron micrographs and roughness of squares patterned on (a) a single-crystalline Ag film (SC1) and (b) a polycrystalline Ag film (PC1) via FIB milling. The patterned area is 10 × 10 μm^2 and the depth is 60 nm. (c) The RMS surface roughness of the patterned area as a function of the milling depth. The error bars for SC1 are not shown as they are smaller than the size of the data points. Before patterning, both films have a nearly identical roughness of about 0.8 nm. At the depth of 60 nm, the roughness of the polycrystalline film (8.91 nm) is over three times that of the epitaxial film (2.74 nm). The RMS roughness was determined by averaging four 2.5 × 2.5 μm^2 AFM scans within each patterned square.

To quantify this difference, we patterned 10 × 10 μm^2 squares of different depths on both single-crystalline and polycrystalline films via FIB milling. The surface roughness of each square was then observed via AFM. As expected, for the same FIB milling conditions, the squares on SC1 and PC1 showed different surface morphologies. The squares on SC1 exhibited a more uniform surface (figure 3.11a), compared to the squares on PC1 (figure 3.11b). Figure 3.11c shows the measured RMS surface roughness as a function of the milling depth. Before patterning, both epitaxial (SC1) and polycrystalline (PC1) films had nearly identical surface roughness. With increasing milling depth, the surface roughness of the patterned area on both films increased. However, for the epitaxial film (SC1), the increase in roughness saturated at a depth of 60 nm, while the roughness of the polycrystalline film (PC1) continued to increase. As a result, when the milling depth is 60 nm or deeper, the roughness of the patterned area on PC1 is over three times larger than that on SC1. This shows that epitaxial films can provide more precisely patterned nanostructures as compared to the polycrystalline films. Such fine control is essential for accurate manipulation of SPPs with plasmonic devices.[28, 39]

3.3 Conclusions

Thus, we have demonstrated that epitaxially grown silver films can provide several key benefits for plasmonics. Using a standard dc magnetron sputtering system, single-crystalline films can be easily obtained that are extremely flat over large areas. Because this flatness occurs on both sides, these films can be useful for devices that utilize long-range plasmonic waveguides[43] or extraordinary optical transmission.[2] The metallic films also exhibit an improved dielectric function with higher conductivity and lower optical absorption compared to polycrystalline films. This can lead to an increase in the SPP propagation length. Furthermore, when the epitaxial films are patterned via FIB milling, precise single-crystalline nanostructures can be obtained. The resulting films can therefore allow the fabrication of plasmonic devices with enhanced performance.

3.4 Experimental Section

Preparation of epitaxial films.

Epitaxial films of silver were deposited on mica substrates via dc magnetron sputtering in a system with a base pressure lower than 5×10^{-8} Torr. The substrates were cleaved perpendicular to the c-axis to reveal smooth, clean surfaces, prior to deposition. Films were sputtered at an argon pressure of 6 mTorr and a dc power of 400 W to give a deposition rate of 1.65 nm/s at a source to substrate distance of 18 cm. Various substrate temperatures were used between room temperature and 500 °C. Films grown at room temperature were polycrystalline, though textured in the (111) direction, whereas films grown at temperatures higher than 300 °C were single crystalline. The surface roughness of the films was observed to be the lowest at 350 °C, and, thus, films grown at this temperature (samples SC1 and SC2) were used for this study.

Preparation of polycrystalline films.

200-nm-thick silver films were deposited on cleaned <100> silicon wafers by thermal evaporation. The thermal evaporator was housed inside a nitrogen-containing glove box to limit contamination of the silver films. During the deposition, the chamber pressure of the evaporator was maintained at about 10^{-6} Torr and the substrate temperature was in the range of 30-40 °C. The deposition rate of silver was 0.1-0.2 nm/s which was calibrated with a quartz crystal microbalance. To strip off the evaporated silver films, we applied either thermally-curable epoxy (EPO-TEK 377, Epoxy Technologies) or ultraviolet (UV)-curable epoxy (Norland Products, NOA 61) to the top of the films. To cure, each epoxy layer was treated at 150 °C for 1 h or exposed to a UV lamp for 3 h. The cured epoxy was employed as a backing layer of the silver films. After curing, the silver and epoxy bilayer was stripped from the silicon substrate after running a razor blade along the epoxy side of the film.

X-ray diffraction (XRD).

All films were characterized using a Bruker microdiffractometer equipped with a two-dimensional area detector to determine their microstructure. Five distinct Debye rings were observed in the area diffraction pattern of all polycrystalline films in the 2-theta range of 30°-85°, as expected from the powder diffraction pattern of Ag. The single-crystalline films, on the other hand, showed a single spot at the Ag(111) peak. In addition, high-resolution wide-angle XRD patterns, rocking curves, and grazing-incidence diffraction scans were obtained for single-crystalline Ag films using a Panalytical X'Pert Pro. Results obtained from these scans are discussed in the main text. Grazing-incidence X-ray reflectivity scans, also carried out on the X'Pert Pro, were used for thickness and roughness measurements.

Atomic force microscopy (AFM).

The atomic force microscope (Veeco Nanoscope IIIA multimode system) was housed inside an argon-containing glove box. The dry argon atmosphere was helpful to prevent contamination of the silver surfaces during the measurement and to observe the surface morphology accurately. All AFM images were obtained by using tapping mode at a scan rate of 0.5 Hz and the scanned area was $2.5 \times 2.5\ \mu m^2$. Nanoscope software was utilized to analyze the images and extract topographical information such as root mean square roughness.

Ellipsometry.

To measure the dielectric functions of the silver films, a multi-angle spectroscopic ellipsometer (V-VASE, J. A. Wollam Co.) was utilized. With a 75 W xenon lamp source, polarized incident light was scanned in the wavelength range from 450 to 750 nm, with an interval of 1 nm, and the reflected light was analyzed at incidence angles of 65, 70, and 75°. By using WVASE software (JA Woolam Co.), the dielectric functions were fitted with numerical iteration and the Fresnel equations. A two-layer model (air and Ag) with a perfectly flat interface was assumed. For all samples, the mean square errors,

representing the quality of the match between the measured and theoretically calculated dielectric functions, were less than 1, which implies good consistency between them.

Focused-ion-beam (FIB) milling.

The epitaxial and polycrystalline silver films were patterned using a dual-beam FEI Quanta 200 3D FIB workstation. The patterns, including slits, grooves, bull's eyes, gratings, and squares were etched using 30 kV as the acceleration voltage and 100 pA as the ion-beam current. The approximate spot size was 25 nm. The etched depth was controlled by the milling time.

Propagation length of surface plasmon polaritons (SPPs).

The method for the measurement of SPP propagation length has been described in a previous publication.[38] For each film, multiple slit-groove pairs were milled through the silver layer with FIB. Both the slit and the groove were approximately 200 nm wide and 40 μm long. Their separations were set at 10, 15, 20, 25, 30, 35, and 40 μm. Each sample was mounted on a Nikon TE 200 inverted microscope (20× objective, numerical aperture of 0.45) and illuminated on the mica or epoxy side of the films in transmission mode with light from a 250 W quartz tungsten halogen lamp focused by a condenser (numerical aperture of 0.1). SPPs were generated on the silver film when light transmitted through the slits. When the SPPs propagated along the silver surfaces and then struck the grooves, they scattered light that could be collected by the microscope. For each groove, we projected the image of the scattered light onto the entrance of an imaging monochromator (Triax 320, Jobin Yvon) and measured the spectrum with a liquid-nitrogen-cooled spectroscopic CCD camera (Princeton Instruments). Light that was directly transmitted through the slits was blocked at the entrance of the monochromator.

Plots of the scattered intensity versus slit-groove separation distance d for each wavelength were used to extract the wavelength dependence of the SPP propagation

length. Two methods were used, as discussed in the main text. In the first approach, the scattered intensity at each wavelength λ, $I(d,\lambda)$, was fit to the following equation,[24, 38]

$$I(d,\lambda) = I_o(\lambda)e^{-d/L_{SPP}(\lambda)} + I_b(\lambda), \quad (3.1)$$

where $I_o(\lambda)$ is the SPP intensity at the slit, $L_{SPP}(\lambda)$ is the SPP propagation length, and $I_b(\lambda)$ is the background intensity. The results for each film are shown in figure 3.8.

However, this formula underestimates the SPP propagation length because not all SPPs will propagate along the shortest path between the slit and groove.[22, 38] Light passing through the slit will launch SPPs in many directions. Depending on the geometry, some of these can reach the slit by travelling a distance greater than *d*. Therefore, a slit-groove pair with a shorter separation will lead to a larger amount of SPPs at the groove. This is due not only to the shorter distance but also a relatively larger acceptance angle. In other words, a groove closer to the slit can capture more propagating directions of the SPPs than a groove farther from the slit. This results in a larger detected intensity of the slit-groove pair at shorter distance, and thus the extracted SPP propagation length is underestimated.

Our second method tries to correct for this effect. To treat the problem exactly, one would need to know how efficiently the SPPs are launched from the slit in each direction. Because this angle dependence is not known, we assumed that SPPs are launched equally in all directions. For each slit-groove pair, we then calculated an average acceptance angle. In other words, we considered each point on the slit and calculated the range of angles that would reach the groove. This acceptance angle for each distance *d* was then averaged over the length of the slit to obtain $\bar{\theta}(d)$. After normalizing by the average acceptance angle at *d*=10 μm, $\bar{\theta}(10)$, Equation (3.1) can be corrected as,

$$I_{corrected}(d,\lambda) = \left[\frac{\bar{\theta}(d)}{\bar{\theta}(10)}\right] \cdot I_o(\lambda)e^{-d/L_{SPP}(\lambda)} + I_b(\lambda). \quad (3.2)$$

The results for each film using Equation (3.2) are shown in figure 3.7.

Effect of grain boundaries on the propagation length of SPPs.

The propagation length of SPPs on metallic films is limited by several loss mechanisms. These include: (i) ohmic losses in the metal, (ii) in-plane scattering, (iii) radiative scattering, and (iv) grain-boundary scattering. The overall SPP propagation length, L_{SPP}, can be obtained from[1, 38]

$$\frac{1}{L_{SPP}} = \frac{1}{L_{ohm}} + \frac{1}{L_{scat}} + \frac{1}{L_{rad}} + \frac{1}{L_{gb}}, \tag{3.3}$$

where L_{ohm}, L_{scat}, L_{rad}, and L_{gb}, are the ohmic, in-plane-scattering, radiative-scattering, and grain-boundary-scattering contributions, respectively. These individual contributions can be estimated from the following equations: [1, 24, 38]

$$L_{ohm} = \frac{c}{2\omega}\left[\mathrm{Im}\left(\sqrt{\frac{\varepsilon_m \varepsilon_d}{\varepsilon_m + \varepsilon_d}}\right)\right]^{-1}, \tag{3.4}$$

$$L_{scat} = \frac{2}{3}\frac{|\varepsilon_{m1}|}{(\omega/c)^5}\frac{1}{\sigma^2\delta^2}, \tag{3.5}$$

$$L_{rad} = \frac{3}{4}\frac{|\varepsilon_{m1}|^{1/2}}{(\omega/c)^5}\frac{1}{\sigma^2\delta^2}, \text{ and} \tag{3.6}$$

$$L_{gb} = \frac{g}{S_{gb}}, \tag{3.7}$$

where c is the speed of light, ω is the frequency of the SPP, ε_m is the dielectric function of the metal with real component ε_{m1}, ε_d is the dielectric function of the surrounding dielectric material (air in our case), δ and σ are the root mean square height and the lateral correlation length of the metal surface, g is the average grain size, and S_{gb} is the grain boundary scattering coefficient.

For each of our Ag films, we obtained the dielectric function via ellipsometry measurements. The surface morphology parameters (such as δ, σ, and g) were extracted from AFM images. L_{gb} for the single-crystalline films was assumed to be infinite. Thus, for films SC1 and SC2, L_{SPP} could be calculated from

$$\frac{1}{L_{SPP}} = \frac{1}{L_{ohm}} + \frac{1}{L_{scat}} + \frac{1}{L_{rad}} \tag{3.8}$$

and compared with the measurements shown in figure 3.7b and 3.7c. On average, the measured propagation lengths for SC1 and SC2 were lower by 20% and 50% of the predicted value, respectively. Unfortunately, these discrepancies complicate the analysis of the grain boundary scattering because the difference with theory is significant compared to the grain boundary contribution. Therefore, to obtain a rough estimate, we made a major assumption. Namely, we assumed that the theory and experiments would deviate by the same percentages in the polycrystalline films, PC1 and PC2. In other words, we calculated L_{SPP} for PC1 and PC2 using Equation (3.8), which ignores the presence of grain boundaries. These curves were then decreased by 20% and 50%, respectively. The results were fit to the measured propagation lengths for PC1 and PC2, using L_{gb} as a fitting parameter. Figure 3.9 shows the final fit. Using this procedure, L_{gb} was estimated to be 120 and 80 μm for PC1 and PC2, respectively. With these values for L_{gb} and the experimentally determined average grain sizes (180 and 140 nm for PC1 and PC2, respectively), the grain boundary scattering coefficients, S_{gb}, were also estimated. Values of 0.15% and 0.18% were obtained for PC1 and PC2, respectively. These scattering coefficients are comparable to a previously reported value (0.2%) for gold films.[24]

3.5 References

[1] H. Raether, *Surface Plasmons on Smooth and Rough Surfaces and on Gratings*. Springer-Verlag: Berlin, 1988.

[2] W. L. Barnes, A. Dereux, T. W. Ebbesen, "Surface Plasmon Subwavelength Optics," *Nature* **2003,** *424*, 824.

[3] H. A. Atwater, "The Promise of Plasmonics," *Sci. Am.* **2007,** *296*, 56.

[4] A. Polman, "Applied Physics: Plasmonics Applied," *Science* **2008,** *322*, 868.

[5] S. W. Bishnoi, C. J. Rozell, C. S. Levin, M. K. Gheith, B. R. Johnson, D. H. Johnson, N. J. Halas, "All-Optical Nanoscale pH Meter," *Nano Lett.* **2006,** *6*, 1687.

[6] A. Barhoumi, D. Zhang, F. Tam, N. J. Halas, "Surface-Enhanced Raman Spectroscopy of DNA," *J. Am. Chem. Soc.* **2008,** *130*, 5523.

[7] H. Im, K. C. Bantz, N. C. Lindquist, C. L. Haynes, S.-H. Oh, "Vertically Oriented Sub-10-nm Plasmonic Nanogap Arrays," *Nano Lett.* **2010,** *10*, 2231.

[8] A. G. Brolo, R. Gordon, B. Leathem, K. L. Kavanagh, "Surface Plasmon Sensor Based on the Enhanced Light Transmission through Arrays of Nanoholes in Gold Films," *Langmuir* **2004,** *20*, 4813.

[9] J. N. Anker, W. P. Hall, O. Lyandres, N. C. Shah, J. Zhao, R. P. Van Duyne, "Biosensing with Plasmonic Nanosensors," *Nat. Mater.* **2008,** *7*, 442.

[10] N. C. Lindquist, A. Lesuffleur, H. Im, S.-H. Oh, "Sub-Micron Resolution Surface Plasmon Resonance Imaging Enabled by Nanohole Arrays with Surrounding Bragg Mirrors for Enhanced Sensitivity and Isolation," *Lab Chip* **2009,** *9*, 382.

[11] M. I. Stockman, "Nanofocusing of Optical Energy in Tapered Plasmonic Waveguides," *Phys. Rev. Lett.* **2004,** *93*, 137404.

[12] E. Verhagen, L. Kuipers, A. Polman, "Enhanced Nonlinear Optical Effects with a Tapered Plasmonic Waveguide," *Nano Lett.* **2007,** *7*, 334.

[13] N. C. Lindquist, P. Nagpal, A. Lesuffleur, D. J. Norris, S.-H. Oh, "Three-Dimensional Plasmonic Nanofocusing," *Nano Lett.* **2010,** *10*, 1369.

[14] S. I. Bozhevolnyi, V. S. Volkov, E. Devaux, J. Y. Laluet, T. W. Ebbesen, "Channel Plasmon Subwavelength Waveguide Components Including Interferometers and Ring Resonators," *Nature* **2006,** *440*, 508.

[15] D. K. Gramotnev, S. I. Bozhevolnyi, "Plasmonics Beyond the Diffraction Limit," *Nat. Photonics* **2010,** *4*, 83.

[16] P. Mühlschlegel, H.-J. Eisler, O. J. F. Martin, B. Hecht, D. W. Pohl, "Resonant Optical Antennas," *Science* **2005,** *308*, 1607.

[17] L. Novotny, N. van Hulst, "Antennas for Light," *Nat. Photonics* **2011,** *5*, 83.

[18] W. A. Challener, C. Peng, A. V. Itagi, D. Karns, W. Peng, Y. Peng, X. Yang, X. Zhu, N. J. Gokemeijer, Y.-T. Hsia, G. Ju, R. E. Rottmayer, M. A. Seigler, E. C. Gage, "Heat-Assisted Magnetic Recording by a Near-Field Transducer with Efficient Optical Energy Transfer," *Nat. Photonics* **2009,** *3*, 220.

[19] M. Mansuripur, A. R. Zakharian, A. Lesuffleur, S.-H. Oh, R. J. Jones, N. C. Lindquist, H. Im, A. Kobyakov, J. V. Moloney, "Plasmonic Nano-Structures for Optical Data Storage," *Opt. Express* **2009,** *17*, 14001.

[20] H. A. Atwater, A. Polman, "Plasmonics for Improved Photovoltaic Devices," *Nat. Mater.* **2010,** *9*, 205.

[21] H. J. Lezec, A. Degiron, E. Devaux, R. A. Linke, L. Martin-Moreno, F. J. Garcia-Vidal, T. W. Ebbesen, "Beaming Light from a Subwavelength Aperture," *Science* **2002,** *297*, 820.

[22] J. T. van Wijngaarden, E. Verhagen, A. Polman, C. E. Ross, H. J. Lezec, H. A. Atwater, "Direct Imaging of Propagation and Damping of Near-Resonance Surface Plasmon Polaritons Using Cathodoluminescence Spectroscopy," *Appl. Phys. Lett.* **2006,** *88*, 221111.

[23] C. A. Volkert, A. M. Minor, "Focused Ion Beam Microscopy and Micromachining," *MRS Bull.* **2007,** *32*, 389.

[24] M. Kuttge, E. J. R. Vesseur, J. Verhoeven, H. J. Lezec, H. A. Atwater, A. Polman, "Loss Mechanisms of Surface Plasmon Polaritons on Gold Probed by Cathodoluminescence Imaging Spectroscopy," *Appl. Phys. Lett.* **2008,** *93*, 113110.

[25] H. Ditlbacher, A. Hohenau, D. Wagner, U. Kreibig, M. Rogers, F. Hofer, F. R. Aussenegg, J. R. Krenn, "Silver Nanowires as Surface Plasmon Resonators," *Phys. Rev. Lett.* **2005,** *95*, 257403.

[26] A. W. Sanders, D. A. Routenberg, B. J. Wiley, Y. Xia, E. R. Dufresne, M. A. Reed, "Observation of Plasmon Propagation, Redirection, and Fan-Out in Silver Nanowires," *Nano Lett.* **2006,** *6*, 1822.

[27] M. Allione, V. V. Temnov, Y. Fedutik, U. Woggon, M. V. Artemyev, "Surface Plasmon Mediated Interference Phenomena in Low-Q Silver Nanowire Cavities," *Nano Lett.* **2008,** *8*, 31.

[28] J.-S. Huang, V. Callegari, P. Geisler, C. Brüning, J. Kern, J. C. Prangsma, X. Wu, T. Feichtner, J. Ziegler, P. Weinmann, M. Kamp, A. Forchel, P. Biagioni, U. Sennhauser, B. Hecht, "Atomically Flat Single-Crystalline Gold Nanostructures for Plasmonic Nanocircuitry," *Nat. Commun.* **2010,** *1*, 150.

[29] B. Wild, L. Cao, Y. Sun, B. P. Khanal, E. R. Zubarev, S. K. Gray, N. F. Scherer, M. Pelton, "Propagation Lengths and Group Velocities of Plasmons in Chemically Synthesized Gold and Silver Nanowires," *ACS Nano* **2012,** *6*, 472.

[30] B. J. Wiley, D. J. Lipomi, J. Bao, F. Capasso, G. M. Whitesides, "Fabrication of Surface Plasmon Resonators by Nanoskiving Single-Crystalline Gold Microplates," *Nano Lett.* **2008,** *8*, 3023.

[31] J. A. DeRose, T. Thundat, L. A. Nagahara, S. M. Lindsay, "Gold Grown Epitaxially on Mica: Conditions for Large Area Flat Faces," *Surf. Sci.* **1991,** *256*, 102.

[32] K. Reichelt, H. O. Lutz, "Hetero-Epitaxial Growth of Vacuum Evaporated Silver and Gold," *J. Cryst. Growth* **1971,** *10*, 103.

[33] A. A. Baski, H. Fuchs, "Epitaxial Growth of Silver on Mica as Studied by AFM and STM," *Surf. Sci.* **1994,** *313*, 275.

[34] H. Bialas, K. Heneka, "Epitaxy of FCC Metals on Dielectric Substrates," *Vacuum* **1994,** *45*, 79.

[35] T.-B. Hur, H. K. Kim, J. Blachere, "Epitaxial Growth of Ag Films on Native-Oxide-Covered Si Substrates," *Phys. Rev. B* **2007,** *75*, 205306.

[36] M. Hegner, P. Wagner, G. Semenza, "Ultralarge Atomically Flat Template-Stripped Au Surfaces for Scanning Probe Microscopy," *Surf. Sci.* **1993,** *291*, 39.

[37] C.-H. Sun, N. C. Linn, P. Jiang, "Templated Fabrication of Periodic Metallic Nanopyramid Arrays," *Chem. Mater.* **2007,** *19*, 4551.

[38] P. Nagpal, N. C. Lindquist, S.-H. Oh, D. J. Norris, "Ultrasmooth Patterned Metals for Plasmonics and Metamaterials," *Science* **2009,** *325*, 594.

[39] N. C. Lindquist, T. W. Johnson, D. J. Norris, S.-H. Oh, "Monolithic Integration of Continuously Tunable Plasmonic Nanostructures," *Nano Lett.* **2011,** *11*, 3526.

[40] J. H. Park, P. Nagpal, S.-H. Oh, D. J. Norris, "Improved Dielectric Functions in Metallic Films Obtained via Template Stripping," *Appl. Phys. Lett.* **2012,** *100*, 081105.

[41] V. V. Temnov, U. Woggon, J. Dintinger, E. Devaux, T. W. Ebbesen, "Surface Plasmon Interferometry: Measuring Group Velocity of Surface Plasmons," *Opt. Lett.* **2007,** *32*, 1235.

[42] E. J. R. Vesseur, R. de Waele, H. J. Lezec, H. A. Atwater, F. J. G. de Abajo, A. Polman, "Surface Plasmon Polariton Modes in a Single-Crystal Au Nanoresonator Fabricated Using Focused-Ion-Beam Milling," *Appl. Phys. Lett.* **2008,** *92*, 083110.

[43] I. De Leon, P. Berini, "Amplification of Long-Range Surface Plasmons by a Dipolar Gain Medium," *Nat. Photonics* **2010,** *4*, 382.

Chapter 4.
Fabrication of Smooth Patterned Structures of Refractory Metals, Semiconductors, and Oxides via Template Stripping*

The template-stripping method can offer smooth patterned films without surface contamination. However, the process is typically limited to noble metals such as silver and gold because other materials cannot be readily stripped from silicon templates due to strong adhesion. Herein, we report an improved template-stripping method that can be extended to a large variety of materials including refractory metals, semiconductors, and oxides. To address the adhesion issue, we introduce a thin noble-metal layer between the template and the deposited materials. After peeling off all of the deposited materials from the template, the noble-metal layer can be selectively removed via wet etching. Thus, smooth patterned films of any desired material can be obtained. Further, we demonstrate template-stripped multilayer structures which have potential applications for photovoltaics and solar absorbers. In other words, an entire patterned device, *e.g.* which includes a transparent conductor, semiconductor absorber, and back contact, can be fabricated. Since our approach can simply reproduce the patterned films and multilayer structures with nanometer-scale fidelity via reuse of the template, a low-cost and high-throughput process in micro- and nanofabrication is provided that is highly favorable for electronics, plasmonics, and nanophotonics.

* The main portion of this chapter has been prepared for submission as Jong Hyuk Park, Prashant Nagpal, Kevin M. McPeak, Nathan C. Lindquist, Sang-Hyun Oh, and David J. Norris, "Fabrication of Smooth Patterned Structures of Refractory Metals, Semiconductors, and Oxides via Template Stripping."

4.1 Introduction

Numerous patterning techniques have been developed to prepare nanostructured materials.[1-2] However, despite significant progress, some applications would still benefit from improved methods. For example, many techniques rely on the patterning of polymers with electron-beam lithography,[3-4] block-copolymer lithography,[5-6] or nanoimprinting,[7-8] or on microcontact printing with self-assembled molecular monolayers.[9-10] The polymer or monolayer is then used as a mask and the pattern is transferred into the actual material with ion etching. Unfortunately, even after the removal of this mask, residual carbon deposits can remain that can be detrimental. Moreover, the etching process, which relies on high-energy ions to remove material, can degrade the mechanical, electronic, or optical properties of the final structure. In particular, ions can roughen the surfaces or be embedded in the material, both of which can increase optical and electronic losses.[2, 11] Finally, since each individual device is patterned separately, nanometer-scale differences can lead to sample-to-sample variations. Therefore, low-cost, high-throughput nanofabrication methods that avoid these problems are still needed to obtain nanostructured films for optical and electronic applications.

Recently, template stripping has been explored as a possible route.[11-15] This process deposits a thin film of a coinage metal, such as silver or gold, on a pre-patterned silicon substrate. Since these metals can wet the native oxide on the Si, but adhere poorly, the film can be peeled off, revealing a smooth inverted replica of the original patterned template. This approach is not only simple but can exploit several key advantages. First, the sophisticated patterning techniques developed for Si can be utilized to form the template. Second, after removal of the patterned metal film, the template can be reused many times,[11] resulting in a low-cost, high-throughput process. Third, because the metal is not directly patterned (*e.g.* via ion etching with a polymer mask) contamination and degradation can be completely avoided.

In the field of plasmonics, these advantages can be important because the pattern is used to manipulate electromagnetic waves known as surface plasmon polaritons.[16]

Template stripping can provide extremely smooth patterned films of pure metals with low loss, leading to better performance.[11] In particular, surface roughness that can scatter surface plasmon polaritons is greatly reduced.[15, 17] Silver and gold are also among the best available materials for many plasmonic applications. Consequently, the restriction of template stripping to such metals is typically not an issue.

However, in other areas this restriction can be problematic. For example, in photovoltaics, nanostructured films have been explored to enhance light absorption through reflecting, channeling, or concentrating sunlight.[18-20] To obtain practical devices, the technique used to introduce the nanostructure must be inexpensive and able to handle large areas. Template stripping could potentially provide a solution, but the use of Ag or Au would increase cost. Other materials, such as Al or metal oxides, could avoid this problem. However, since these materials adhere to a Si substrate, structured films cannot be directly obtained from them via template stripping.

Another example is in thermophotovoltaic devices, where nanostructured films are used to absorb energy from a hot object, such as the sun, and then re-radiate thermal emission that can be converted into electricity by a photocell.[21-25] The goal of the film is to convert the broadband emission from the hot object into a narrower spectrum that is better matched to the photocell. Since the nanostructured film must sustain elevated temperatures (typically above 1000 ˚C), it must be fabricated from a refractory material (*e.g.* tungsten). Patterning of such materials through conventional methods can present challenges, as discussed further below. Template stripping could again potentially provide a solution. However, due to adhesion of refractory materials to Si substrates, template stripping with such materials has not yet been demonstrated.

Here, we present a simple scheme to expand template stripping beyond the coinage metals to obtain structures for a broader set of applications. Our approach allows smooth patterning of thin films of refractory metals, semiconductors, and oxides while maintaining all of the advantages of template stripping discussed above. Consequently, the resulting films can exhibit properties better than those made via conventional patterning techniques. In addition, multilayered stacks of various combinations of

materials can be fabricated. Thus, our approach provides a useful tool for low-cost, high-throughput fabrication for various applications.

4.2 Results and Discussion

While metals such as Ag and Au can be easily peeled off oxide substrates such as mica, glass, and oxidized Si,[11-12] refractory metals, semiconductors, and oxides have been regarded as non-strippable due to their strong adhesion to these substrates. To address this problem, we introduce a thin film of a strippable metal as a release layer between the substrate and the desired material.[13] Although many metals such as Ag, Au, Cu, or Pd could be employed, we use a Au film because its top surface shows very low roughness, leading to smoother surfaces in the final structure.

As shown in figure 4.1, the procedure begins by patterning the inverse of the desired structure on the substrate (figure 4.1a). A thin Au layer is then deposited (figure 4.1b), followed by the deposition of the desired material (figure 4.1c). Because Au has a high surface energy, the desired material will be more conformal than if deposited on a polymer. The two layers (Au and desired material) are then peeled off the patterned substrate (figure 4.1e) using a backing layer. Typically this is a flexible adhesive polymer (like epoxy or polydimethylsiloxane). For high temperature applications, where the final structure should not contain any organic materials, the backing layer can be made from an electrodeposited metal (such as nickel) or a dissolvable material (such as glucose) that can be easily removed to yield a free-standing structure. In any case, a counter-substrate (like a glass or Si wafer) can be attached to the backing layer before stripping if additional structural stability is required. Since the Au release layer adheres poorly to the template, but sticks to the desired material, the two layers can be easily stripped together. Afterwards, the Au can be selectively removed with a wet etchant such that a patterned structure of the desired material is obtained (figure 4.1f). The Au can be recycled if desired.

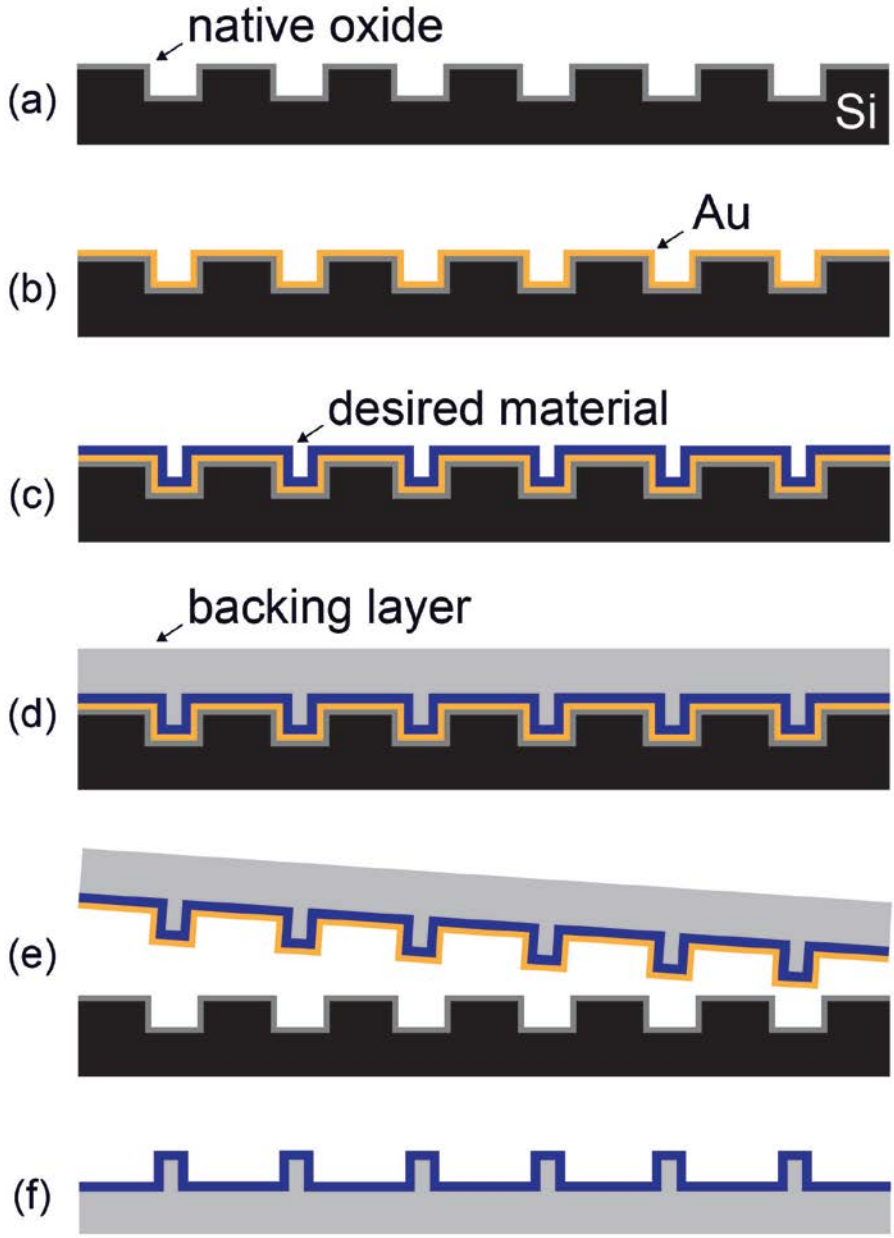

Figure 4.1 Schematic for the template-stripping approach with a release layer. (a) A silicon (Si) template is patterned by conventional fabrication techniques. (b) A thin gold (Au) layer is deposited on the native oxide of the template. (c) A layer of the desired material is subsequently deposited on the Au. (d) A backing layer is added to the top surface of the deposited films. (e) All of the layers are stripped from the template. (f) The Au is selectively removed by wet etching and can be recycled if necessary.

The surface morphology of the final structure is largely determined by the top surface of the Au release layer. Although very thin Au films can be extremely smooth, if the Au is too thin, it may not completely cover the template and the desired material may not strip off. To avoid this, we first determined the optimal thickness of the Au layer (~20 nm). Figure 4.2a shows the surface morphology of the top surface of such a Au film. The root mean square (RMS) roughness of this surface was quantified with atomic force microscopy (AFM). The Au has a slightly larger roughness, 0.39 nm, than the original Si substrate, 0.16 nm (figure 4.3).

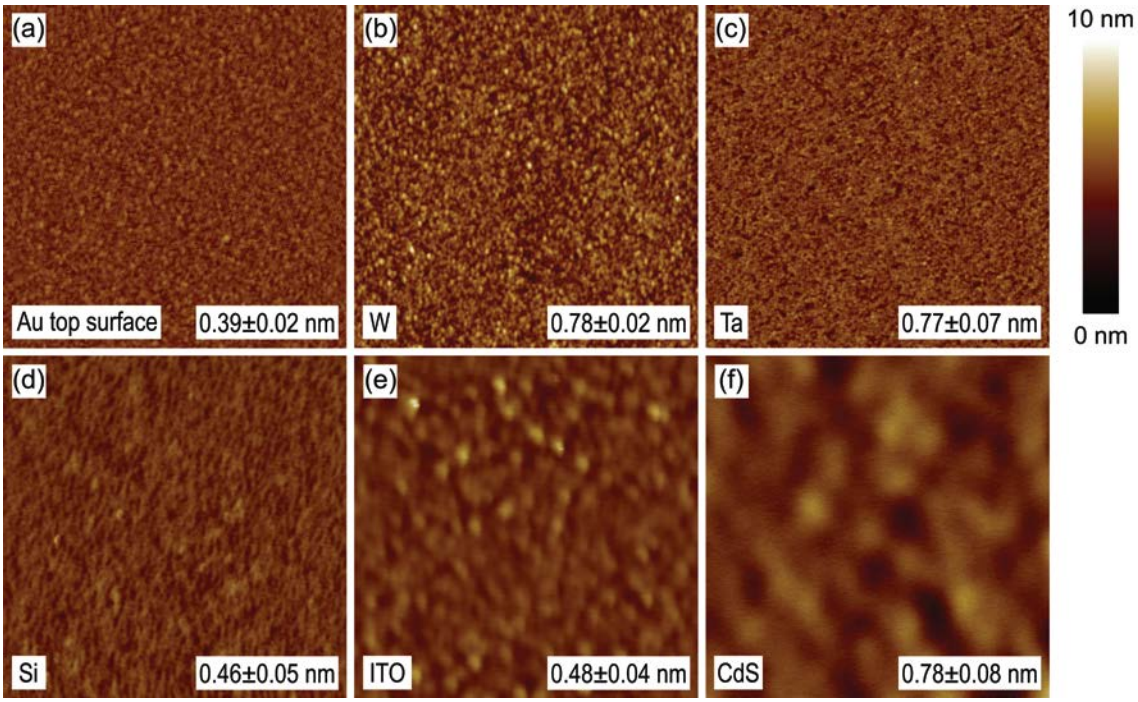

Figure 4.2 AFM images of flat surfaces for determining surface roughness. (a) Top surface of a 20-nm-thick gold (Au) film. Template-stripped (b) tungsten (W), (c) tantalum (Ta), (d) silicon (Si), (e) indium tin oxide (ITO), and (f) cadmium sulfide (CdS) surfaces. Each image includes the extracted RMS roughness from the 2.5 × 2.5 μm^2 scanned area.

The effectiveness of such a Au release layer was tested by fabricating flat films of various materials via template stripping. W, Ta, Si, indium tin oxide (ITO), or cadmium sulfide (CdS) was deposited on the Au via sputtering or chemical bath deposition[26-27] (see Experimental Section). To remove the Au after template stripping, a wet etchant

containing potassium iodide and iodine was typically used. However, since CdS is also attacked by this etchant, a potassium hydroxide (KOH) and potassium cyanide solution was utilized in this case.[28] Figure 4.2 shows the surface morphology of the flat template-stripped films. All materials exhibit smooth surfaces with an RMS roughness below 0.8 nm. This level of roughness is difficult to achieve in these materials with conventional deposition approaches.

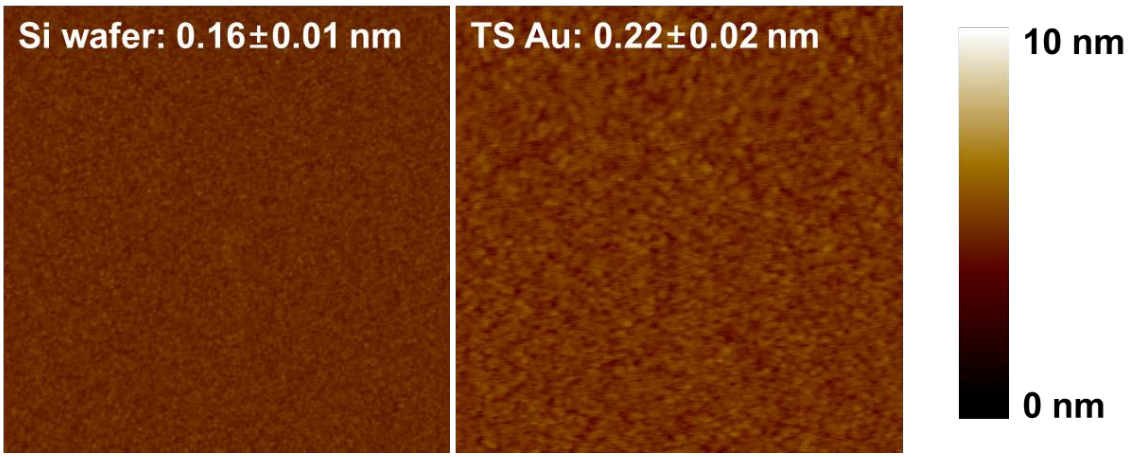

Figure 4.3 AFM images of the silicon (Si) wafer (left panel) and a gold (Au) film template-stripped (TS) from it (right panel). For each surface the RMS roughness is provided: 0.16 and 0.22 nm, respectively. The Au film is 20 nm thick. The scanned areas are 2.5 × 2.5 μm^2.

These template-stripped films were characterized with X-ray photoelectron spectroscopy (XPS) to detect the surface impurities such as residual Au. Figure 4.4 exhibits the XPS spectra for the template-stripped films of W and Ta. As shown in the wide-scan survey spectra (figure 4.4a and 4.4c), most peaks indicate the main element of the films and Au peaks are not observed. To confirm this result, a high-resolution spectrum was obtained in the range of 80-95 eV where the Au4f peaks exist. The Au peaks are not detected at all in the spectrum (figure 4.4b and 4.4d). This implies that the Au release layer was completely removed via the etching process. Figure 4.5 shows the XPS spectra for the template-stripped films of Si, ITO, and CdS. Likewise, no Au peaks are found in both wide-scan survey spectra and high-resolution spectra. Consequently, all these template-stripped films can have pure surfaces without residual Au.

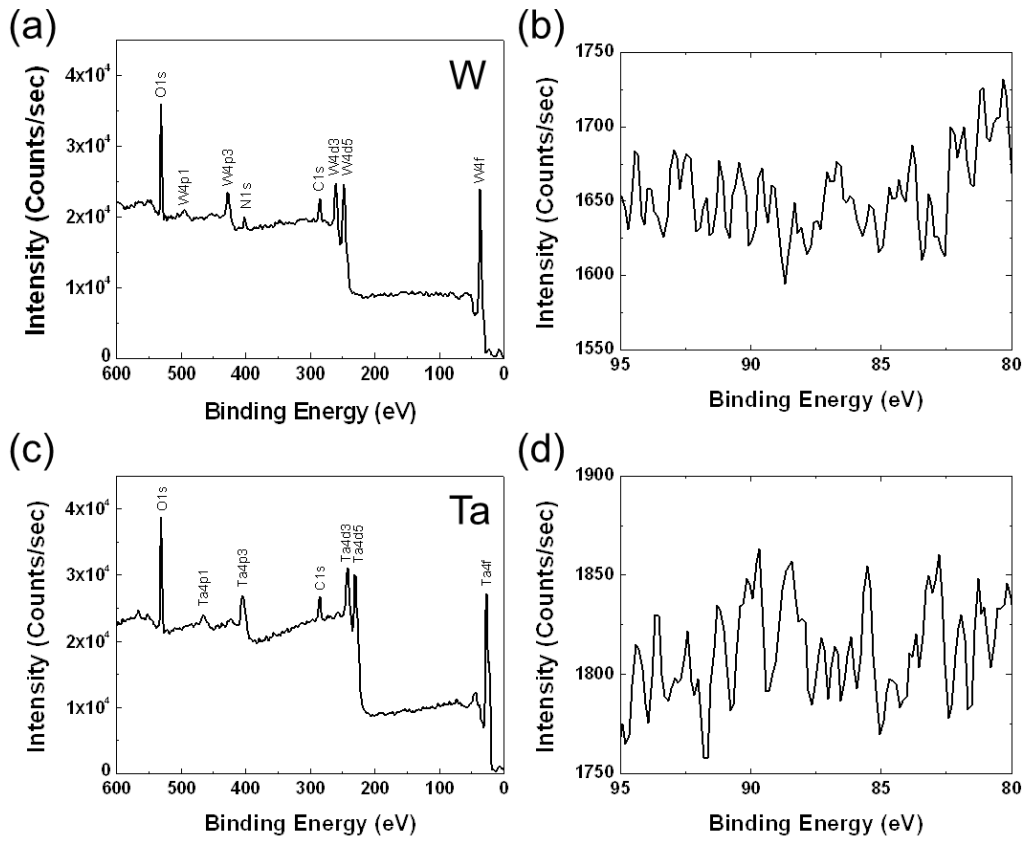

Figure 4.4 XPS spectra for template-stripped surfaces of tungsten (W) and tantalum (Ta) films. A wide-scan survey spectrum of the template-stripped (a) W and (c) Ta films. Each image contains the peak annotation. A high-resolution spectrum of the template-stripped (b) W and (d) Ta films for detecting Au4f peaks. Au peaks are not observed.

In addition to the flat films, the same strategy can be exploited to obtain patterned structures. For example, figure 4.6a and 4.6b demonstrates a W bull's-eye pattern obtained with this approach. Conventionally, such metal structures would be patterned with reactive-ion etching (RIE), ion milling, or focused-ion-beam (FIB) milling. However, this typically leads to large surface roughness due to the polycrystallinity of the metal. Namely, grains that are oriented in different directions etch at different rates.[29-30] Indeed, as shown in figure 4.6c and 4.6d, a W bull's-eye structure fabricated by RIE exhibits very rough surfaces, especially in the etched grooves. In comparison, the template-stripped structure has smooth surfaces (figure 4.6a and 4.6b), similar to those previously demonstrated for Ag and Au.[11]

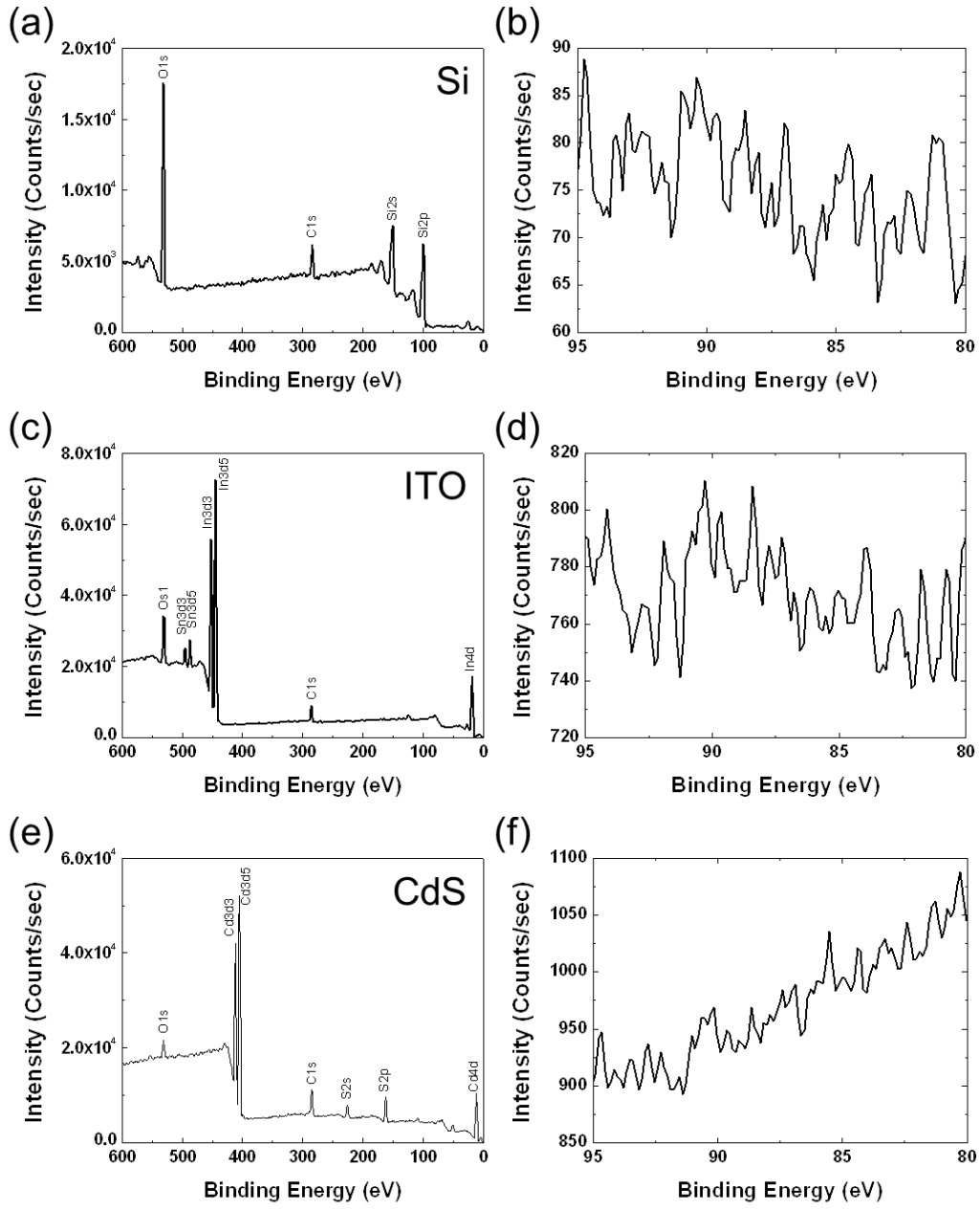

Figure 4.5 XPS spectra for template-stripped surfaces of silicon (Si), indium tin oxide (ITO), and cadmium sulfide (CdS) films. A wide-scan survey spectrum of the template-stripped (a) Si, (c) ITO and (e) CdS films. Each image contains the peak annotation. A high-resolution spectrum of the template-stripped (b) Si, (d) ITO and (f) CdS films for detecting Au4f peaks. Au peaks are not observed.

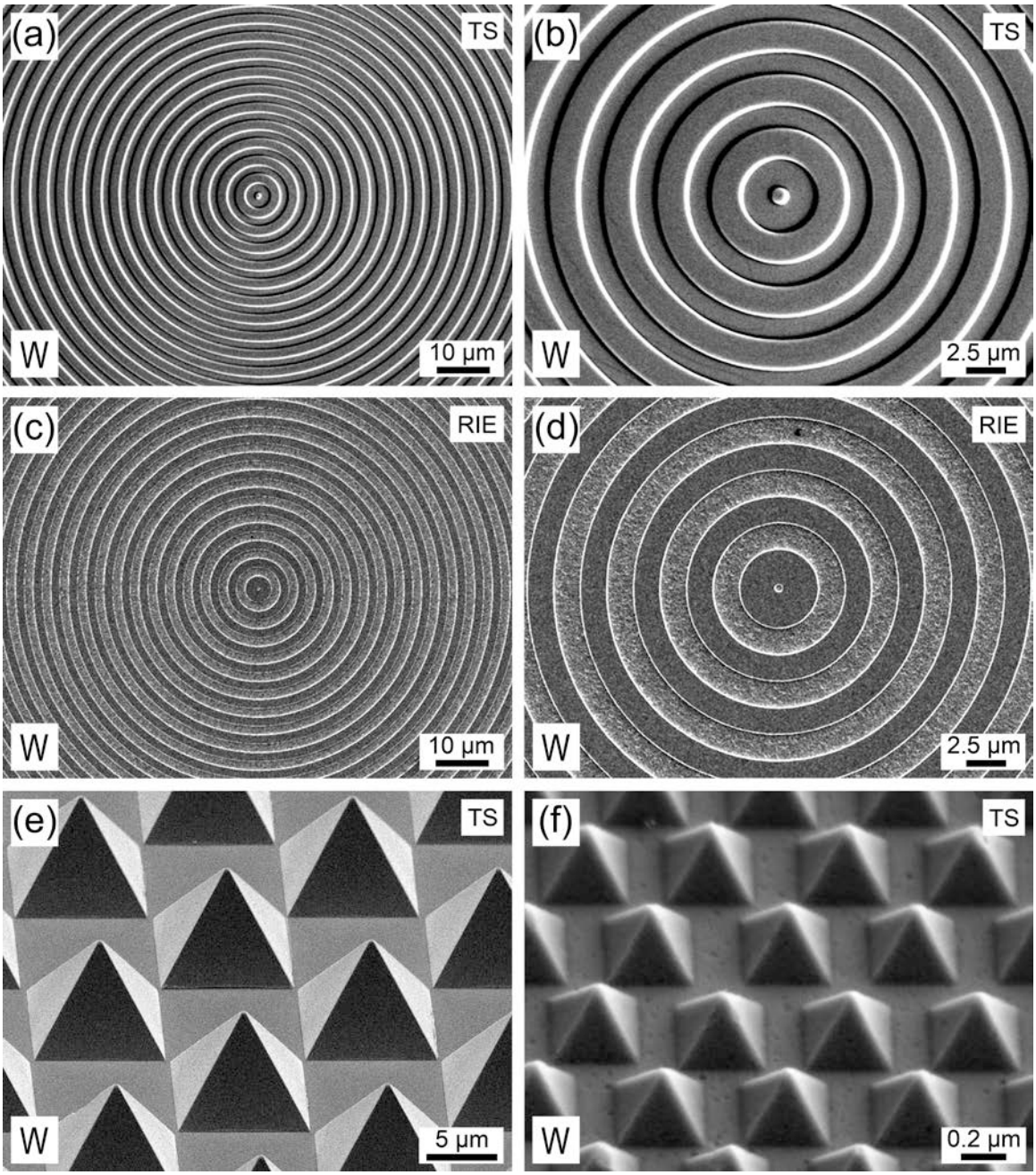

Figure 4.6 Scanning electron micrographs of tungsten (W) structures. (a) and (b) show a bull's-eye pattern prepared via template stripping (TS). (c) and (d) show a bull's-eye pattern made via conventional reactive-ion etching (RIE) for comparison. Both bull's-eye structures have a groove periodicity of 3.5 μm and a groove depth of ~200 nm. (e) Micro- and (f) nanoscale pyramid arrays prepared by TS. The pyramids have a base length of ~9 μm and 350 nm, respectively.

This is quantified in figure 4.7, which compares the surface morphology of the W bull's-eye structures obtained via RIE with those from template stripping. The RIE sample was obtained by first depositing a W film on a flat silicon substrate via sputtering. Before patterning, the W film had a nominal RMS roughness of about 2 nm on its exposed surface. The pattern was then created by etching this surface with RIE. As this etching proceeds, the surface roughness of the patterned area increases as shown in figure 4.7a and 4.7b. The final RMS roughness in the 200-nm-deep grooves is about 10 nm. This increase cannot be avoided due to the polycrystallinity of the metal.

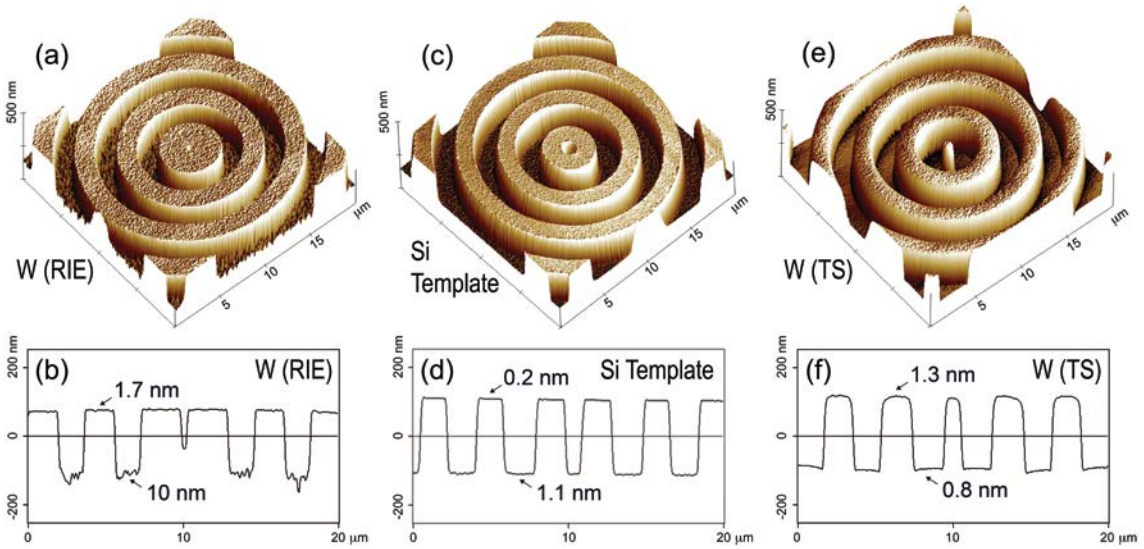

Figure 4.7 Surface morphology comparison. Three-dimensional AFM images of (a) a tungsten (W) bull's-eye pattern obtained from direct RIE of a W film, (c) a silicon (Si) bull's-eye pattern obtained from direct RIE of a Si wafer, and (e) a W bull's-eye pattern obtained via template stripping from the Si template. (b), (d), and (f) show the cross-sectional profile of each structure with the extracted RMS roughness at the top or bottom of the grooves.

However, a single-crystalline substrate like a Si wafer exhibits much more uniform etching, leading to smoothly patterned surfaces.[30] Figure 4.7c and 4.7d shows the same bull's-eye pattern in Si obtained via RIE. The RMS roughness at the bottom of the grooves is 10× smaller than for those directly patterned in the W. Consequently, when this Si is used as a template for W deposition, a template-stripped W bull's eye that is much smoother is fabricated (figure 4.7e, 4.7f, and 4.8). The RMS roughness in the

grooves and on the top flats was only 0.8 and 1.3 nm, respectively. This implies that the template-stripped structures should exhibit lower optical and electronic losses. If such refractory structures are used for thermophotovoltaic applications, this can lead to better performance.[31]

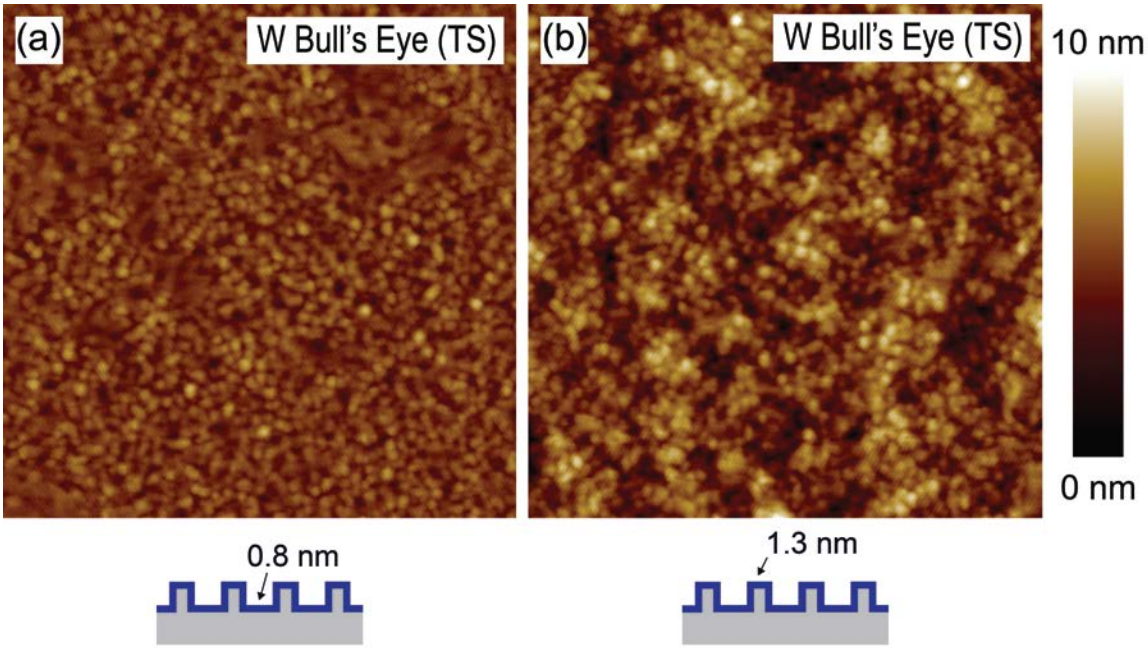

Figure 4.8 AFM images of template-stripped (TS) tungsten (W) bull's-eye structures. The surfaces of (a) the groove and (b) the top flats were separately characterized. These surfaces exhibited a root mean square roughness of ca. 0.8 and 1.3 nm, respectively. The scanned areas are $1 \times 1\ \mu m^2$.

As already mentioned, one advantage of template stripping is that it allows surface contamination to be avoided. Conventional patterning with RIE or FIB frequently leads to embedded ions.[2, 11, 32] Above, we used XPS to demonstrate that Au contamination from the release layer could be avoided with template stripping. For the patterned films we also routinely used energy dispersive X-ray spectroscopy (EDS) to confirm that the Au was eliminated. As shown in figure 4.9a, we could not detect any impurities, including residual Au, on the surface of template-stripped W bull's eyes.

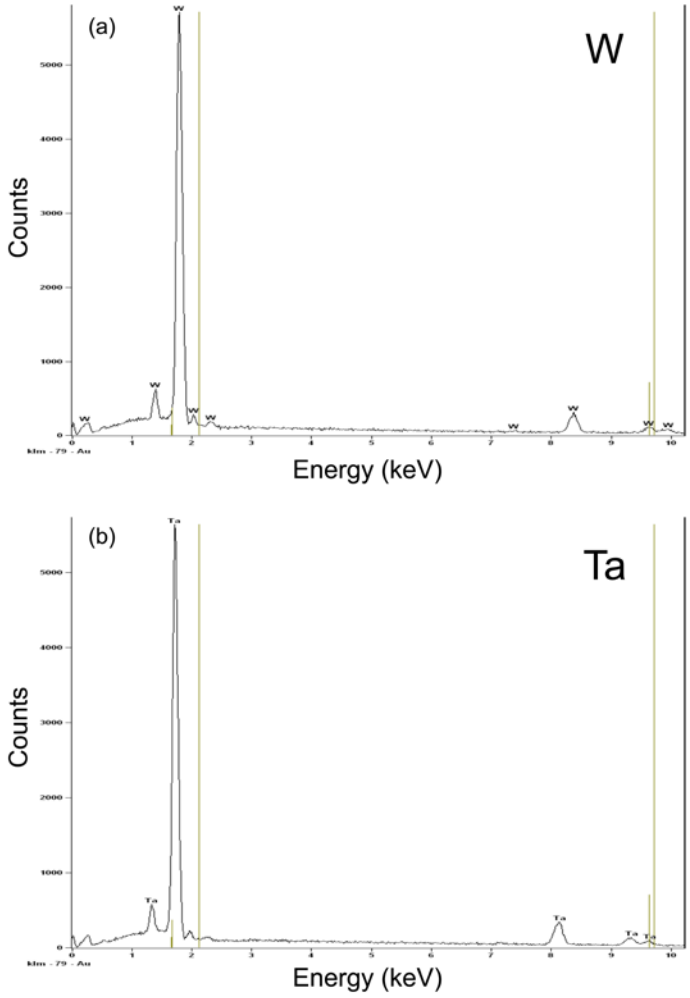

Figure 4.9 EDS spectra from template-stripped (a) tungsten (W) and (b) tantalum (Ta) bull's-eye structures. The vertical lines in the graphs indicate the peak positions of gold. After removing the gold layer, only the desired element was observed without detectable surface contamination. The electron-beam acceleration voltage was 10 kV.

In addition to bull's-eye patterns, arrays of W pyramids were fabricated via template stripping. Such structures have been discussed for their potential application as omnidirectional solar absorbers.[33] To prepare suitable templates, we utilized anisotropic etching of Si (100) wafers with KOH.[34] Using photolithography or nanosphere lithography, arrays of micro- or nano-scale holes were formed in a Cr layer on the Si substrate, respectively.[11, 13] These holes were used as the mask for the anisotropic etch, which induced pyramidal etch pits in the Si. The deposition of Au and W layers, template

stripping, and wet etching then followed. Figure 4.6e and 4.6f shows the smooth tapered W micro- and nanopyramids obtained. As predicted by previous theoretical calculations,[33] the W nanopyramid arrays exhibit much higher absorptivity for visible wavelengths compared to a flat W film (figure 4.10). The taper of the nanopyramids reduces the impedance mismatch for incoming light at the W-air interface, which leads to lower reflectivity and higher absorptivity.

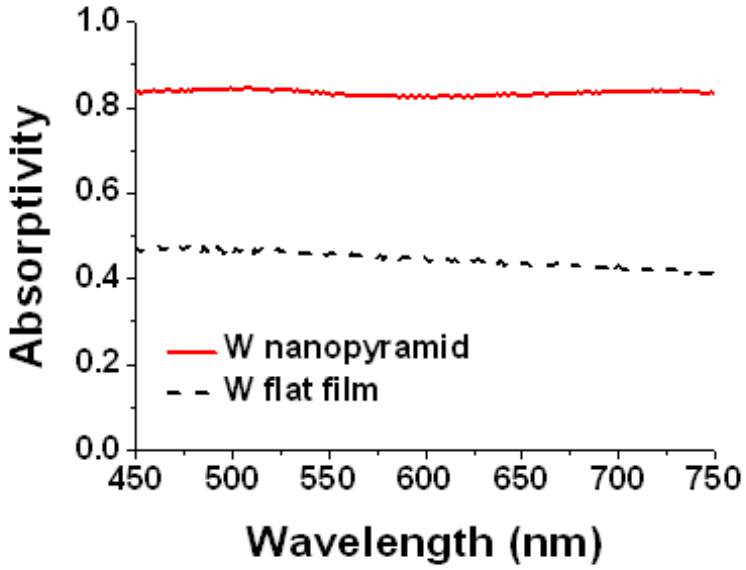

Figure 4.10 Absorption enhancement for tungsten (W) nanopyramid films fabricated by template stripping compared to flat tungsten films. Here, absorptivity is estimated from 1-*R*, where *R* is the reflectivity. Thus, this neglects the effect of high-angle scattering that is not collected by the high-numerical-aperture (0.9) objective used in the experiment.

In addition to W, a large variety of materials can be patterned with this template-stripping approach. In the field of micro- and nanofabrication, dry etching is typically used to pattern materials such as refractory metals and oxides, which have a high melting point and stiff elastic modulus. However, the etching process can be affected by many factors, including the mechanical and chemical properties of the material; its crystalline structure, grain orientation, and surface purity; and even the history of the etching chamber. Thus, it is difficult to control patterns on the nanometer scale. In contrast, since

our template-stripping method utilizes etching of silicon, which is extremely well developed, accurate control of the same pattern is possible for many materials. Figure 4.11 shows bull's-eye structure made from Ta, Si, ITO, and CdS via template stripping. In all cases, we used EDS to confirm that the Au was removed by wet etching (figure 4.9b and 4.12). All of the bull's-eye structures were prepared with exactly the same groove periodicity (3.5 μm). The groove depth was adjusted from 150 to 300 nm via fine-tuning of the template. Precisely patterned structures with smooth surfaces made from such semiconductors and oxides can be highly useful in the fabrication of various devices including structured semiconductor solar cells[18] and plasmonic devices of transparent conducting oxides.[35]

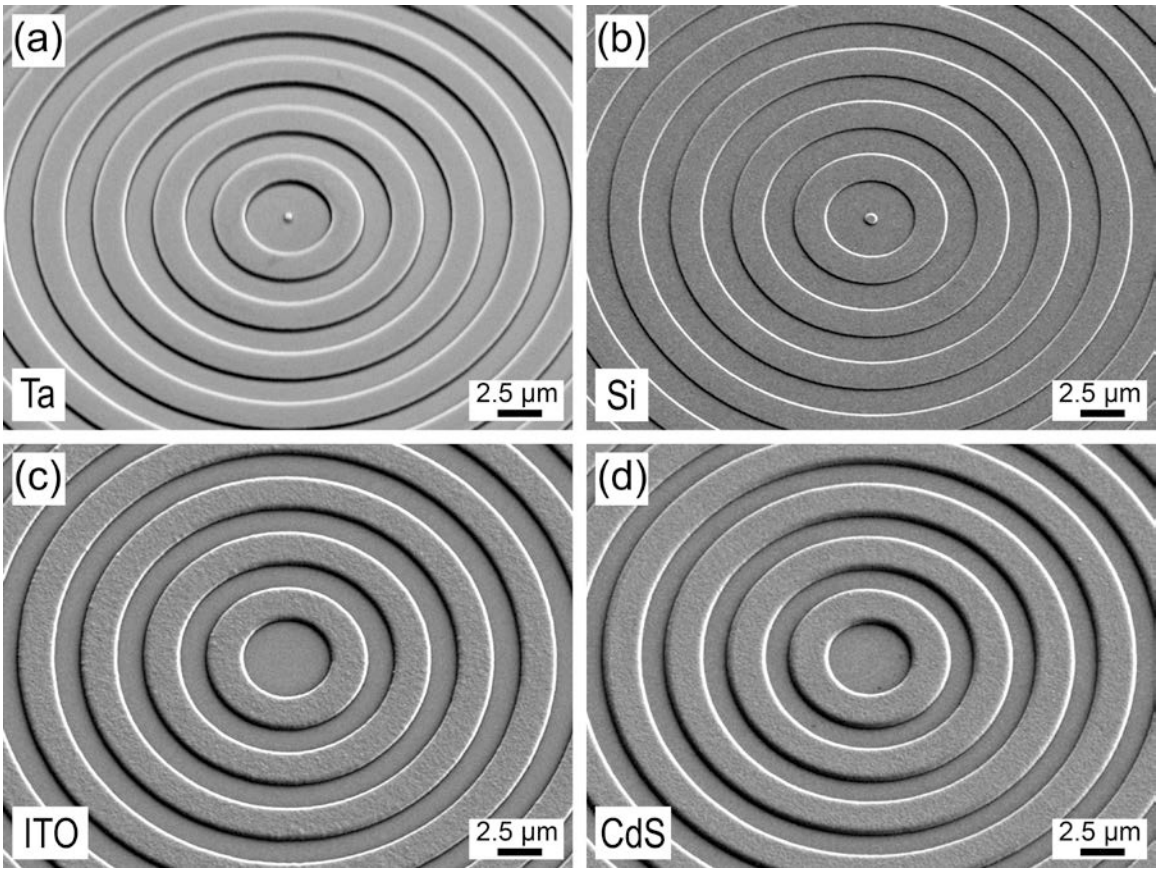

Figure 4.11 Scanning electron micrographs of bull's-eye patterns of (a) tantalum (Ta), (b) silicon (Si), (c) indium tin oxide (ITO), and (d) cadmium sulfide (CdS). The structures all have a 3.5 μm groove periodicity with groove depths from 150 to 300 nm. The images were taken with the sample tilted 30° from normal.

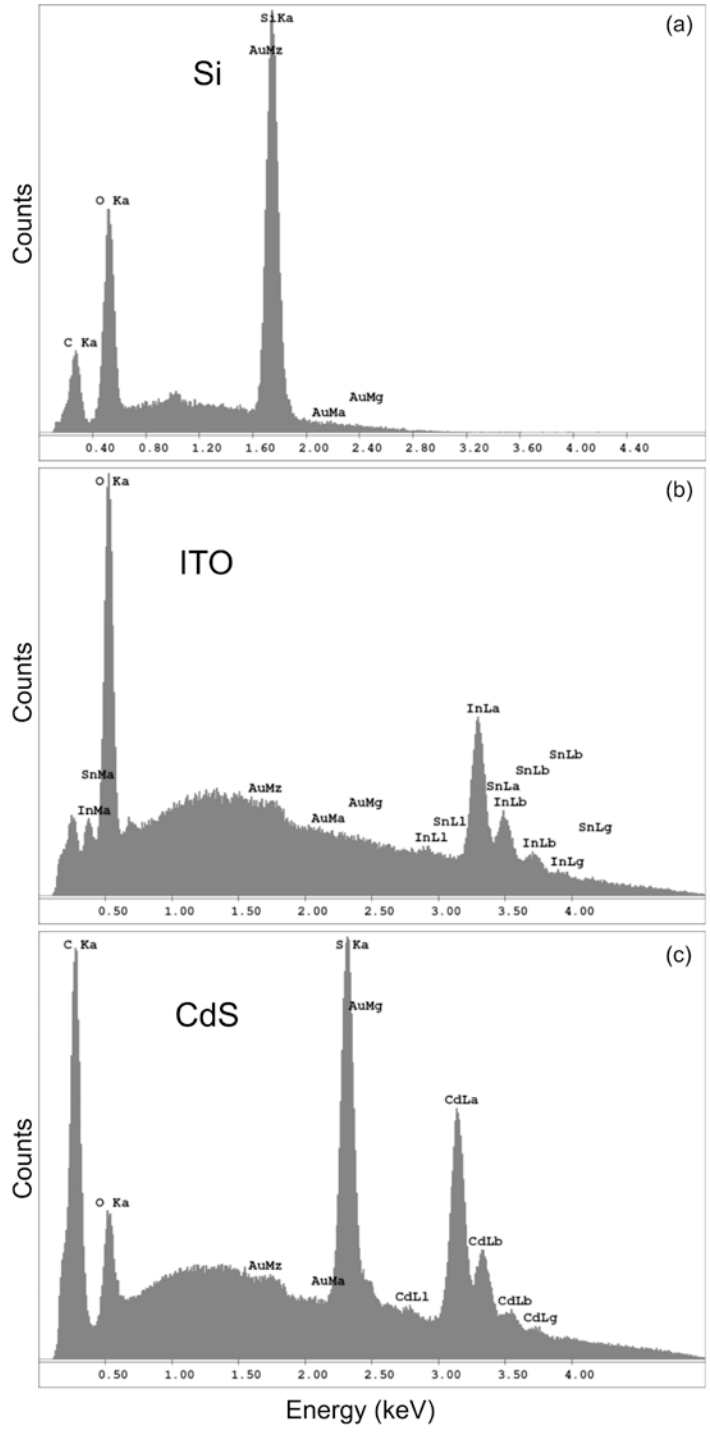

Figure 4.12 EDS spectra from template-stripped (a) silicon (Si), (b) indium tin oxide (ITO), and (c) cadmium sulfide (CdS) bull's-eye structures. Each peak is labeled by the responsible atomic transition. The position of Au transitions is also indicated, but no discernible gold peaks were detected. The electron-beam acceleration voltage was 5 kV.

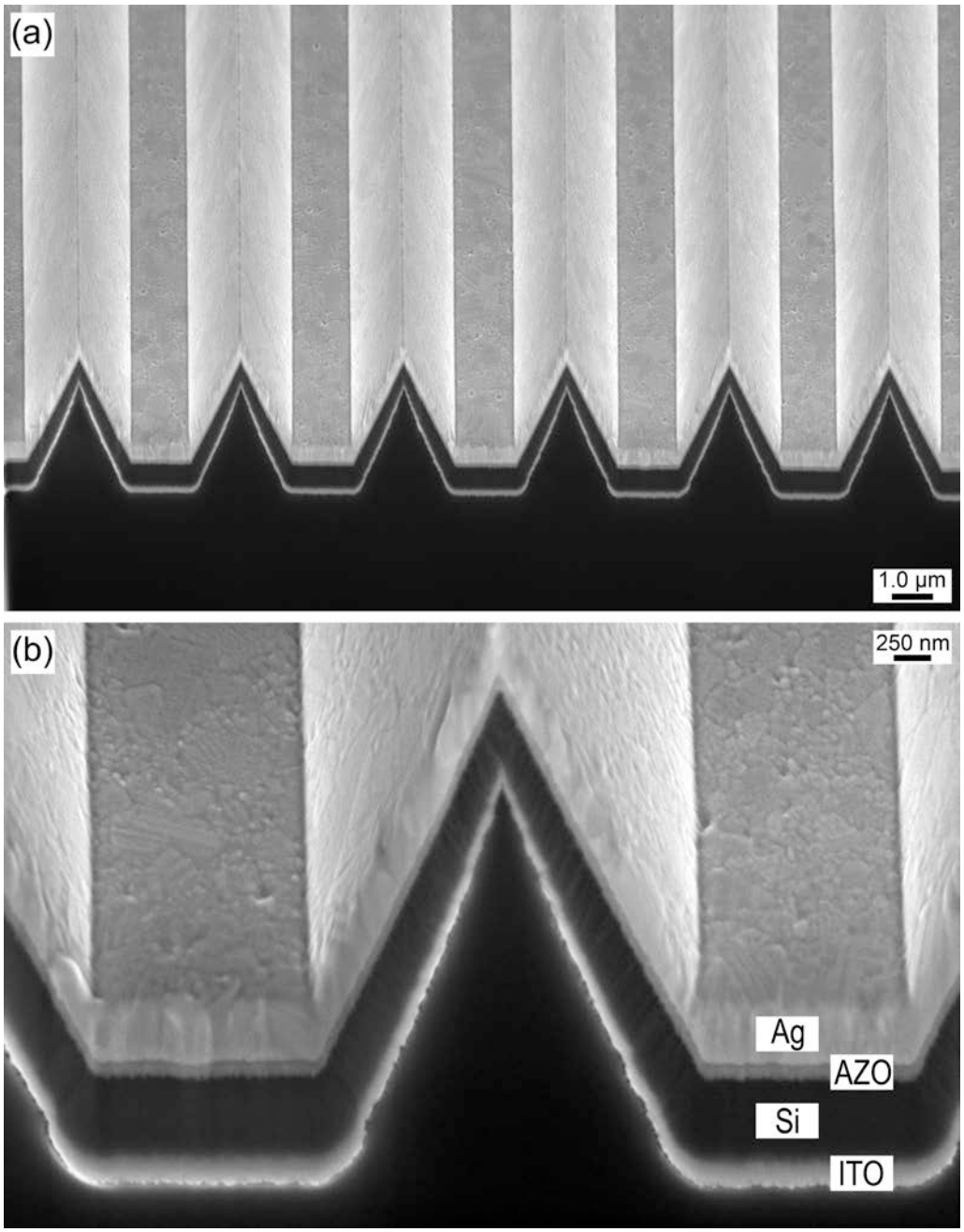

Figure 4.13 Scanning electron micrographs of a multilayered wedge structure made via template stripping. (a) A cross-section obtained by focused-ion-beam milling. (b) A close-up of the cross section showing the four layers of silver (Ag), aluminum-doped zinc oxide (AZO), silicon (Si), and indium tin oxide (ITO) (from top to bottom). These layers have thicknesses of ~250, ~65, ~350, and ~110 nm, respectively.

Moreover, patterned multilayer stacks can also be easily created, which can be useful for photovoltaics,[19-20] solar absorbers,[36] and metamaterials.[37-38] For example, figure 4.13 shows a wedge structure that contains four layers: Ag, aluminum-doped zinc oxide (AZO), Si, and ITO. As shown in the close-up image (figure 4.13b), each layer is continuous and even the bottom layer of ITO still maintains a sharp tip in the wedge. Although the demonstrated structure has a relatively large periodicity of 4 μm compared to previously reported structures,[19-20] we have also used template stripping to prepare smaller periodicities. Si templates can be patterned via electron-beam lithography, nanosphere lithography, or FIB milling. While the creation of nanometer-scale patterns with electron-beam lithography or FIB milling over large areas can be slow and costly, template stripping allows this template to be reused many times (>30 times with the upper limit not yet determined), potentially leading to low-cost, high-throughput, and large-scale nanofabrication.

4.3 Conclusions

In conclusion, we have demonstrated that template stripping can provide a general route to various patterned materials beyond the coinage metals. Namely, template stripping can create patterned refractory metals, semiconductors, and oxides. The advantages of template stripping, which were previously demonstrated for Ag, Au, and Cu, are maintained: (i) the surfaces of the resulting films can be smooth without contamination, (ii) a variety of structures can be patterned with nanometer-scale fidelity, and (iii) integrated multilayer architectures can be created. This extends template stripping to high-melting-point solids, such as W, and transparent conductors, such as ITO, both of which are difficult to pattern with conventional methods. Because such materials are becoming increasingly important for applications in photovoltaics, thermophotovoltaics, batteries, *etc.*, template stripping offers a simple approach to many optoelectronic, plasmonic, photonic, and electrochemical devices.

4.4 Experimental Section

Preparation of silicon templates

Silicon (100) wafers were used as templates due to their flatness, low cost, and easy processability for patterning and stripping.[11] Several different silicon templates were used in this work.

The templates for the bull's-eye structures were fabricated using photolithographic techniques. Specifically, positive photoresist (Shipley, Microposit S1805) was spin-coated onto pre-cleaned silicon substrates and then exposed under an ultraviolet (UV) lamp through a chrome-on-glass mask with a mask aligner (Karl Suss, MA6). The photoresist on the exposed areas was removed in developing solution (Shipley, Microposit 351 developer). The patterns of the photoresist layer were transferred to the underlying silicon substrates by reactive-ion etching (RIE). The RIE process was performed with CF_4 and O_2 gases, and the depth of the etched parts was controlled by varying the processing time.

To obtain the templates with micrometer-scale pyramid structures (micropyramids), silicon (100) wafers were coated with a 40-nm-thick chromium layer and then hole arrays were patterned on the chromium layer via photolithographic techniques. The hole arrays act as windows for anisotropic etching of the silicon. Since the (100) planes of the silicon are etched much faster in potassium hydroxide (KOH) solution than the (111) planes, the etching process proceeds until four symmetric (111) planes are exposed. As a result, silicon templates with the four faces of the pyramidal etch pits can be obtained.[11, 13] After the anisotropic etching process, the chromium layer was etched away with a chromium etchant (Cyantek, CR-7).

The templates for the wedge structures were prepared via a similar procedure as that used for the micropyramids. However, instead of hole arrays, gratings were patterned on the chromium layer.

Nanosphere lithography[13] was used to fabricate the templates with submicrometer-scale pyramid structures (nanopyramids). An aqueous solution containing

monodisperse 550-nm-diameter polystyrene spheres (Microparticles GmbH, 10 wt.%) was spin-coated onto silicon substrates (800 rpm for 2 min, followed by 1500 rpm for 30 sec) to construct a close-packed monolayer. After argon/oxygen plasma treatment to reduce the size of the spheres, the substrates were deposited with a thin chromium layer (~40 nm) via evaporation. Removing the polystyrene spheres can provide hexagonal hole arrays on the chromium layer, which are then used as a mask for KOH anisotropic etching.

All prepared templates were cleaned with piranha solution before deposition.

Deposition of release layer and desired materials

A thin gold film was introduced as a release layer between the silicon templates and the desired materials (refractory metals, semiconductors, and oxides). A 20-nm-thick gold layer was deposited on the patterned templates via evaporation or sputtering. Then, desired materials were added onto the gold layer. Tungsten and tantalum were deposited with DC magnetron sputtering at a power of 250 W. Silicon and indium tin oxide (ITO) were deposited with RF magnetron sputtering at a power of 180 and 35 W, respectively. The diameter of all sputtering targets was 2 inches. The pressure in the sputtering chamber was maintained at 6 mTorr with argon during deposition and the source-to-substrate distance was fixed as 14 cm. The sputtering time for each material was controlled to obtain ca. 200-nm-thick layers. For cadmium sulfide (CdS), chemical bath deposition method was used.[27] The CdS layers were grown in an aqueous solution containing 2 mM of cadmium chloride, 10 mM of thiourea, and 40 mM of ammonium chloride at 85 °C. The pH of the solution was adjusted to 9.5 by adding ammonium hydroxide. After 30 min of reaction, about 130-nm-thick CdS films were formed on the substrates.

Template stripping of the deposited films and removal of the release layer

To strip off the deposited films, UV-curable epoxy (Norland Products, NOA 61) was applied to the top surface of the films.[11] The epoxy layer was cured by exposing to a

UV lamp for 3 h. The cured epoxy was then employed as a backing layer for the deposited films. After curing, the deposited films were peeled off the silicon templates by using a razor blade. The gold layer on the top of the stripped films was removed with a gold etchant containing potassium iodide and iodine (Transene, GE-6). In most cases the etchant was very effective at selectively etching away the gold layer without damaging the underlying desired material (such as tungsten, tantalum, silicon, and ITO). However, CdS was attacked by the gold etchant. Thus, a different etchant was employed in this case. Using an aqueous solution containing 1 M KOH and 0.1 M potassium cyanide with oxygen purging, the gold layer could be selectively etched off without damaging the CdS films.[28]

Fabrication of bull's-eye structures via direct etching

Figure 4.6 and 4.7 compare tungsten bull's-eye structures prepared by conventional etching (figure 4.6c and 4.6d) with those obtained with template stripping (figure 4.6a and 4.6b). To fabricate the conventional bull's-eye structures, 500-nm-thick tungsten films were first deposited on flat silicon substrates by sputtering. Photoresist was coated on the tungsten films and then exposed under a UV lamp through a mask for bull's-eye patterns. The patterns of the photoresist were transferred into the underlying tungsten films by RIE. The RIE process was performed with SF_6 and Ar gases and the depth of the grooves was adjusted by the etching time.

Fabrication of multilayer structures via template stripping

Multilayer structures composed of metal, semiconductor, and oxide layers were also fabricated by the template-stripping method, as demonstrated in figure 4.13. Silicon templates for wedge structures were prepared via KOH anisotropic etching, as discussed above. Then 250 nm of silver, 65 nm of aluminum-doped zinc oxide, 350 nm of silicon, and 110 nm of ITO were sequentially deposited on the template by sputtering. Wedge structures containing these four layers were stripped with a cured-epoxy backing layer, revealing smooth silver surfaces. To observe the cross-sections of the multilayer

structures shown in figure 4.13, the structures were cut by focused-ion-beam milling with 30 kV as the acceleration voltage and 150 pA as the ion-beam current.

Characterization of surface morphology

An atomic force microscope (AFM, Agilent 5500) was utilized to characterize the surface morphology of the prepared structures. All AFM images were obtained by using tapping mode and the root mean square (RMS) roughness of the stripped surfaces was determined with $2.5 \times 2.5\ \mu m^2$ scans.

Characterization of impurities on template-stripped surfaces

The impurities on the template-stripped surfaces were characterized with X-ray photoelectron spectroscopy (XPS, PHI 5000 VersaProbe). The X-ray source was Al Kα (1486.6 eV) and 25 W (15 kV) was applied to the source. The photoelectrons were detected at an angle of 45° from normal under ultrahigh vacuum (base pressure of 6.7×10^{-8} Pa). The analyzer pass energy for a wide scan and a high-resolution scan was 117.40 and 23.50 eV, respectively.

Characterization of residual Au on template-stripped bull's-eye structures

After removing the Au release layers on the template-stripped bull's-eye structures by wet etching, the existence of residual Au was examined with energy dispersive X-ray spectroscopy (EDS, JEOL 6500 or Zeiss NVision 40). The X-ray detector was cooled by using liquid nitrogen. For tungsten and tantalum structures, the electron-beam acceleration voltage of 10 kV was utilized. For silicon, ITO, and CdS structures, the acceleration voltage was 5 kV.

Optical characterization of nanopyramid arrays

Optical characterization of the tungsten nanopyramid arrays was performed with a tungsten halogen lamp, liquid-nitrogen-cooled CCD photodetector (Princeton Instruments), and an inverted optical microscope (Nikon TE 200). A tungsten

nanopyramid film was illuminated by the lamp and the reflected light was collected using a high-numerical-aperture (NA) objective lens (100×, NA = 0.9). The reflected image of the nanopyramid arrays was then formed on the detector and analyzed spectroscopically. A flat single-crystalline silver film[30] with RMS surface roughness of ~1 nm was employed as a reference to obtain the absolute reflectivity of the sample, at each wavelength. The reflectivity of this silver reference sample was independently determined via ellipsometery. Absorptivity was estimated from 1–*R*, where *R* is the reflectivity. Thus, light scattered at high angles was neglected. A flat 350-nm-thick tungsten film with RMS surface roughness of ~1 nm was prepared by DC magnetron sputtering and the absorptivity was compared with the tungsten nanopyramid film.

4.5 References

[1] B. D. Gates, Q. Xu, M. Stewart, D. Ryan, C. G. Willson, G. M. Whitesides, "New Approaches to Nanofabrication: Molding, Printing, and Other Techniques," *Chem. Rev.* **2005,** *105*, 1171.

[2] N. C. Lindquist, P. Nagpal, K. M. McPeak, D. J. Norris, S.-H. Oh, "Engineering Metallic Nanostructures for Plasmonics and Nanophotonics," *Rep. Prog. Phys.* **2012,** *75*, 036501.

[3] C. Vieu, F. Carcenac, A. Pépin, Y. Chen, M. Mejias, A. Lebib, L. Manin-Ferlazzo, L. Couraud, H. Launois, "Electron Beam Lithography: Resolution Limits and Applications," *Appl. Surf. Sci.* **2000,** *164*, 111.

[4] J. Joo, B. Y. Chow, J. M. Jacobson, "Nanoscale Patterning on Insulating Substrates by Critical Energy Electron Beam Lithography," *Nano Lett.* **2006,** *6*, 2021.

[5] M. Park, C. Harrison, P. M. Chaikin, R. A. Register, D. H. Adamson, "Block Copolymer Lithography: Periodic Arrays of Similar to 10(11) Holes in 1 Square Centimeter," *Science* **1997,** *276*, 1401.

[6] S.-J. Jeong, G. Xia, B. H. Kim, D. O. Shin, S.-H. Kwon, S.-W. Kang, S. O. Kim, "Universal Block Copolymer Lithography for Metals, Semiconductors, Ceramics, and Polymers," *Adv. Mater.* **2008,** *20*, 1898.

[7] E. Kim, Y. N. Xia, G. M. Whitesides, "Polymer Microstructures Formed by Molding in Capillaries," *Nature* **1995,** *376*, 581.

[8] S. Y. Chou, P. R. Krauss, P. J. Renstrom, "Imprint Lithography with 25-Nanometer Resolution," *Science* **1996,** *272*, 85.

[9] A. Kumar, G. M. Whitesides, "Features of Gold Having Micrometer to Centimeter Dimensions Can Be Formed through a Combination of Stamping with an Elastomeric Stamp and an Alkanethiol Ink Followed by Chemical Etching," *Appl. Phys. Lett.* **1993,** *63*, 2002.

[10] M. Geissler, H. Schmid, A. Bietsch, B. Michel, E. Delamarche, "Defect-Tolerant and Directional Wet-Etch Systems for Using Monolayers as Resists," *Langmuir* **2002,** *18*, 2374.

[11] P. Nagpal, N. C. Lindquist, S.-H. Oh, D. J. Norris, "Ultrasmooth Patterned Metals for Plasmonics and Metamaterials," *Science* **2009,** *325*, 594.

[12] M. Hegner, P. Wagner, G. Semenza, "Ultralarge Atomically Flat Template-Stripped Au Surfaces for Scanning Probe Microscopy," *Surf. Sci.* **1993,** *291*, 39.

[13] C.-H. Sun, N. C. Linn, P. Jiang, "Templated Fabrication of Periodic Metallic Nanopyramid Arrays," *Chem. Mater.* **2007,** *19*, 4551.

[14] N. C. Lindquist, T. W. Johnson, D. J. Norris, S.-H. Oh, "Monolithic Integration of Continuously Tunable Plasmonic Nanostructures," *Nano Lett.* **2011,** *11*, 3526.

[15] J. H. Park, P. Nagpal, S.-H. Oh, D. J. Norris, "Improved Dielectric Functions in Metallic Films Obtained via Template Stripping," *Appl. Phys. Lett.* **2012,** *100*, 081105.

[16] H. Raether, *Surface Plasmons on Smooth and Rough Surfaces and on Gratings*. Springer-Verlag: Berlin, 1988.

[17] N. C. Lindquist, P. Nagpal, A. Lesuffleur, D. J. Norris, S.-H. Oh, "Three-Dimensional Plasmonic Nanofocusing," *Nano Lett.* **2010,** *10*, 1369.

[18] H. A. Atwater, A. Polman, "Plasmonics for Improved Photovoltaic Devices," *Nat. Mater.* **2010,** *9*, 205.

[19] V. E. Ferry, M. A. Verschuuren, H. B. T. Li, E. Verhagen, R. J. Walters, R. E. I. Schropp, H. A. Atwater, A. Polman, "Light Trapping in Ultrathin Plasmonic Solar Cells," *Opt. Express* **2010,** *18*, A237.

[20] J. Zhu, C.-M. Hsu, Z. F. Yu, S. H. Fan, Y. Cui, "Nanodome Solar Cells with Efficient Light Management and Self-Cleaning," *Nano Lett.* **2010,** *10*, 1979.

[21] T. Bauer, *Thermophotovoltaics: Basic Principles and Critical Aspects of System Design*. Springer-Verlag: Berlin, 2011.

[22] A. Heinzel, V. Boerner, A. Gombert, B. Bläsi, V. Wittwer, J. Luther, "Radiation Filters and Emitters for the NIR Based on Periodically Structured Metal Surfaces," *J. Mod. Optic.* **2000,** *47*, 2399.

[23] S. Y. Lin, J. Moreno, J. G. Fleming, "Three-Dimensional Photonic-Crystal Emitter for Thermal Photovoltaic Power Generation," *Appl. Phys. Lett.* **2003,** *83*, 380.

[24] P. Nagpal, S. E. Han, A. Stein, D. J. Norris, "Efficient Low-Temperature Thermophotovoltaic Emitters from Metallic Photonic Crystals," *Nano Lett.* **2008,** *8*, 3238.

[25] X. Liu, T. Tyler, T. Starr, A. F. Starr, N. M. Jokerst, W. J. Padilla, "Taming the Blackbody with Infrared Metamaterials as Selective Thermal Emitters," *Phys. Rev. Lett.* **2011,** *107*, 045901.

[26] R. Ortega-Borges, D. Lincot, "Mechanism of Chemical Bath Deposition of Cadmium Sulfide Thin Films in the Ammonia-Thiourea System: In-Situ Kinetic Study and Modelization," *J. Electrochem. Soc.* **1993,** *140*, 3464.

[27] N. G. Dhere, D. L. Waterhouse, K. B. Sundaram, O. Melendez, N. R. Parikh, B. Patnaik, "Studies on Chemical Bath Deposited Cadmium Sulfide Films by Buffer Solution Technique," *J. Mater. Sci. Mater. Electron.* **1995,** *6*, 52.

[28] A. Kumar, H. A. Biebuyck, N. L. Abbott, G. M. Whitesides, "The Use of Self-Assembled Monolayers and a Selective Etch to Generate Patterned Gold Features," *J. Am. Chem. Soc.* **1992,** *114*, 9188.

[29] C. A. Volkert, A. M. Minor, "Focused Ion Beam Microscopy and Micromachining," *MRS Bull.* **2007,** *32*, 389.

[30] J. H. Park, P. Ambwani, M. Manno, N. C. Lindquist, P. Nagpal, S.-H. Oh, C. Leighton, D. J. Norris, "Single-Crystalline Silver Films for Plasmonics," *Adv. Mater.* **2012,** *24*, 3988.

[31] S. E. Han, D. J. Norris, "Beaming Thermal Emission from Hot Metallic Bull's Eyes," *Opt. Express* **2010,** *18*, 4829.

[32] N. E. Sosa, J. Liu, C. Chen, T. J. Marks, M. C. Hersam, "Nanoscale Writing of Transparent Conducting Oxide Features with a Focused Ion Beam," *Adv. Mater.* **2009,** *21*, 721.

[33] E. Rephaeli, S. Fan, "Tungsten Black Absorber for Solar Light with Wide Angular Operation Range," *Appl. Phys. Lett.* **2008,** *92*, 211107.

[34] S. A. Campbell, *The Science and Engineering of Microelectronic Fabrication*. Oxford University Press: New York, 2001.

[35] P. R. West, S. Ishii, G. V. Naik, N. K. Emani, V. M. Shalaev, A. Boltasseva, "Searching for Better Plasmonic Materials," *Laser Photonics Rev.* **2010,** *4*, 795.

[36] N. P. Sergeant, M. Agrawal, P. Peumans, "High Performance Solar-Selective Absorbers Using Coated Sub-Wavelength Gratings," *Opt. Express* **2010,** *18*, 5525.

[37] D. R. Smith, J. B. Pendry, M. C. K. Wiltshire, "Metamaterials and Negative Refractive Index," *Science* **2004,** *305*, 788.

[38] J. Valentine, S. Zhang, T. Zentgraf, E. Ulin-Avila, D. A. Genov, G. Bartal, X. Zhang, "Three-Dimensional Optical Metamaterial with a Negative Refractive Index," *Nature* **2008,** *455*, 376.

Chapter 5.
Tailored Thermal Emission from Metallic Bull's Eye Structures*

Optical sources generating directional monochromatic beams are of critical importance in a variety of applications. Here, we demonstrate that periodic metal structures can provide such a source via a simple thermal process. Theoretical calculation has shown that the thermal excitation of surface plasmon polaritons on a metallic bull's-eye structure (a series of circular concentric grooves) can lead to tailored thermal emission. To verify the predicted results, a bull's-eye structure of tungsten was fabricated by photolithography and metal-sputtering deposition. When the bull's eye was heated to 900 ºC, the emission spectrum for the normal direction showed a single peak at 3.532 μm, comparable to the period of the structure. The full-width-at-half-maximum and angular divergence of the emission peak was only 30 nm and 1.4º, respectively. In addition, the peak disappeared rapidly at tilted emission angles. In other words, the bull's eye can provide a unidirectional monochromatic beam. Moreover, the thermal stability of the structure at high temperatures could be improved by coating with a hafnium oxide layer on the metal surfaces via atomic layer deposition. Even after heating at 900 ºC for 24 hr, the morphology of the hafnium oxide-coated structure was hardly changed. Consequently, the bull's eye can be utilized for many practical applications including a novel radiation source generating a unidirectional monochromatic beam.

* The main portion of this chapter has been prepared for submission as Jong Hyuk Park, Sang Eon Han, Prashant Nagpal, and David J. Norris, "Tailored Thermal Emission from Metallic Bull's Eye Structures."

5.1 Introduction

Surface plasmon polaritons (SPPs) are electromagnetic waves that propagate along a metal surface.[1] Since SPPs have the hybrid nature of photons and electrons, manipulating SPPs allows concentration of light below the optical diffraction limit, inducing large electric-field enhancements. Due to this unique property, SPPs have been exploited for a variety of applications such as subwavelength waveguides, molecular sensors, high-resolution microscopy, and solar cells.[2-5] In general, SPPs are generated by using an optical source, that is light illumination.[6-7] However, to provide additional flexibility for plasmonic devices, it will be desirable to develop non-optical sources for SPPs. Thermal excitation can be a promising route to create SPPs.[8] Since many plasmonic devices are at the micro- or nanometer scale and have a low heat capacity, even low power supplied by laser illumination or electrical heating can thermally excite SPPs over the entire device or on a selected area of it.

Moreover, the thermal excitation of SPPs can lead to tailored thermal emission to control both emission angle and wavelength simultaneously. The thermally excited SPPs on patterned metal structures can be coupled to light through the following procedure. Thermal energy generates SPPs on metal structures and the SPPs propagate along the metal surfaces. During the propagation, the SPPs gain additional momentum from the patterns on the surfaces, which allows coupling to light and leads to thermal emission from the structures. Due to momentum conservation, the emission angle and wavelength of the light are determined by the additional momentum.[9] Furthermore, this additional momentum can be adjusted by the geometry of the patterned metal structure. Therefore, heating properly-designed metal structures can result in tailored thermal emission.

This strategy for modifying the thermal emission spectrum of materials via coupling of surface waves to light in patterned structures has previously been reported.[9-18] The surface waves can be either SPPs for metallic materials or surface phonon polaritons for polar materials. However, the surface waves on the supporting materials can be launched only in the wavelength range where the real part of its dielectric function

is smaller than -1.[18] Accordingly, surface phonon polaritons have been utilized at relatively long wavelengths, for example, about 11.5 μm for silicon carbide[9, 11] and 9 μm for silicon dioxide.[12-13] In contrast, SPPs on metallic materials can be applicable in a broad wavelength range including visible wavelengths. Thus, exploiting SPPs allows flexibility in choosing the target wavelength for the modification of the thermal emission.

While unstructured materials typically exhibit broadband thermal emission spectra, prior research has pursued the use of patterned interfaces to obtain sharp emission peaks. Indeed, such a thermal emission spectrum was obtained by using metal films with simple one-dimensional (1D) periodic gratings.[14-15] However, since the peak wavelength of the emission varies with the emission angle, the 1D grating structures generate a series of monochromatic beams with different emission angles. Therefore, the tailored thermal emission with a unidirectional monochromatic beam was not obtained with this approach.

A bull's-eye structure, that is a series of circular concentric grooves, [7, 17, 19] can provide a promising solution to address this possibility. In a bull's-eye structure, SPPs can efficiently couple to light only when propagating along paths that pass through the center. Thus, during coupling, the SPPs gain constant momentum from a bull's-eye structure. In this case, the emission angle and wavelength of the coupled light are related to each other. If one is changed, the other should also vary. As shown in our previous publication,[17] when the wavelength of the light is close to the period of the bull's eye, an emission peak occurs in the normal direction. Even though light with longer or shorter wavelengths than the period is also emitted at different angles, its contribution to the overall emission is negligible because such emission features need to be averaged around the circumference of the structure. Consequently, the thermal emission from a bull's-eye structure should be strong at the wavelength of the period of the structure in the normal direction and will be weaker at all other wavelengths and directions.

Here, we experimentally demonstrate tailored thermal emission from metallic bull's eyes. When the bull's eyes are heated to 900 ºC, a unidirectional and monochromatic beam can be obtained. The emission spectrum in the normal direction

shows a single peak at 3.532 μm, which is nearly identical to the period of the bull's eye. The full-width-at-half-maximum (FWHM) and angular divergence of the emission peak was only 30 nm and 1.4º, respectively. These experimental results are highly consistent with numerical simulations. Furthermore, the thermal stability of the structures can be improved by adding a protective oxide layer on the metal surfaces. Consequently, a simple thermal process, that is heating of a metallic bull's eye, can provide a novel source of infrared radiation.

5.2 Results and Discussion

Tungsten and molybdenum were chosen as the materials for the bull's eyes because both have a high melting point over 2500 ºC and can support SPPs in the infrared wavelength range. Moreover, since they are abundant and inexpensive materials, they could be employed in practical applications. Considering the dielectric function of the materials and the facile fabrication of the structure, the target wavelength for the modification of the thermal emission spectrum was chosen to be about 3.5 μm. Based on this wavelength, the geometry of the bull's eye was designed by numerical simulation to obtain a unidirectional monochromatic beam with large emissivity.[17] Tungsten and molybdenum bull's eyes were fabricated by the following procedure. 300 circular concentric grooves with a period of 3.52±0.01 μm were patterned on silicon substrates via photolithography and reactive-ion etching (RIE). Then, a 160-nm-thick tungsten or molybdenum layer was deposited on the patterned substrates by dc magnetron sputtering. The fill factor of the bull's eye, defined as the ratio of the length of the ridge to the period, was adjusted to about 0.5 by tuning the process parameters of the photolithography. The depth of the grooves was controlled to be 180 nm by varying the duration time of the RIE.

Figure 5.1 shows scanning electron microscopy (SEM) images of a tungsten bull's eye. The diameter of the entire bull's eye was about 2.1 mm and no defect was found over the entire patterned area. Moreover, the structure had smooth surfaces as shown in figure 5.1b. The surface morphology of the bull's eyes was characterized with

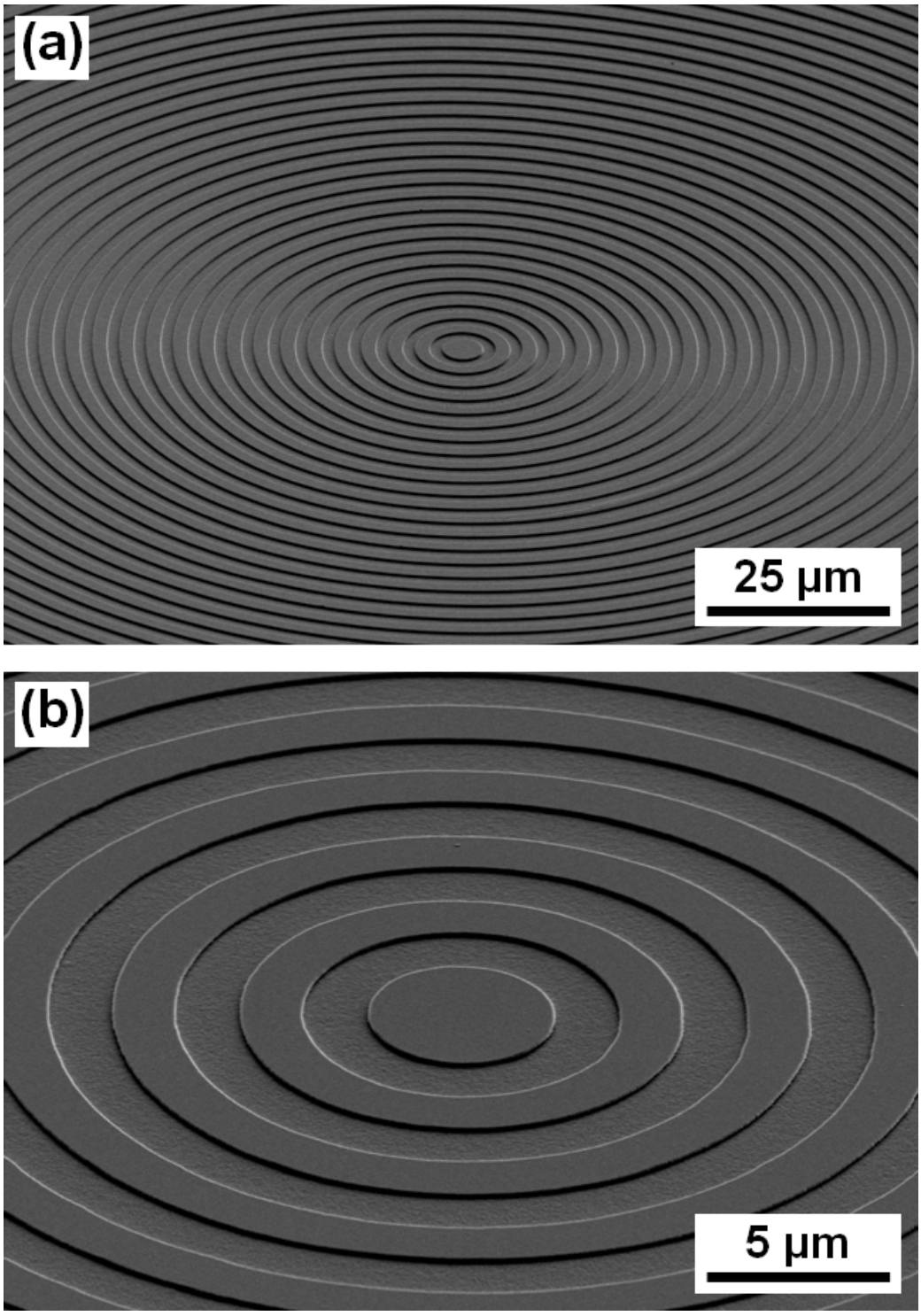

Figure 5.1 Scanning electron micrographs of a tungsten bull's eye. The structure contains 300 circular concentric grooves that are 180 nm deep and 1.76 μm wide. The period of the structure is 3.52 μm. The images were taken with the sample tilted 60° from normal.

atomic force microscopy (AFM). To avoid the inaccurate measurement due to the large height difference between the ridges and grooves, the flat areas outside of the bull's-eye patterns were scanned. Figure 5.2 shows the AFM images of the tungsten and molybdenum films. Both films exhibit very smooth surfaces with a root mean square (RMS) roughness below 1.5 nm, and presumably, these roughness values are equivalent to those in the patterned areas. Since the smooth surfaces can play a significant role in reducing the ohmic loss and unwanted scattering of SPPs,[20-21] such bull's eyes will manipulate SPPs more efficiently compared to the rough structures prepared via direct RIE of tungsten films.[22] Consequently, these smooth bull's eyes are expected to show improved thermal emission properties.

For the measurement of the thermal emission spectrum, a setup for precisely aligned experiments is required. Figure 5.3 describes the apparatus which includes a Fourier-transform infrared (FT-IR) spectrometer, mirrors, pinholes, a heating chamber, a goniometer, and a translation stage. Such components could be aligned by using a laser

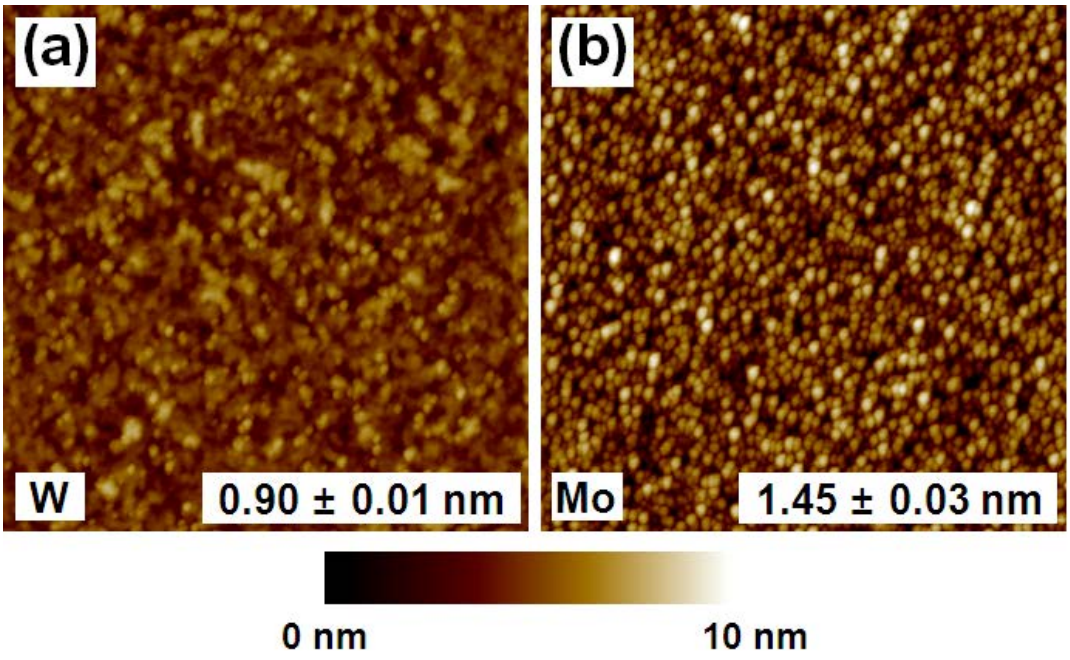

Figure 5.2 Surface morphology of metal films deposited on silicon substrates. (a) Tungsten (W) and (b) molybdenum (Mo) films. Each image includes the extracted RMS roughness from the 2.5 × 2.5 μm^2 scanned area.

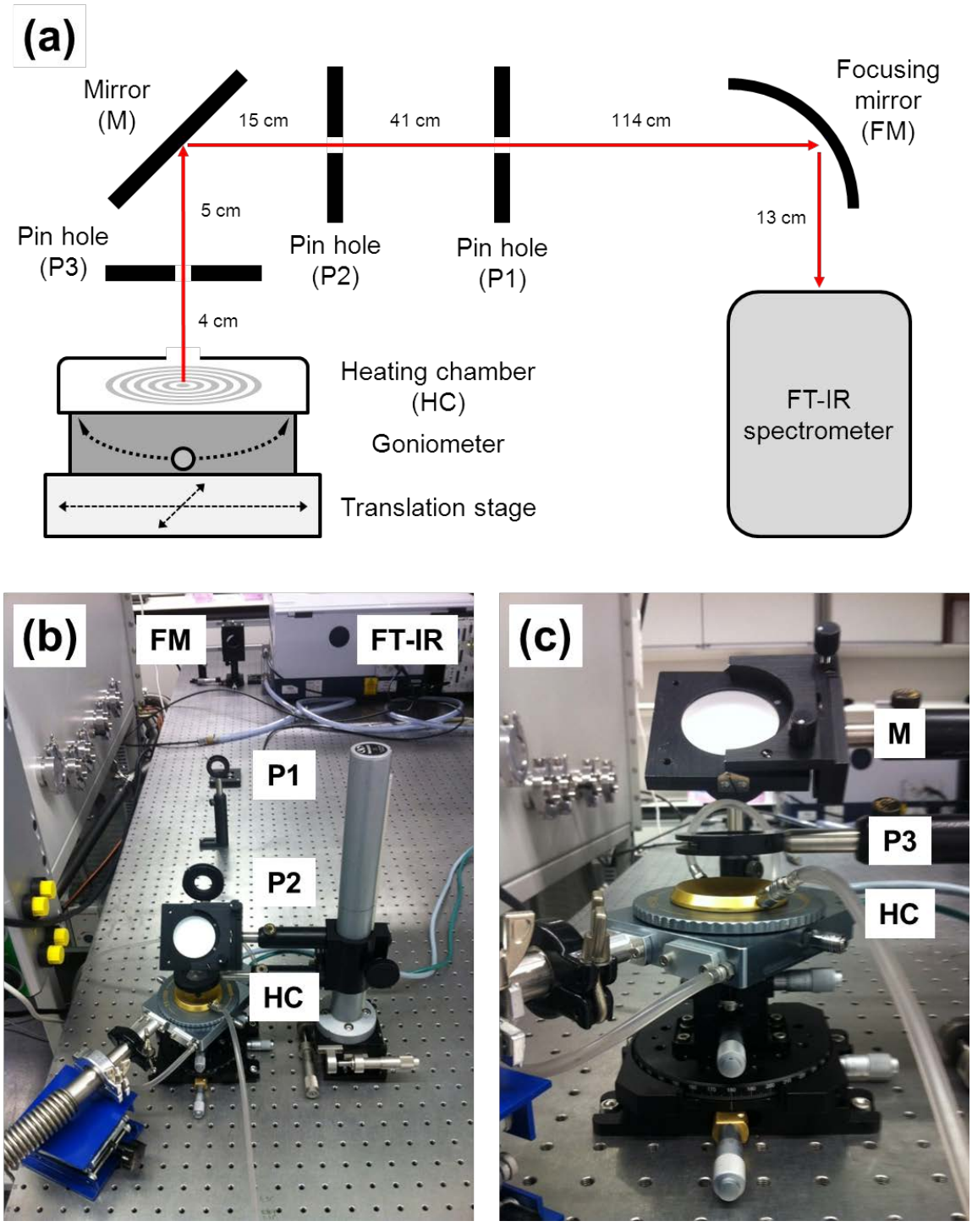

Figure 5.3 (a) Schematic of the experimental setup for measuring thermal emission spectra from bull's eyes. The distance between individual components is represented. (b) and (c) Photographs of the actual experimental setup. The heating chamber is connected to a turbomolecular pump for evacuation and the outside of the chamber is cooled to room temperature by water circulation.

beam coming from the FT-IR spectrometer. The sample was set on the center of the resistive heater in the heating chamber where the laser beam hits. The position and tilt angle of the sample could be finely adjusted by using the reflected laser beam from the sample. To minimize the heat loss and temperature variation at elevated temperatures, the air in the chamber was evacuated thoroughly and then, the sample was heated to 900 ºC. The size of the pinholes in the beam path was controlled to obtain a collection angle of ±0.1º.

Figure 5.4 shows the thermal emission spectra of the tungsten bull's eye at 900 ºC. The emission spectra were measured at various tilt angles (θ) from normal (figure 5.4a). To calibrate the emissivity, each emission spectrum was normalized by that of a carbon emitter (pelletized carbon nanopowder), which was assumed to be a blackbody. As predicted by theoretical calculations in a previous work,[17] the bull's eye shows a single sharp emission peak in the normal direction. The peak is observed at 3.532 μm, nearly identical to the period of the structure (3.52±0.01 μm), and its FWHM (Δλ) is 30 nm, giving a quality factor ($Q = \lambda / \Delta\lambda$) of 118. Moreover, if the sample is tilted, the peak is split and the emissivity decreases rapidly. This implies that the bull's eye provides a unidirectional monochromatic beam, as compared to the 1D grating structure that has multiple emission peaks at different emission angles.[14] Since the bull's eye can couple SPPs to only p-polarized light, the maximum emissivity of the structure is slightly higher than 0.5. As shown in figure 5.4a, the emissivity of the peak for the normal angle (0.545) is close to the maximum value. Hence, we confirmed that the bull's eye has desirable properties for coupling SPPs to light efficiently.

The calculated emission spectra of the bull's eye at various tilt angles were obtained via numerical simulation (figure 5.4b). For the simulation, we assumed that the size of the bull's eye is much larger than the coherence length of the SPPs, that is the propagation distance over which the SPPs maintain a specified degree of coherence (usually the intensity of SPPs becomes 1/e). Therefore, the effect of the center and the boundary of the structure on the thermal emission can be neglected and the bull's eye can be regarded as a series of linear gratings oriented around the center.[17] To determine the

optical properties of the structure, we obtained the averaged absorptivity of linear gratings evenly distributed in all directions. Since the absorptivity is equivalent to the emissivity according to Kirchhoff's law,[23-24] the calculated absorptivity can be used to estimate the emissivity of the structure. The simulation was performed with the

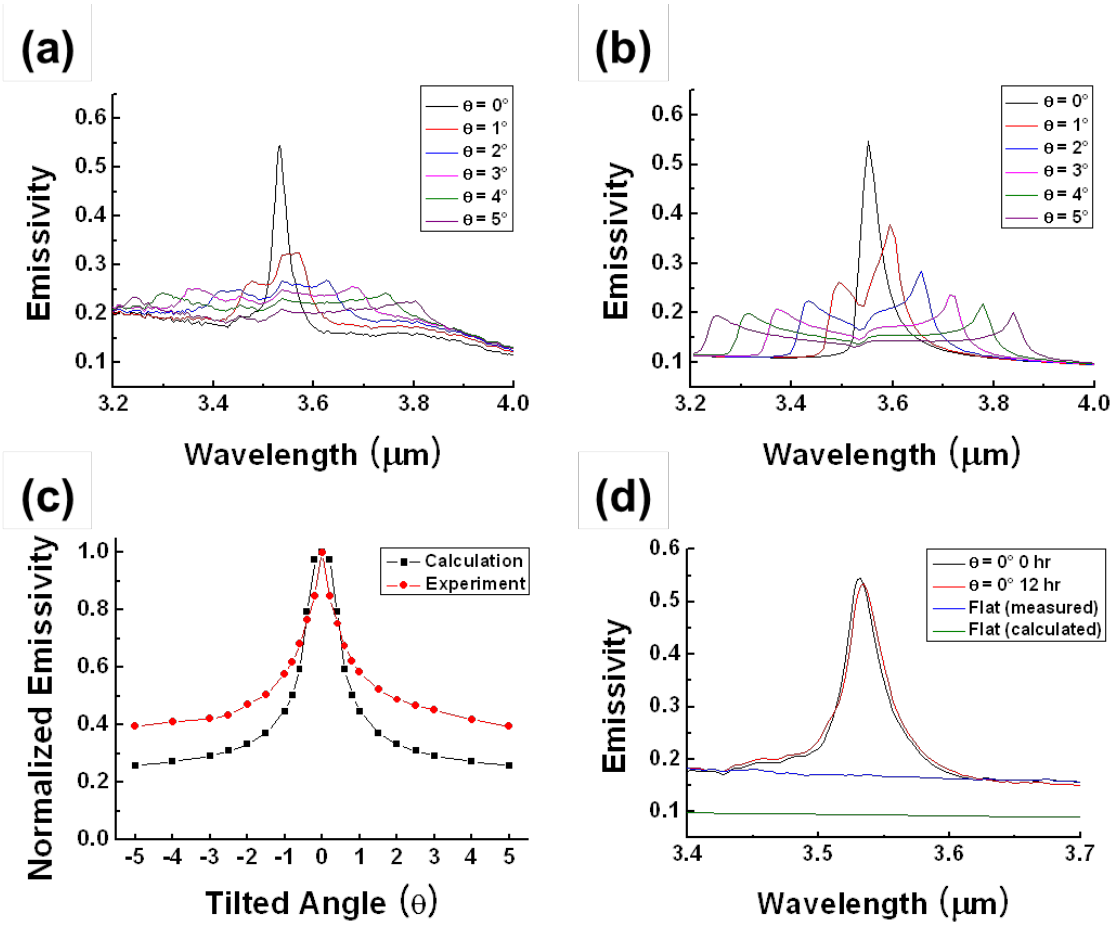

Figure 5.4 Thermal emission spectra of a tungsten bull's eye at 900 ºC. The dimensional parameters of the structure are: a fill factor of 0.5, a groove depth of 180 nm, and a period of 3.52 μm. (a) Measured thermal emission spectra at various tilt angles (θ) from normal. The collection angle of the emission spectrum is ±0.1° and a carbon emitter is utilized as a reference to calibrate the emissivity. (b) Calculated thermal emission spectra at various tilt angles (θ) from normal. The dielectric function of tungsten for 900 ºC is employed. (c) Angular dependence of the emissivity at the peak maximum. The measured and calculated spectra for the normal angle (θ = 0) show the maximum emissivity of 0.545 at 3.532 μm and 0.547 at 3.552 μm, respectively. The emissivity at the given wavelength for different θ is normalized with the maximum emissivity for the normal angle. (d) Comparison of the emission spectra initially and after 12 hr at 900 ºC. The measured and calculated emission spectra for a flat tungsten film at 900 ºC are also shown.

dimensional parameters of the structure listed in figure 5.1 and the dielectric function of tungsten for 900 ºC.[25] The calculated emission results are highly consistent with the experimental ones. The emission spectrum for the normal angle shows a single emission peak at 3.552 μm with a FWHM of 40 nm. When the sample is tilted, the split of the emission peak and the decrease in the emissivity are observed in the same manner as the measured emission spectra.

Figure 5.4c indicates the angular dependence of the emissivity at the peak maximum. The measured and calculated spectrum for the normal angle shows a maximum emissivity of 0.545 at 3.532 μm and 0.547 at 3.552 μm, respectively. At the given wavelength, the emissivity for tilt angles is normalized with the maximum emissivity for the normal angle. The angular divergence ($\Delta\theta$) of the emission peak for the measured and calculated emission spectrum is estimated as 1.4 and 1.2º, corresponding to the SPP coherence length ($L_{SPP} = \lambda / \Delta\theta$) of 145 and 170 μm, respectively. Since the size of the bull's-eye structure (2.1 mm) is much larger than these coherence lengths, our assumption for the simulation is justified.

Figure 5.4d contains the emission spectra of the bull's eye initially and after 12 hr at 900 ºC. After heating for 12 hr, the emission peak had a FWHM of 35 nm and shifted to 3.535 μm. In other words, a peak broadening and peak shift were observed after prolonged heating. This change resulted from a deterioration of the tungsten structure at high temperatures. The surface morphology of the bull's eye before and after heating will be compared in the next paragraph. Figure 5.4d also includes the emission spectra for a flat tungsten film at 900 ºC. Our flat tungsten film shows larger emissivity than that calculated from literature values of the dielectric function.[25] It is known that metal films of the same element can exhibit different optical properties due to surface roughness and grain boundaries.[21, 26] Consequently, we believe that the difference in thermal emission properties between the experimental and calculated results was partly caused by the different optical properties of materials. In addition, since the emissivity of the experimental results was calibrated with the spectrum of a carbon emitter, which was assumed to be a blackbody, the emissivity values may contain experimental errors (for

example, variations in temperature or emission angle between two measurements) as well as the effect of the assumption.

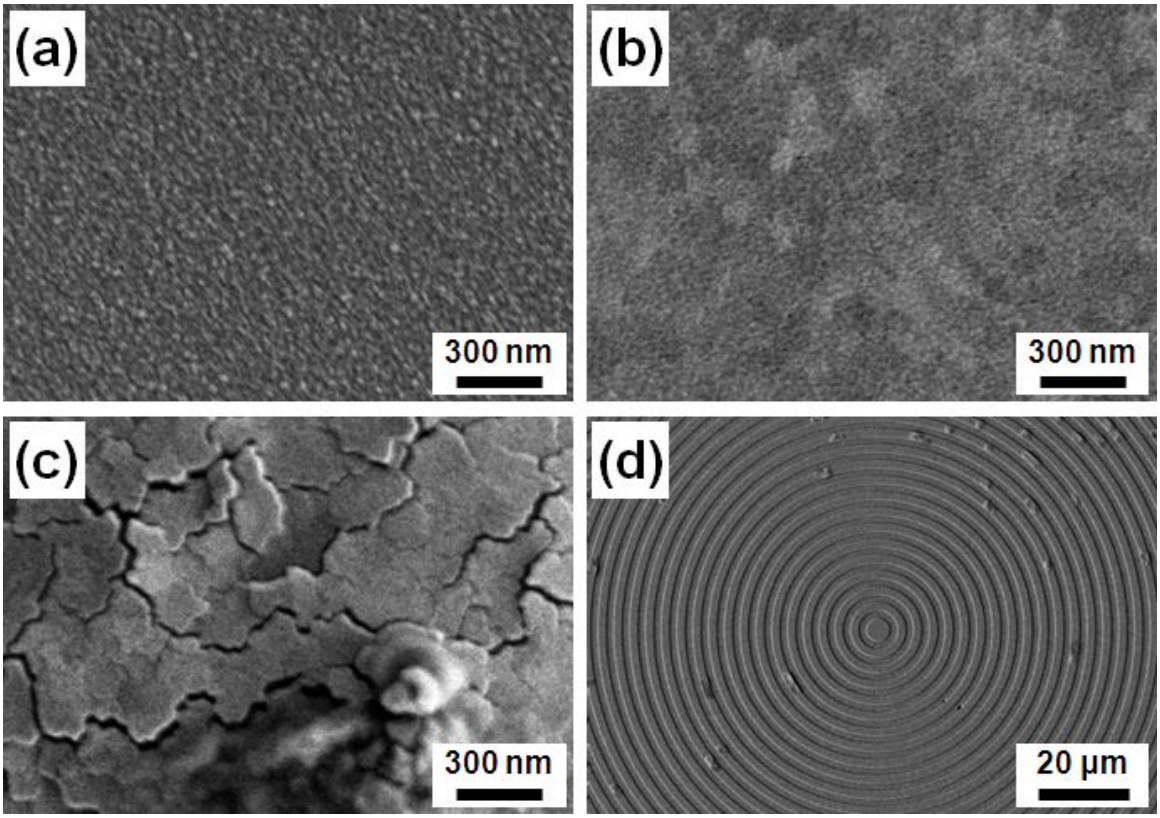

Figure 5.5 Scanning electron micrographs of a tungsten bull's eye before and after heating. The surface of a ridge in the bull's eye (a) before heating and (b) after heating at 900 ºC for 12 hr. Morphology of (c) a cracked region and (d) a bull's-eye pattern after heating at 900 ºC for 12 hr. The structure maintains bull's-eye patterns but many cracked regions are observed over the entire structure.

Figure 5.5a and 5.5b show the surface of a ridge in the tungsten bull's eye before and after heating, respectively. While the initial size of the tungsten grains was around 20 nm, which is consistent with the AFM image (figure 5.2a), after heating at 900 ºC for 12 hr, the grain size increased to around 100 nm. The grain growth of tungsten at high temperatures needs to be suppressed because it can result in roughening the surfaces and collapsing the structure at the end. For free-standing structures, this problem has been avoided by alloy formation with molybdenum.[27] However, since our structure lies on a silicon substrate, another issue that should be considered is the difference in thermal

expansion between a tungsten layer and a silicon substrate. In fact, the stress due to the thermal expansion difference at elevated temperatures can cause cracks on the tungsten layer of the bull's eye (figure 5.5c and 5.5d). Moreover, if the temperature is high enough, even small amounts of oxygen that remain in the heating chamber can oxidize the metal surfaces, leading to the deterioration of the thermal emission properties. We observed the oxidation of metal structures by the heating process especially for molybdenum. When a molybdenum bull's-eye structure was heated to 600 ºC, the surface morphology changed significantly (figure 5.6) and the material exhibited yellow color indicating oxidized molybdenum.[28-29] Since the oxidation of molybdenum occurs not only at the surfaces but also throughout the entire structure due to the volatility of molybdenum oxide at high temperatures,[28] SPPs cannot be excited and tailored thermal emission cannot be obtained.

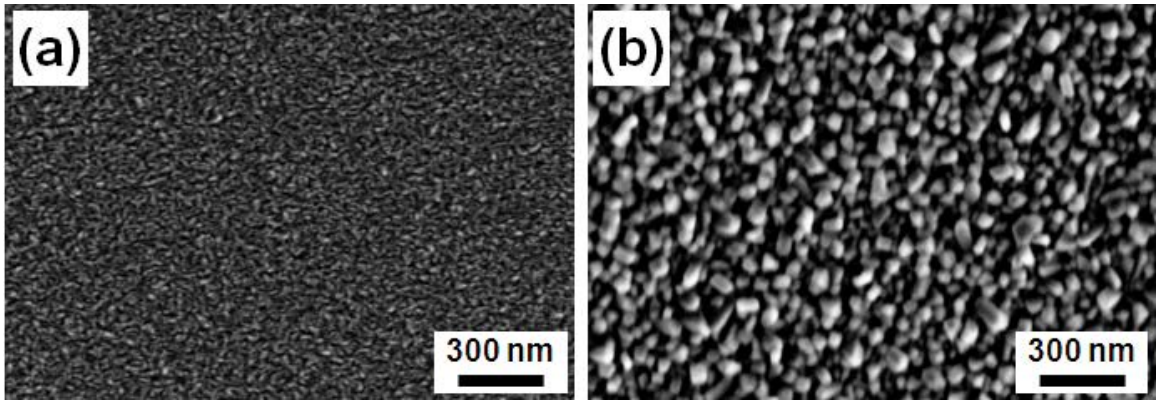

Figure 5.6 Scanning electron micrographs of a molybdenum bull's eye before and after heating. The surface of a ridge in the bull's eye (a) before heating and (b) after heating at 600 ºC for 2 hr. The surface morphology is changed significantly after heating.

To address these issues and guarantee the thermal stability of the bull's eye for extended periods, we introduced a protective oxide layer on the metal surface. Considering optical properties and thermal stability, hafnium oxide (HfO_2) was chosen as the material for this protective layer. Atomic layer deposition (ALD) was utilized because it can provide a uniform and continuous HfO_2 layer with an accurately controlled thickness.[30-31] An 11-nm-thick HfO_2 layer was deposited on the metal surface and then, the thermal stability of the bull's eye was tested. Figure 5.7 shows SEM images of the

HfO_2-coated bull's eyes after heating. Surprisingly, even after 24 hr at 900 ºC, both surfaces of the tungsten and molybdenum structures have the same morphology as the initial state and the individual grain size seems hardly changed (figure 5.7a and 5.7b). This indicates the HfO_2 layer can effectively suppress the grain growth of the materials and prevent the diffusion and oxidation of metals on the surface by the heating process. As a result, the HfO_2-coated bull's eyes could maintain their morphology without deforming when at high temperatures for extended periods (figure 5.7c and 5.7d).

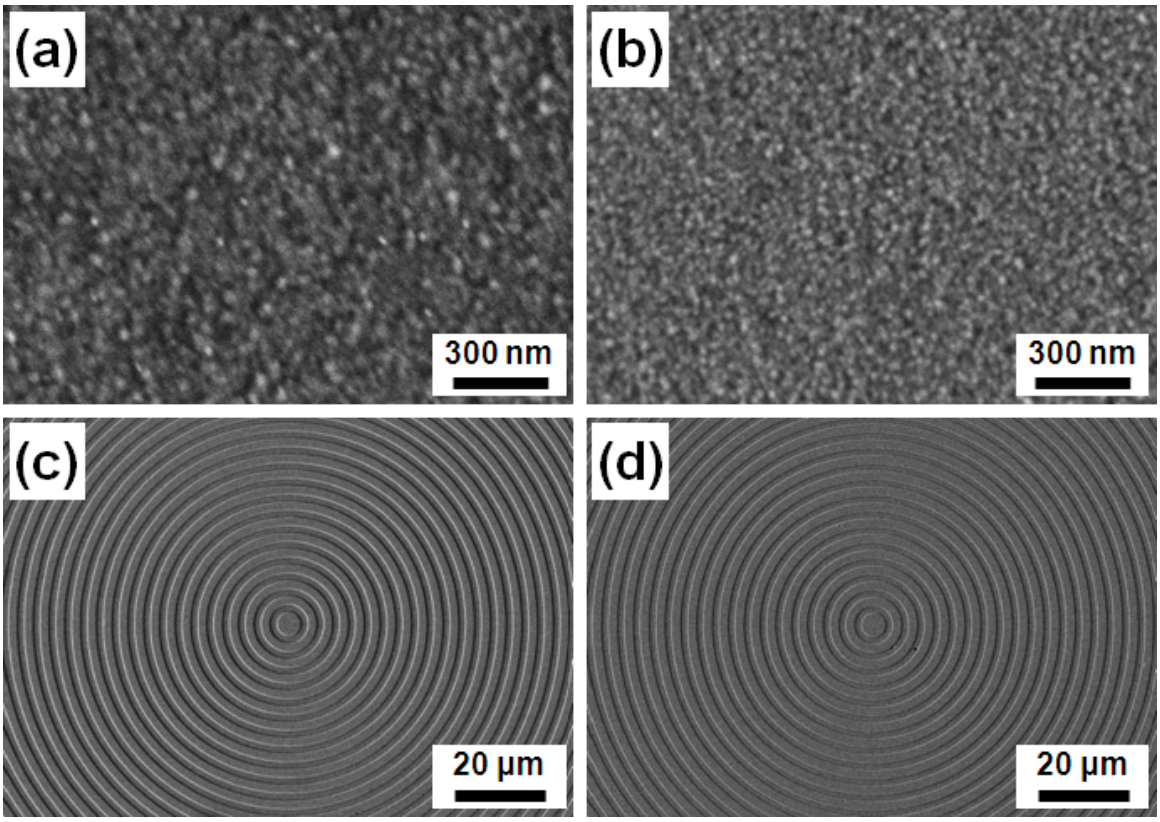

Figure 5.7 Scanning electron micrographs of a HfO_2-coated tungsten and a HfO_2-coated molybdenum bull's eye after heating at 900 ºC for 24 hr. The surface of a ridge in (a) the tungsten and (b) the molybdenum structure after heating. Overall morphology of each bull's-eye pattern of (c) tungsten with a HfO_2 layer and (d) molybdenum with a HfO_2 layer after heating. Morphology change due to heating is not observed for the structures with the protective layer.

The thermal emission properties of the HfO_2-coated bull's eyes were characterized. Figure 5.8 indicates the emission spectra of the HfO_2-coated tungsten bull's eye at 900 ºC. The measured emission spectra (figure 5.8a) have similar features to

those of the bare tungsten structure (figure 5.4a). The HfO_2-coated structure exhibits a single sharp emission peak in the normal direction. In addition, the emission peak is split and the emissivity decreases as the sample is tilted. However, the peak is broader

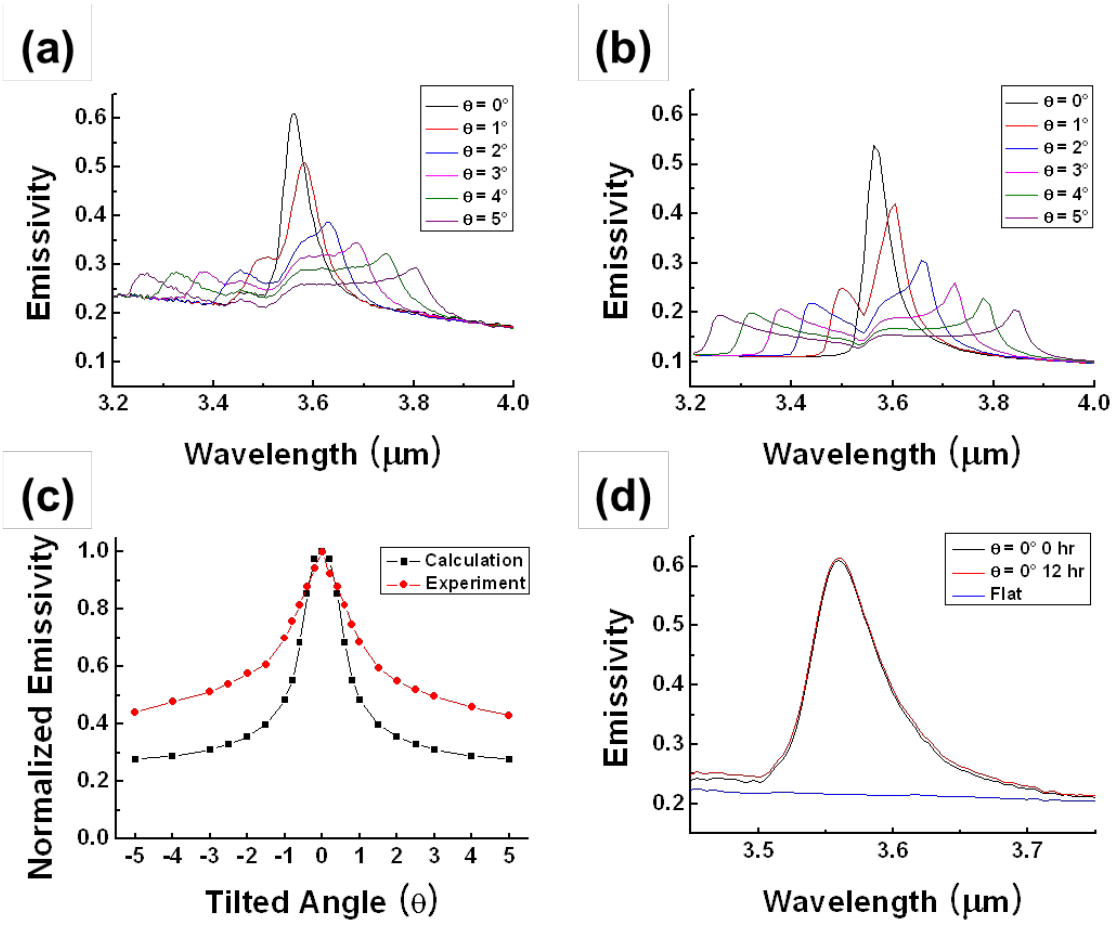

Figure 5.8 Thermal emission spectra of a HfO_2-coated tungsten bull's eye at 900 ºC. The dimensional parameters of the structure are: a fill factor of 0.52, a groove depth of 180 nm, and a period of 3.52 μm. (a) Measured thermal emission spectrum at various tilt angles (θ) from normal. The collection angle of the emission spectra is ±0.1° and a carbon emitter is utilized as a reference to calibrate the emissivity. (b) Calculated thermal emission spectra at various tilt angles (θ) from normal. The dielectric function of tungsten for 900 ºC is employed and the dielectric constant of HfO_2 is approximated as 4 without an imaginary component. (c) Angular dependence of the emissivity at the peak maximum. The measured and calculated spectra for the normal angle (θ = 0) show the maximum emissivity of 0.610 at 3.559 μm and 0.538 at 3.563 μm, respectively. The emissivity at the given wavelength for different θ is normalized with the maximum emissivity for the normal angle. (d) Comparison of the emission spectra initially and after 12 hr at 900 ºC. The measured emission spectrum for a flat tungsten film covered with the HfO_2 layer at 900 ºC is also shown.

(a FWHM of 58 nm and a Q of 61) compared to the emission spectrum of the bare structure. This peak broadening is mainly caused by the lifetime decrease of SPPs due to the HfO_2 layer ($\varepsilon = 4$)[32] because SPPs more quickly decay in the dielectric material with a higher dielectric constant.[1-2] Furthermore, the lifetime decrease of SPPs leads to an increase in the angular divergence of the peak to 2.1º and a decrease in the SPP coherence length to 97 μm (figure 5.8c). These changes in the thermal emission properties by adding the HfO_2 layer are also observed in the calculated emission spectra (figure 5.8b and 5.8c). In other words, the emission peak broadens (FWHM of 57 nm) and its angular divergence increases ($\Delta\theta = 1.5$º). However, the introduction of the HfO_2 layer greatly improves the thermal stability of the structures. As shown in figure 5.8d, even after 12 hr at 900 ºC, the HfO_2-coated tungsten bull's eye exhibits the identical emission spectrum with the same position and width of the peak. Therefore, this structure can potentially be applied as a radiation source.

Moreover, the coating of the HfO_2 layer can enhance the thermal stability of the molybdenum structures as well. While a bare molybdenum bull's eye could not support SPPs at even 600 ºC due to the oxidation of the structure, the HfO_2-coated molybdenum bull's eye exhibited tailored emission spectra at 900 ºC (figure 5.9). Compared to the HfO_2-coated tungsten structure, the HfO_2-coated molybdenum bull's eye shows a slightly narrower emission peak with a FWHM of 55 nm and a Q of 65 (figure 5.9a). In addition, the angular divergence of the peak also has a smaller value of 1.4º, giving the SPP coherence length of 145 μm (figure 5.9c). Since the thermal stability of the HfO_2-coated molybdenum bull's eye was confirmed by heating at 900 ºC for 12 hr (figure 5.9d), the HfO_2-coated molybdenum structures can potentially provide another candidate for an infrared radiation source, and with a better angular resolution than the tungsten structures.

Since the dielectric function of molybdenum at high temperatures has apparently not been reported, we employed the dielectric function for room temperature[33] to obtain the emission spectrum of the molybdenum structure via numerical simulation. Therefore, figure 5.9b indicates the calculated emission spectra of the HfO_2-coated molybdenum bull's eye using these values. While similar features such as the peak splitting and

emissivity decrease at off-normal angles are predicted, the calculated results show large differences with the measured results in terms of the overall emissivity and the width of the peak. In other words, the calculated emission spectra exhibit a narrower emission peak with smaller emissivity compared to the measured spectra. This discrepancy is

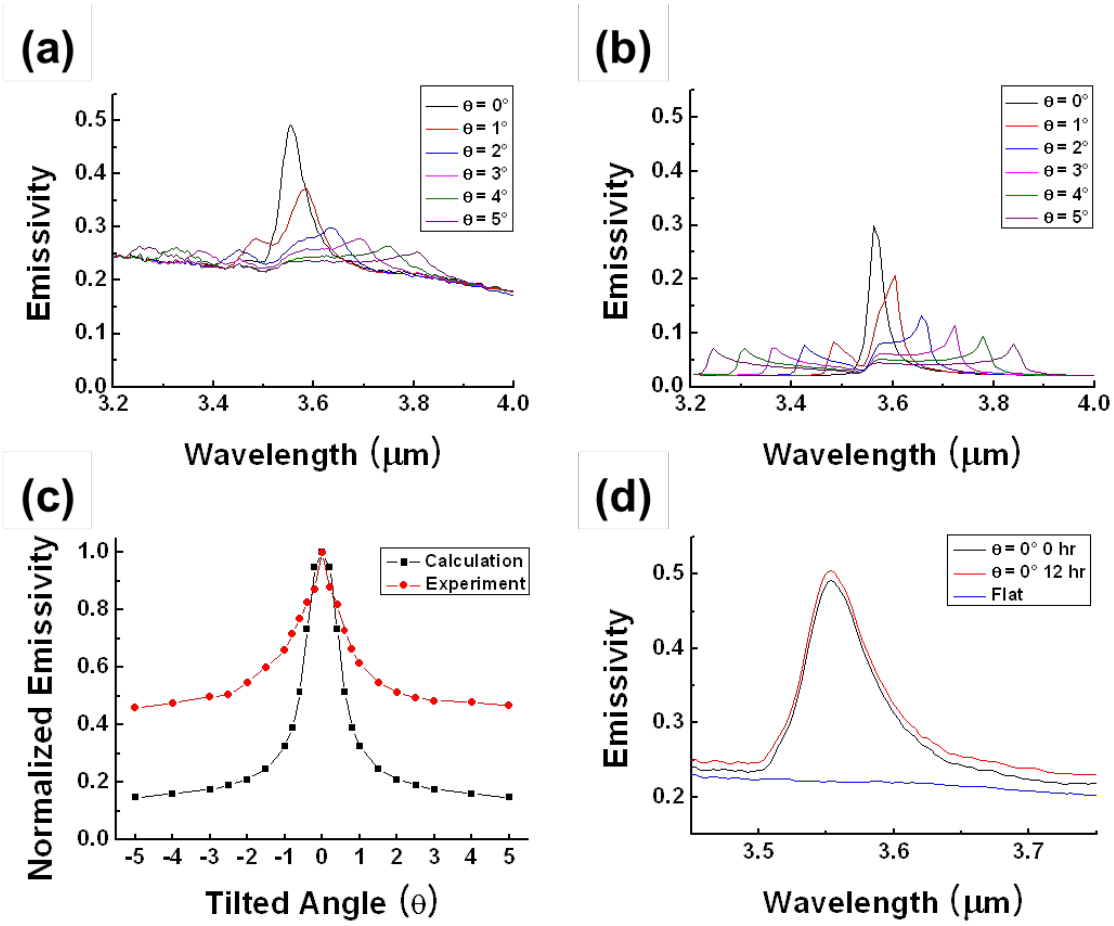

Figure 5.9 Thermal emission spectra of a HfO_2-coated molybdenum bull's eye at 900 ºC. The dimensional parameters of the structure are: a fill factor of 0.54, a groove depth of 180 nm, and a period of 3.52 μm. (a) Measured thermal emission spectra at various tilt angles (θ) from normal. The collection angle of the emission spectrum is ±0.1° and a carbon emitter is utilized as a reference to calibrate the emissivity. (b) Calculated thermal emission spectra at various tilt angles (θ) from normal. The dielectric function of molybdenum for room temperature is employed and the dielectric constant of HfO_2 is approximated as 4 without an imaginary component. (c) Angular dependence of the emissivity at the peak maximum. The measured and calculated spectra for the normal angle (θ = 0) show the emissivity of 0.492 at 3.554 μm and 0.299 at 3.563 μm, respectively. The emissivity at the given wavelength for different θ is normalized with the maximum emissivity for the normal angle. (d) Comparison of the emission spectra initially and after 12 hr at 900 ºC. The measured emission spectrum for a flat molybdenum film covered with the HfO_2 layer at 900 ºC is also shown.

mostly due to applying the inaccurate dielectric function because in general metals at higher temperature are lossier for SPPs, leading to a broadening of the emission peak and an increase in the overall emissivity. Therefore, more reasonable results by theoretical calculation would presumably be obtained if the dielectric function of molybdenum at the actual temperature was available.

5.3 Conclusions

In conclusion, we have demonstrated tailored thermal emission from a metallic bull's-eye structure. Thermally excited SPPs can be successfully coupled to light on the metallic bull's eye with a properly designed geometry. As a result, the thermal emission spectrum of the tungsten bull's eye shows a very narrow emission peak with a small angular divergence in the normal direction. This result is highly consistent with the predicted result by theoretical calculation. Furthermore, the coating of a HfO_2 layer on the metal surfaces via ALD can prevent the deformation and oxidation of the metal structures and thereby the thermal stability of the structures can be improved. Consequently, we have shown that a simple thermal process, that is heating of a metallic bull's eye, can provide a novel radiation source that generates a unidirectional monochromatic beam. This ability can play an important role in the effective exploitation of thermal energy.

5.4 Experimental Section

Fabrication of metallic bull's-eye structures

The silicon templates for metallic bull's-eye structures were prepared via photolithography. Positive photoresist (Shipley, Microposit S1805) was spin-coated at 4000 rpm on pre-cleaned silicon substrates and then exposed under an ultraviolet lamp through a chrome-on-glass mask with a mask aligner (Karl Suss MA6). The photoresist on the exposed areas was removed in a developing solution (Shipley, Microposit 351 developer:deionized water = 1:5). The patterns of the photoresist layer were transferred to

the underlying silicon substrates by reactive-ion etching (RIE). The RIE process was performed at a power of 25 W and a pressure of 100 mTorr with CF_4 and O_2 gas flow rates of 40 sccm and 4 sccm, respectively. The etching rate was about 0.6 nm/s and the depth of the grooves was controlled by varying the process time.

Tungsten and molybdenum layers were deposited with DC magnetron sputtering at a power of 150 W. The diameter of the sputtering targets was 2 inches. The pressure in the sputtering chamber was maintained at 6 mTorr with argon during deposition and the source-to-substrate distance was fixed as 13 cm. The sputtering time for each material was controlled to obtain about 160-nm-thick layers.

In our previous work (chapter 4), metallic bull's eyes had been fabricated by the deposition of metal layers on flat silicon substrates followed by RIE patterning of the metal layers.[22, 34] However, since this approach needs to etch the polycrystalline metal layers with a non-uniform etching rate due to the different grain orientations, the etched grooves had very rough surfaces (figure 4.7, RMS roughness of ~10 nm).[34] In contrast, the bull's eyes prepared in this study show much smoother surfaces at both the ridges and the grooves.

Deposition of a protective oxide layer on metal surfaces

To enhance the thermal stability of metallic bull's eyes, their surfaces were coated with a HfO_2 layer via atomic layer deposition (ALD, Picosun R150B).[30-31] Tetrakis(ethylmethylamido)hafnium (TEMAH, $Hf[N(CH_3)(C2H_5)]_4$) was utilized as a precursor and reacted with water at 200 ºC. TEMAH and water vapors were alternatively entrained in the N_2 carrier flow of 100 sccm and the pulse time for both vapors was 0.1 s. One ALD reaction cycle was defined as one dose of the precursor followed by a 6-s purge and then one dose of water followed by a 8-s purge. A 11-nm-thick HfO_2 layer was formed on the metal surfaces after 125 reaction cycles.

Characterization of the surface morphology

An atomic force microscope (AFM, Agilent 5500) was utilized to characterize the surface morphology of the metal films. All AFM images were obtained by using tapping mode and the RMS roughness of the metal surfaces was determined with $2.5 \times 2.5\ \mu m^2$ scans.

Alignment of the experimental setup for thermal emission measurement

Since the thermal emission from the bull's eye is highly directional, the experimental setup needs to be aligned precisely to measure the emission spectrum. Figure 5.3a describes the setup and contains the abbreviation of each component. The alignment was done by the following procedure. (i) The position of P2 was fixed and utilized as the standard point. (ii) A laser beam coming from the FT-IR spectrometer was aligned to the center of P2 by adjusting the tilt angle of FM. (iii) The center position of P1 was determined by using the laser beam. (iv) The tilt angle of M was adjusted to reflect the laser beam to the center of P1. (v) M is turned without changing the tilt angle to reflect the laser beam to the center of HC. (vi) The position of P3 was determined by using the laser beam. (vii) The sample was placed on the center of HC. (viii) The tilt angle of the HC was adjusted by using a goniometer to align the reflected laser beam by the sample to the center of P1. (ix) The size of the hole of P3 was controlled to block the thermal emission from the surrounding regions. (x) The size of the holes of P1 and P2 was controlled to obtain a collection angle of $\pm 0.1^{o}$.

We employed FM and M made from silver, which is highly reflective in the infrared wavelength range. In addition, a sapphire flat with a high transmittance in the infrared wavelength range was utilized as a window for HC to minimize the loss of thermal emission from the bull's eye.

Measurement of thermal emission spectra

For the measurement of the thermal emission spectra, the heating chamber (Linkam TS1500) was evacuated with a turbomolecular pump (Varian, Turbo-V 70).

After the chamber pressure reached around 10^{-5} mbar, the sample was heated to 900 ºC at a ramping rate of 20 ºC/min. During the measurement, the temperature of the heater was constant (900±1 ºC) and the outside of the chamber was kept at room temperature by water circulation.

The thermal emission spectrum from the bull's eye was measured with a Fourier-transform infrared (FT-IR, Bruker-Vertex 80) spectrometer. Due to the IR wavelength of the emission peak, a KBr beam splitter and a liquid-nitrogen-cooled InSb detector were utilized. The emission spectrum from the sample was scanned 4000 times in the wavenumber range between 3400 and 2400 cm^{-1} with a resolution of 4 or 8 cm^{-1}. To calibrate the emissivity, we assumed that the thermal emission from a carbon emitter (pelletized carbon nanopowder, Aldrich #633100) is equivalent to that from a blackbody at the given temperature. Then, the emission spectrum from the sample was normalized by that of the carbon emitter obtained under the same measuring conditions. The tilt angle of the sample could be accurately controlled by using a goniometer on which the heating chamber was mounted.

Calculation of thermal emission spectra via numerical simulation

We assumed that the size of the bull's eye is sufficiently large that we can neglect the effect of the center and the boundary of the structure on its thermal emission properties. Hence, the bull's eye can be approximated as a series of linear gratings oriented around the center.[17] Since the absorptivity is equivalent to the emissivity according to Kirchhoff's law,[23-24] the averaged absorptivity of linear gratings evenly distributed in all directions yields the emissivity of the bull's eye. For the calculation, we used the transfer matrix formalism[35] and a unit cell is discretized by a 80 × 80 mesh. The simulation was performed for each structure using the dimensional parameters determined by SEM. While all bull's eyes had nominally the same period (3.52 μm) and groove depth (180 nm), a fill factor for each structure showed small variations. The bare tungsten, HfO_2-coated tungsten, and HfO_2-coated molybdenum structures had a fill factor of 0.5, 0.52, and 0.54, respectively. The thickness of the HfO_2 layer was 11 nm and its

dielectric constant was assumed to be 4 without an imaginary component.[32] For tungsten, the dielectric function at 900 ºC was employed to obtain the emission spectrum.[25] However, due to the absence of data for molybdenum, the dielectric function for room temperature was utilized for the calculation. This resulted in the large difference between the measured and calculated results in terms of the overall emissivity and the width of the emission peak.

5.5 References

[1] H. Raether, *Surface Plasmons on Smooth and Rough Surfaces and on Gratings*. Springer-Verlag: Berlin, 1988.

[2] W. L. Barnes, A. Dereux, T. W. Ebbesen, "Surface Plasmon Subwavelength Optics," *Nature* **2003,** *424*, 824.

[3] E. Ozbay, "Plasmonics: Merging Photonics and Electronics at Nanoscale Dimensions," *Science* **2006,** *311*, 189.

[4] H. A. Atwater, "The Promise of Plasmonics," *Sci. Am.* **2007,** *296*, 56.

[5] A. Polman, "Applied Physics: Plasmonics Applied," *Science* **2008,** *322*, 868.

[6] T. W. Ebbesen, H. J. Lezec, H. F. Ghaemi, T. Thio, P. A. Wolff, "Extraordinary Optical Transmission through Sub-wavelength Hole Arrays," *Nature* **1998,** *391*, 667.

[7] H. J. Lezec, A. Degiron, E. Devaux, R. A. Linke, L. Martin-Moreno, F. J. Garcia-Vidal, T. W. Ebbesen, "Beaming Light from a Subwavelength Aperture," *Science* **2002,** *297*, 820.

[8] Y. De Wilde, F. Formanek, R. Carminati, B. Gralak, P.-A. Lemoine, K. Joulain, J.-P. Mulet, Y. Chen, J.-J. Greffet, "Thermal Radiation Scanning Tunnelling Microscopy," *Nature* **2006,** *444*, 740.

[9] J.-J. Greffet, R. Carminati, K. Joulain, J.-P. Mulet, S. Mainguy, Y. Chen, "Coherent Emission of Light by Thermal Sources," *Nature* **2002,** *416*, 61.

[10] P. J. Hesketh, J. N. Zemel, B. Gebhart, "Organ Pipe Radiant Modes of Periodic Micromachined Silicon Surfaces," *Nature* **1986,** *324*, 549.

[11] N. Dahan, A. Niv, G. Biener, Y. Gorodetski, V. Kleiner, E. Hasman, "Extraordinary Coherent Thermal Emission from SiC due to Coupled Resonant Cavities," *J. Heat Transfer* **2008,** *130*, 112401.

[12] N. Dahan, A. Niv, G. Biener, V. Kleiner, E. Hasman, "Space-Variant Polarization Manipulation of a Thermal Emission by a SiO_2 Subwavelength Grating Supporting Surface Phonon-Polaritons," *Appl. Phys. Lett.* **2005,** *86*, 191102.

[13] N. Dahan, A. Niv, G. Biener, Y. Gorodetski, V. Kleiner, E. Hasman, "Enhanced Coherency of Thermal Emission: Beyond the Limitation Imposed by Delocalized Surface Waves," *Phys. Rev. B* **2007,** *76*, 045427.

[14] M. Laroche, C. Arnold, F. Marquier, R. Carminati, J. J. Greffet, S. Collin, N. Bardou, J. L. Pelouard, "Highly Directional Radiation Generated by a Tungsten Thermal Source," *Opt. Lett.* **2005,** *30*, 2623.

[15] G. Biener, N. Dahan, A. Niv, V. Kleiner, E. Hasman, "Highly Coherent Thermal Emission Obtained by Plasmonic Bandgap Structures," *Appl. Phys. Lett.* **2008,** *92*, 081913.

[16] F. Marquier, C. Arnold, M. Laroche, J. J. Greffet, Y. Chen, "Degree of Polarization of Thermal Light Emitted by Gratings Supporting Surface Waves," *Opt. Express* **2008,** *16*, 5305.

[17] S. E. Han, D. J. Norris, "Beaming Thermal Emission from Hot Metallic Bull's Eyes," *Opt. Express* **2010,** *18*, 4829.

[18] K. Joulain, J.-P. Mulet, F. Marquier, R. Carminati, J.-J. Greffet, "Surface Electromagnetic Waves Thermally Excited: Radiative Heat Transfer, Coherence Properties and Casimir Forces Revisited in the Near Field," *Surf. Sci. Rep.* **2005,** *57*, 59.

[19] Y.-T. Chang, Y.-H. Ye, D.-C. Tzuang, Y.-T. Wu, C.-H. Yang, C.-F. Chan, Y.-W. Jiang, S.-C. Lee, "Localized Surface Plasmons in Al/Si Structure and Ag/SiO_2/Ag Emitter with Different Concentric Metal Rings," *Appl. Phys. Lett.* **2008,** *92*, 233109.

[20] P. Nagpal, N. C. Lindquist, S.-H. Oh, D. J. Norris, "Ultrasmooth Patterned Metals for Plasmonics and Metamaterials," *Science* **2009,** *325*, 594.

[21] J. H. Park, P. Nagpal, S.-H. Oh, D. J. Norris, "Improved Dielectric Functions in Metallic Films Obtained via Template Stripping," *Appl. Phys. Lett.* **2012,** *100*, 081105.

[22] P. Nagpal, *Ph.D. Thesis: Metal Photonics and Plasmonics for Energy Generation*. University of Minnesota: Minneapolis, 2009.

[23] J.-J. Greffet, M. Nieto-Vesperinas, "Field Theory for Generalized Bidirectional Reflectivity: Derivation of Helmholtz's Reciprocity Principle and Kirchhoff's Law," *J. Opt. Soc. Am. A* **1998,** *15*, 2735.

[24] S. E. Han, "Theory of Thermal Emission from Periodic Structures," *Phys. Rev. B* **2009,** *80*, 155108.

[25] L. N. Aksyutov, "Temperature Dependence of the Optical Constants of Tungsten and Gold," *J. Appl. Spectrosc.* **1977,** *26*, 656.

[26] J. H. Park, P. Ambwani, M. Manno, N. C. Lindquist, P. Nagpal, S.-H. Oh, C. Leighton, D. J. Norris, "Single-Crystalline Silver Films for Plasmonics," *Adv. Mater.* **2012,** *24*, 3988.

[27] N. R. Denny, S. E. Han, D. J. Norris, A. Stein, "Effects of Thermal Processes on the Structure of Monolithic Tungsten and Tungsten Alloy Photonic Crystals," *Chem. Mater.* **2007,** *19*, 4563.

[28] E. A. Gulbransen, K. F. Andrew, F. A. Brassart, "Oxidation of Molybdenum 550 °C to 1700 °C," *J. Electrochem. Soc.* **1963,** *110*, 952.

[29] J. B. B. Heyns, J. J. Cruywagen, S. A. Kinkead, "Yellow Molybdenum(VI) Oxide Dihydrate" in *Inorganic Syntheses*, John Wiley & Sons, Inc.: 2007; pp 191.

[30] D. M. Hausmann, E. Kim, J. Becker, R. G. Gordon, "Atomic Layer Deposition of Hafnium and Zirconium Oxides Using Metal Amide Precursors," *Chem. Mater.* **2002,** *14*, 4350.

[31] K. Kukli, M. Ritala, T. Sajavaara, J. Keinonen, M. Leskelä, "Atomic Layer Deposition of Hafnium Dioxide Films from Hafnium Tetrakis(ethylmethylamide) and Water," *Chem. Vap. Deposition* **2002,** *8*, 199.

[32] D. H. Triyoso, R. I. Hegde, J. B. E. White, P. J. Tobin, "Physical and Electrical Characteristics of Atomic-Layer-Deposited Hafnium Dioxide Formed Using Hafnium Tetrachloride and Tetrakis(ethylmethylaminohafnium)," *J. Appl. Phys.* **2005,** *97*, 124107.

[33] E. D. Palik, *Handbook of Optical Constants of Solids*. Academic Press: Orlando, 1985.

[34] J. H. Park, P. Nagpal, K. M. McPeak, N. C. Lindquist, S.-H. Oh, D. J. Norris, "Fabrication of Smooth Patterned Structures of Refractory Metals, Semiconductors, and Oxides via Template Stripping," *unpublished*.

[35] J. B. Pendry, A. MacKinnon, "Calculation of Photon Dispersion Relations," *Phys. Rev. Lett.* **1992,** *69*, 2772.

Bibliography

- Encyclopedia Britannica, http://www.britannica.com.
- Aksyutov, L. N., "Temperature Dependence of the Optical Constants of Tungsten and Gold," *J. Appl. Spectrosc.* **1977,** *26*, 656.
- Allione, M., Temnov, V. V., Fedutik, Y., Woggon, U., Artemyev, M. V., "Surface Plasmon Mediated Interference Phenomena in Low-Q Silver Nanowire Cavities," *Nano Lett.* **2008,** *8*, 31.
- Anker, J. N., Hall, W. P., Lyandres, O., Shah, N. C., Zhao, J., Van Duyne, R. P., "Biosensing with Plasmonic Nanosensors," *Nat. Mater.* **2008,** *7*, 442.
- Ashcroft, N. W., Mermin, N. D., *Solid State Physics*. Saunders College: Philadelphia, 1976.
- Aspnes, D. E., Theeten, J. B., Hottier, F., "Investigation of Effective-Medium Models of Microscopic Surface Roughness by Spectroscopic Ellipsometry," *Phys. Rev. B* **1979,** *20*, 3292.
- Aspnes, D. E., "Optical Properties of Thin Films," *Thin Solid Films* **1982,** *89*, 249.
- Atwater, H. A., "The Promise of Plasmonics," *Sci. Am.* **2007,** *296*, 56.
- Atwater, H. A., Polman, A., "Plasmonics for Improved Photovoltaic Devices," *Nat. Mater.* **2010,** *9*, 205.
- Barhoumi, A., Zhang, D., Tam, F., Halas, N. J., "Surface-Enhanced Raman Spectroscopy of DNA," *J. Am. Chem. Soc.* **2008,** *130*, 5523.
- Barnes, W. L., Dereux, A., Ebbesen, T. W., "Surface Plasmon Subwavelength Optics," *Nature* **2003,** *424*, 824.
- Baski, A. A., Fuchs, H., "Epitaxial Growth of Silver on Mica as Studied by AFM and STM," *Surf. Sci.* **1994,** *313*, 275.

- Bauer, T., *Thermophotovoltaics: Basic Principles and Critical Aspects of System Design*. Springer-Verlag: Berlin, 2011.
- Bialas, H., Heneka, K., "Epitaxy of FCC Metals on Dielectric Substrates," *Vacuum* **1994,** *45*, 79.
- Biener, G., Dahan, N., Niv, A., Kleiner, V., Hasman, E., "Highly Coherent Thermal Emission Obtained by Plasmonic Bandgap Structures," *Appl. Phys. Lett.* **2008,** *92*, 081913.
- Bishnoi, S. W., Rozell, C. J., Levin, C. S., Gheith, M. K., Johnson, B. R., Johnson, D. H., Halas, N. J., "All-Optical Nanoscale pH Meter," *Nano Lett.* **2006,** *6*, 1687.
- Boyce, M. P., *Gas Turbine Engineering Handbook.* Gulf Professional Pub.: Boston, 2006.
- Bozhevolnyi, S. I., Volkov, V. S., Devaux, E., Laluet, J. Y., Ebbesen, T. W., "Channel Plasmon Subwavelength Waveguide Components Including Interferometers and Ring Resonators," *Nature* **2006,** *440*, 508.
- Brolo, A. G., Gordon, R., Leathem, B., Kavanagh, K. L., "Surface Plasmon Sensor Based on the Enhanced Light Transmission through Arrays of Nanoholes in Gold Films," *Langmuir* **2004,** *20*, 4813.
- Brongersma, M. L., Shalaev, V. M., "The Case for Plasmonics," *Science* **2010,** *328*, 440.
- Campbell, S. A., *The Science and Engineering of Microelectronic Fabrication*. Oxford University Press: New York, 2001.
- Challener, W. A., Peng, C., Itagi, A. V., Karns, D., Peng, W., Peng, Y., Yang, X., Zhu, X., Gokemeijer, N. J., Hsia, Y.-T., Ju, G., Rottmayer, R. E., Seigler, M. A., Gage, E. C., "Heat-Assisted Magnetic Recording by a Near-Field Transducer with Efficient Optical Energy Transfer," *Nat. Photonics* **2009,** *3*, 220.

- Chang, Y.-T., Ye, Y.-H., Tzuang, D.-C., Wu, Y.-T., Yang, C.-H., Chan, C.-F., Jiang, Y.-W., Lee, S.-C., "Localized Surface Plasmons in Al/Si Structure and Ag/SiO_2/Ag Emitter with Different Concentric Metal Rings," *Appl. Phys. Lett.* **2008,** *92*, 233109.
- Chou, S. Y., Krauss, P. R., Renstrom, P. J., "Imprint Lithography with 25-Nanometer Resolution," *Science* **1996,** *272*, 85.
- Coutts, T. J., Fitzgerald, M. C., "Thermophotovoltaics," *Sci. Am.* **1998,** *279*, 90.
- Dahan, N., Niv, A., Biener, G., Kleiner, V., Hasman, E., "Space-Variant Polarization Manipulation of a Thermal Emission by a SiO_2 Subwavelength Grating Supporting Surface Phonon-Polaritons," *Appl. Phys. Lett.* **2005,** *86*, 191102.
- Dahan, N., Niv, A., Biener, G., Gorodetski, Y., Kleiner, V., Hasman, E., "Enhanced Coherency of Thermal Emission: Beyond the Limitation Imposed by Delocalized Surface Waves," *Phys. Rev. B* **2007,** *76*, 045427.
- Dahan, N., Niv, A., Biener, G., Gorodetski, Y., Kleiner, V., Hasman, E., "Extraordinary Coherent Thermal Emission from SiC due to Coupled Resonant Cavities," *J. Heat Transfer* **2008,** *130*, 112401.
- De Leon, I., Berini, P., "Amplification of Long-Range Surface Plasmons by a Dipolar Gain Medium," *Nat. Photonics* **2010,** *4*, 382.
- De Wilde, Y., Formanek, F., Carminati, R., Gralak, B., Lemoine, P.-A., Joulain, K., Mulet, J.-P., Chen, Y., Greffet, J.-J., "Thermal Radiation Scanning Tunnelling Microscopy," *Nature* **2006,** *444*, 740.
- Denny, N. R., Han, S. E., Norris, D. J., Stein, A., "Effects of Thermal Processes on the Structure of Monolithic Tungsten and Tungsten Alloy Photonic Crystals," *Chem. Mater.* **2007,** *19*, 4563.

- DeRose, J. A., Thundat, T., Nagahara, L. A., Lindsay, S. M., "Gold Grown Epitaxially on Mica: Conditions for Large Area Flat Faces," *Surf. Sci.* **1991,** *256*, 102.
- Dhere, N. G., Waterhouse, D. L., Sundaram, K. B., Melendez, O., Parikh, N. R., Patnaik, B., "Studies on Chemical Bath Deposited Cadmium Sulfide Films by Buffer Solution Technique," *J. Mater. Sci. Mater. Electron.* **1995,** *6*, 52.
- Ditlbacher, H., Hohenau, A., Wagner, D., Kreibig, U., Rogers, M., Hofer, F., Aussenegg, F. R., Krenn, J. R., "Silver Nanowires as Surface Plasmon Resonators," *Phys. Rev. Lett.* **2005,** *95*, 257403.
- Drude, P., "Zur Elektronentheorie der Metalle," *Annalen der Physik* **1900,** *306*, 566.
- Ebbesen, T. W., Lezec, H. J., Ghaemi, H. F., Thio, T., Wolff, P. A., "Extraordinary Optical Transmission through Sub-wavelength Hole Arrays," *Nature* **1998,** *391*, 667.
- Einstein, A., "Über einen die Erzeugung und Verwandlung des Lichtes betreffenden heuristischen Gesichtspunkt," *Annalen der Physik* **1905,** *322*, 132.
- Fenstermaker, C. A., McCrackin, F. L., "Errors Arising from Surface Roughness in Ellipsometric Measurement of the Refractive Index of a Surface," *Surf. Sci.* **1969,** *16*, 85.
- Ferry, V. E., Verschuuren, M. A., Li, H. B. T., Verhagen, E., Walters, R. J., Schropp, R. E. I., Atwater, H. A., Polman, A., "Light Trapping in Ultrathin Plasmonic Solar Cells," *Opt. Express* **2010,** *18*, A237.
- Gates, B. D., Xu, Q., Stewart, M., Ryan, D., Willson, C. G., Whitesides, G. M., "New Approaches to Nanofabrication: Molding, Printing, and Other Techniques," *Chem. Rev.* **2005,** *105*, 1171.

- Geissler, M., Schmid, H., Bietsch, A., Michel, B., Delamarche, E., "Defect-Tolerant and Directional Wet-Etch Systems for Using Monolayers as Resists," *Langmuir* **2002,** *18*, 2374.
- Goswami, D. Y., Kreith, F., *Energy Conversion*. Taylor & Francis: Boca Raton, 2008.
- Gramotnev, D. K., Bozhevolnyi, S. I., "Plasmonics Beyond the Diffraction Limit," *Nat. Photonics* **2010,** *4*, 83.
- Green, M. A., *Third Generation Photovoltaics: Advanced Solar Energy Conversion*. Springer: 2005.
- Greffet, J.-J., Nieto-Vesperinas, M., "Field Theory for Generalized Bidirectional Reflectivity: Derivation of Helmholtz's Reciprocity Principle and Kirchhoff's Law," *J. Opt. Soc. Am. A* **1998,** *15*, 2735.
- Greffet, J.-J., Carminati, R., Joulain, K., Mulet, J.-P., Mainguy, S., Chen, Y., "Coherent Emission of Light by Thermal Sources," *Nature* **2002,** *416*, 61.
- Gulbransen, E. A., Andrew, K. F., Brassart, F. A., "Oxidation of Molybdenum 550 °C to 1700 °C," *J. Electrochem. Soc.* **1963,** *110*, 952.
- Han, S. E., *Ph.D. Thesis: Thermal Emission Control with Periodic Microstructures*. University of Minnesota: Minneapolis, 2009.
- Han, S. E., "Theory of Thermal Emission from Periodic Structures," *Phys. Rev. B* **2009,** *80*, 155108.
- Han, S. E., Norris, D. J., "Beaming Thermal Emission from Hot Metallic Bull's Eyes," *Opt. Express* **2010,** *18*, 4829.
- Hausmann, D. M., Kim, E., Becker, J., Gordon, R. G., "Atomic Layer Deposition of Hafnium and Zirconium Oxides Using Metal Amide Precursors," *Chem. Mater.* **2002,** *14*, 4350.
- Hegner, M., Wagner, P., Semenza, G., "Ultralarge Atomically Flat Template-Stripped Au Surfaces for Scanning Probe Microscopy," *Surf. Sci.* **1993,** *291*, 39.

- Heinzel, A., Boerner, V., Gombert, A., Bläsi, B., Wittwer, V., Luther, J., "Radiation Filters and Emitters for the NIR Based on Periodically Structured Metal Surfaces," *J. Mod. Optic.* **2000,** *47*, 2399.
- Heyns, J. B. B., Cruywagen, J. J., Kinkead, S. A., "Yellow Molybdenum(VI) Oxide Dihydrate" in *Inorganic Syntheses*, John Wiley & Sons, Inc.: 2007; pp 191.
- Huang, J.-S., Callegari, V., Geisler, P., Brüning, C., Kern, J., Prangsma, J. C., Wu, X., Feichtner, T., Ziegler, J., Weinmann, P., Kamp, M., Forchel, A., Biagioni, P., Sennhauser, U., Hecht, B., "Atomically Flat Single-Crystalline Gold Nanostructures for Plasmonic Nanocircuitry," *Nat. Commun.* **2010,** *1*, 150.
- Hur, T.-B., Kim, H. K., Blachere, J., "Epitaxial Growth of Ag Films on Native-Oxide-Covered Si Substrates," *Phys. Rev. B* **2007,** *75*, 205306.
- Im, H., Bantz, K. C., Lindquist, N. C., Haynes, C. L., Oh, S.-H., "Vertically Oriented Sub-10-nm Plasmonic Nanogap Arrays," *Nano Lett.* **2010,** *10*, 2231.
- Jeong, S.-J., Xia, G., Kim, B. H., Shin, D. O., Kwon, S.-H., Kang, S.-W., Kim, S. O., "Universal Block Copolymer Lithography for Metals, Semiconductors, Ceramics, and Polymers," *Adv. Mater.* **2008,** *20*, 1898.
- Johnson, P. B., Christy, R. W., "Optical constants of the noble metals," *Phys. Rev. B* **1972,** *6*, 4370.
- Joo, J., Chow, B. Y., Jacobson, J. M., "Nanoscale Patterning on Insulating Substrates by Critical Energy Electron Beam Lithography," *Nano Lett.* **2006,** *6*, 2021.
- Joulain, K., Mulet, J.-P., Marquier, F., Carminati, R., Greffet, J.-J., "Surface Electromagnetic Waves Thermally Excited: Radiative Heat Transfer, Coherence Properties and Casimir Forces Revisited in the Near Field," *Surf. Sci. Rep.* **2005,** *57*, 59.
- Kaser, A., Gerlach, E., "Scattering of Conduction Electrons by Surface Roughness in Thin Metal Films," *Z. Phys. B* **1995,** *97*, 139.

- Keefe, T. J., *The Nature of Light*. http://www.ccri.edu/physics/keefe/light.htm, 2007.
- Kim, E., Xia, Y. N., Whitesides, G. M., "Polymer Microstructures Formed by Molding in Capillaries," *Nature* **1995,** *376*, 581.
- Kittel, C., *Introduction to Solid State Physics*. Wiley: New York, 1966.
- Kittel, C., Kroemer, H., *Thermal Physics*. W. H. Freeman: San Francisco, 1980.
- Kukli, K., Ritala, M., Sajavaara, T., Keinonen, J., Leskelä, M., "Atomic Layer Deposition of Hafnium Dioxide Films from Hafnium Tetrakis(ethylmethylamide) and Water," *Chem. Vap. Deposition* **2002,** *8*, 199.
- Kumar, A., Biebuyck, H. A., Abbott, N. L., Whitesides, G. M., "The Use of Self-Assembled Monolayers and a Selective Etch to Generate Patterned Gold Features," *J. Am. Chem. Soc.* **1992,** *114*, 9188.
- Kumar, A., Whitesides, G. M., "Features of Gold Having Micrometer to Centimeter Dimensions Can Be Formed through a Combination of Stamping with an Elastomeric Stamp and an Alkanethiol Ink Followed by Chemical Etching," *Appl. Phys. Lett.* **1993,** *63*, 2002.
- Kuttge, M., Vesseur, E. J. R., Verhoeven, J., Lezec, H. J., Atwater, H. A., Polman, A., "Loss Mechanisms of Surface Plasmon Polaritons on Gold Probed by Cathodoluminescence Imaging Spectroscopy," *Appl. Phys. Lett.* **2008,** *93*, 113110.
- Laroche, M., Arnold, C., Marquier, F., Carminati, R., Greffet, J. J., Collin, S., Bardou, N., Pelouard, J. L., "Highly Directional Radiation Generated by a Tungsten Thermal Source," *Opt. Lett.* **2005,** *30*, 2623.
- Lezec, H. J., Degiron, A., Devaux, E., Linke, R. A., Martin-Moreno, L., Garcia-Vidal, F. J., Ebbesen, T. W., "Beaming Light from a Subwavelength Aperture," *Science* **2002,** *297*, 820.

- Lin, S. Y., Moreno, J., Fleming, J. G., "Three-Dimensional Photonic-Crystal Emitter for Thermal Photovoltaic Power Generation," *Appl. Phys. Lett.* **2003,** *83*, 380.
- Lindquist, N. C., Lesuffleur, A., Im, H., Oh, S.-H., "Sub-Micron Resolution Surface Plasmon Resonance Imaging Enabled by Nanohole Arrays with Surrounding Bragg Mirrors for Enhanced Sensitivity and Isolation," *Lab Chip* **2009,** *9*, 382.
- Lindquist, N. C., Nagpal, P., Lesuffleur, A., Norris, D. J., Oh, S.-H., "Three-Dimensional Plasmonic Nanofocusing," *Nano Lett.* **2010,** *10*, 1369.
- Lindquist, N. C., Johnson, T. W., Norris, D. J., Oh, S.-H., "Monolithic Integration of Continuously Tunable Plasmonic Nanostructures," *Nano Lett.* **2011,** *11*, 3526.
- Lindquist, N. C., Nagpal, P., McPeak, K. M., Norris, D. J., Oh, S.-H., "Engineering Metallic Nanostructures for Plasmonics and Nanophotonics," *Rep. Prog. Phys.* **2012,** *75*, 036501.
- Liu, X., Tyler, T., Starr, T., Starr, A. F., Jokerst, N. M., Padilla, W. J., "Taming the Blackbody with Infrared Metamaterials as Selective Thermal Emitters," *Phys. Rev. Lett.* **2011,** *107*, 045901.
- Luo, E. Z., Heun, S., Kennedy, M., Wollschläger, J., Henzler, M., "Surface Roughness and Conductivity of Thin Ag Films," *Phys. Rev. B* **1994,** *49*, 4858.
- Mühlschlegel, P., Eisler, H.-J., Martin, O. J. F., Hecht, B., Pohl, D. W., "Resonant Optical Antennas," *Science* **2005,** *308*, 1607.
- Mansuripur, M., Zakharian, A. R., Lesuffleur, A., Oh, S.-H., Jones, R. J., Lindquist, N. C., Im, H., Kobyakov, A., Moloney, J. V., "Plasmonic Nano-Structures for Optical Data Storage," *Opt. Express* **2009,** *17*, 14001.
- Marquier, F., Arnold, C., Laroche, M., Greffet, J. J., Chen, Y., "Degree of Polarization of Thermal Light Emitted by Gratings Supporting Surface Waves," *Opt. Express* **2008,** *16*, 5305.

- Martín-Moreno, L., García-Vidal, F. J., Lezec, H. J., Degiron, A., Ebbesen, T. W., "Theory of Highly Directional Emission from a Single Subwavelength Aperture Surrounded by Surface Corrugations," *Phys. Rev. Lett.* **2003,** *90*, 167401.
- Muhlschlegel, P., Eisler, H. J., Martin, O. J., Hecht, B., Pohl, D. W., "Resonant Optical Antennas," *Science* **2005,** *308*, 1607.
- Nagpal, P., Han, S. E., Stein, A., Norris, D. J., "Efficient Low-Temperature Thermophotovoltaic Emitters from Metallic Photonic Crystals," *Nano Lett.* **2008,** *8*, 3238.
- Nagpal, P., *Ph.D. Thesis: Metal Photonics and Plasmonics for Energy Generation*. University of Minnesota: Minneapolis, 2009.
- Nagpal, P., Lindquist, N. C., Oh, S.-H., Norris, D. J., "Ultrasmooth Patterned Metals for Plasmonics and Metamaterials," *Science* **2009,** *325*, 594.
- Ni, X., Liu, Z., Kildishev, A. V. PhotonicsDB: Optical Constants, http://nanohub.org/resources/PhotonicsDB.
- Novotny, L., van Hulst, N., "Antennas for Light," *Nat. Photonics* **2011,** *5*, 83.
- Ortega-Borges, R., Lincot, D., "Mechanism of Chemical Bath Deposition of Cadmium Sulfide Thin Films in the Ammonia-Thiourea System: In-Situ Kinetic Study and Modelization," *J. Electrochem. Soc.* **1993,** *140*, 3464.
- Ozbay, E., "Plasmonics: Merging Photonics and Electronics at Nanoscale Dimensions," *Science* **2006,** *311*, 189.
- Palik, E. D., *Handbook of Optical Constants of Solids*. Academic Press: Orlando, 1985.
- Park, J. H., Nagpal, P., McPeak, K. M., Lindquist, N. C., Oh, S.-H., Norris, D. J., "Fabrication of Smooth Patterned Structures of Refractory Metals, Semiconductors, and Oxides via Template Stripping," *unpublished*.

- Park, J. H., Ambwani, P., Manno, M., Lindquist, N. C., Nagpal, P., Oh, S.-H., Leighton, C., Norris, D. J., "Single-Crystalline Silver Films for Plasmonics," *Adv. Mater.* **2012,** *24*, 3988.
- Park, J. H., Nagpal, P., Oh, S.-H., Norris, D. J., "Improved Dielectric Functions in Metallic Films Obtained via Template Stripping," *Appl. Phys. Lett.* **2012,** *100*, 081105.
- Park, M., Harrison, C., Chaikin, P. M., Register, R. A., Adamson, D. H., "Block Copolymer Lithography: Periodic Arrays of Similar to 10(11) Holes in 1 Square Centimeter," *Science* **1997,** *276*, 1401.
- Pendry, J. B., MacKinnon, A., "Calculation of Photon Dispersion Relations," *Phys. Rev. Lett.* **1992,** *69*, 2772.
- Polman, A., "Applied Physics: Plasmonics Applied," *Science* **2008,** *322*, 868.
- Raether, H., *Surface Plasmons on Smooth and Rough Surfaces and on Gratings*. Springer-Verlag: Berlin, 1988.
- Reichelt, K., Lutz, H. O., "Hetero-Epitaxial Growth of Vacuum Evaporated Silver and Gold," *J. Cryst. Growth* **1971,** *10*, 103.
- Reif, F., *Fundamentals of Statistical and Thermal Physics*. McGraw-Hill: New York, 1965.
- Rephaeli, E., Fan, S., "Tungsten Black Absorber for Solar Light with Wide Angular Operation Range," *Appl. Phys. Lett.* **2008,** *92*, 211107.
- Richardson, O. W., "The Emission of Electrons from Tungsten at High Temperatures: An Experimental Proof That the Electric Current in Metals Is Carried by Electrons," *Science* **1913,** *38*, 57.
- Rueda, A., Vogel, N., Kreiter, M., "Characterization of Gold Films by Surface Plasmon Spectroscopy: Large Errors and Small Consequences," *Surf. Sci.* **2009,** *603*, 491.

- Sanders, A. W., Routenberg, D. A., Wiley, B. J., Xia, Y., Dufresne, E. R., Reed, M. A., "Observation of Plasmon Propagation, Redirection, and Fan-Out in Silver Nanowires," *Nano Lett.* **2006,** *6*, 1822.
- Sergeant, N. P., Agrawal, M., Peumans, P., "High Performance Solar-Selective Absorbers Using Coated Sub-Wavelength Gratings," *Opt. Express* **2010,** *18*, 5525.
- Smith, D. R., Pendry, J. B., Wiltshire, M. C. K., "Metamaterials and Negative Refractive Index," *Science* **2004,** *305*, 788.
- Sosa, N. E., Liu, J., Chen, C., Marks, T. J., Hersam, M. C., "Nanoscale Writing of Transparent Conducting Oxide Features with a Focused Ion Beam," *Adv. Mater.* **2009,** *21*, 721.
- Stockman, M. I., "Nanofocusing of Optical Energy in Tapered Plasmonic Waveguides," *Phys. Rev. Lett.* **2004,** *93*, 137404.
- Sun, C.-H., Linn, N. C., Jiang, P., "Templated Fabrication of Periodic Metallic Nanopyramid Arrays," *Chem. Mater.* **2007,** *19*, 4551.
- Temnov, V. V., Woggon, U., Dintinger, J., Devaux, E., Ebbesen, T. W., "Surface Plasmon Interferometry: Measuring Group Velocity of Surface Plasmons," *Opt. Lett.* **2007,** *32*, 1235.
- Thomson, J. J., "Cathode Rays," *The Electrician* **1897,** *39*, 104.
- Triyoso, D. H., Hegde, R. I., White, J. B. E., Tobin, P. J., "Physical and Electrical Characteristics of Atomic-Layer-Deposited Hafnium Dioxide Formed Using Hafnium Tetrachloride and Tetrakis(ethylmethylaminohafnium)," *J. Appl. Phys.* **2005,** *97*, 124107.
- Valentine, J., Zhang, S., Zentgraf, T., Ulin-Avila, E., Genov, D. A., Bartal, G., Zhang, X., "Three-Dimensional Optical Metamaterial with a Negative Refractive Index," *Nature* **2008,** *455*, 376.

- van Wijngaarden, J. T., Verhagen, E., Polman, A., Ross, C. E., Lezec, H. J., Atwater, H. A., "Direct Imaging of Propagation and Damping of Near-Resonance Surface Plasmon Polaritons Using Cathodoluminescence Spectroscopy," *Appl. Phys. Lett.* **2006,** *88*, 221111.
- Verhagen, E., Kuipers, L., Polman, A., "Enhanced Nonlinear Optical Effects with a Tapered Plasmonic Waveguide," *Nano Lett.* **2007,** *7*, 334.
- Vesseur, E. J. R., de Waele, R., Lezec, H. J., Atwater, H. A., de Abajo, F. J. G., Polman, A., "Surface Plasmon Polariton Modes in a Single-Crystal Au Nanoresonator Fabricated Using Focused-Ion-Beam Milling," *Appl. Phys. Lett.* **2008,** *92*, 083110.
- Vieu, C., Carcenac, F., Pépin, A., Chen, Y., Mejias, M., Lebib, A., Manin-Ferlazzo, L., Couraud, L., Launois, H., "Electron Beam Lithography: Resolution Limits and Applications," *Appl. Surf. Sci.* **2000,** *164*, 111.
- Volkert, C. A., Minor, A. M., "Focused Ion Beam Microscopy and Micromachining," *MRS Bull.* **2007,** *32*, 389.
- Weber, M. J., *Handbook of Optical Materials*. CRC Press: Boca Raton, 2003.
- West, P. R., Ishii, S., Naik, G. V., Emani, N. K., Shalaev, V. M., Boltasseva, A., "Searching for Better Plasmonic Materials," *Laser Photonics Rev.* **2010,** *4*, 795.
- Wild, B., Cao, L., Sun, Y., Khanal, B. P., Zubarev, E. R., Gray, S. K., Scherer, N. F., Pelton, M., "Propagation Lengths and Group Velocities of Plasmons in Chemically Synthesized Gold and Silver Nanowires," *ACS Nano* **2012,** *6*, 472.
- Wiley, B. J., Lipomi, D. J., Bao, J., Capasso, F., Whitesides, G. M., "Fabrication of Surface Plasmon Resonators by Nanoskiving Single-Crystalline Gold Microplates," *Nano Lett.* **2008,** *8*, 3023.
- Woollam, J. A., Johs, B., Herzinger, C. M., Hilfiker, J., Synowicki, R., Bungay, C. L., "Overview of Variable Angle Spectroscopic Ellipsometry (VASE), Part I: Basic Theory and Typical Applications," *SPIE Proc.* **1999,** *CR72*, 3.

- Zhu, J., Hsu, C.-M., Yu, Z. F., Fan, S. H., Cui, Y., "Nanodome Solar Cells with Efficient Light Management and Self-Cleaning," *Nano Lett.* **2010,** *10*, 1979.

Appendix A.

Ultrasmooth Single-Crystalline Silver Films

Plasmonic devices exploit hybrid photon-electron waves propagating along a metallic surface known as surface plasmon polaritons (SPPs). Manipulating SPPs is feasible when using metallic structures prepared by patterning thin metallic films. However, typically these films are polycrystalline, consisting of many small randomly oriented grains. The grain structure in a metallic film can frustrate the quality of the fabricated patterns and thus can deteriorate the performance of the resulting devices. To address this issue, we provided a simple route to obtain smooth single-crystalline films by sputter deposition of silver onto mica substrates at elevated temperatures (chapter 3). However, the surface roughness of the prepared films could still be improved. In this study, the deposition conditions for single-crystalline silver films were optimized to obtain even smoother surfaces. As a result, extremely small surface roughness of 0.2 nm could be achieved under controlled deposition conditions (deposition rate: 18 Å/s, dc power: 470 W, Ar pressure during deposition: 6 mTorr, substrate temperature: 370 ºC, and source-to-substrate distance: 17 cm). We realized that pre- and post-annealing of the films are very helpful to decrease the surface roughness. Compared to our previous films, the new single-crystalline silver films showed improved dielectric functions, leading to an expected increase in SPP propagation length.

In chapter 3, smooth single-crystalline films were obtained by epitaxial growth of silver on mica substrates at high temperatures.[1] However, since the prepared films exhibited larger root mean square (RMS) roughness (0.8 nm) than the films obtained via other fabrication methods, for example, template stripping (0.35 nm),[2] we tried to find better deposition conditions for single-crystalline films to decrease the roughness. The previous single-crystalline films were deposited under the following conditions (deposition rate: 16.5 Å/s, dc power: 250 W, Ar pressure during deposition: 6 mTorr, substrate temperature: 350 ºC, and source-to-substrate distance: 18 cm). Initially, we thought that a higher deposition rate is desirable to make surfaces smoother. Therefore, we increased the deposition rate by decreasing the source-to-substrate distance and increasing the sputtering power. When utilizing a distance of 13 cm and dc power of 470 W, we could obtain a much faster deposition rate of 33 Å/s compared to the previous conditions. Then, we prepared 200-nm-thick silver films at various substrate temperatures and observed their surface morphology with atomic force microscopy (AFM).

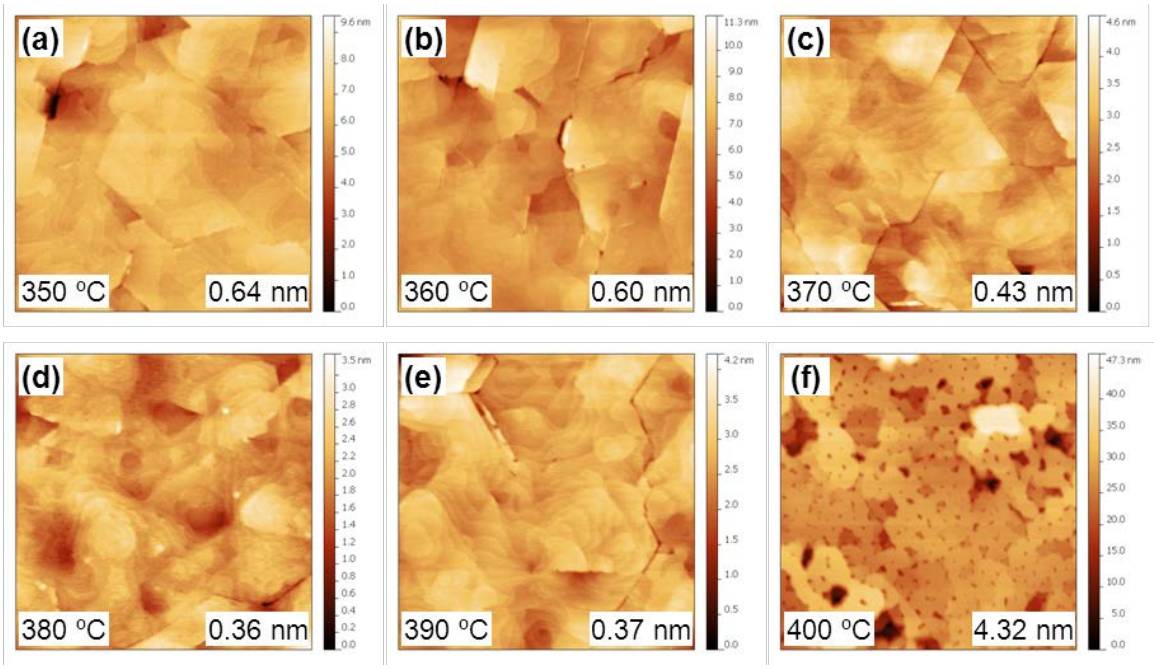

Figure A.1 AFM images of single-crystalline silver films grown on mica substrates at various substrate temperatures. (a) 350, (b) 360, (c) 370, (d) 380, (e) 390, and (f) 400 ºC. All films are 200 nm thick and the deposition rate is 33 Å/s. All scanned areas are 2.5 × 2.5 μm^2 and each image includes the extracted RMS roughness from the areas.

Figure A.1 shows the AFM images of the single-crystalline films. All films except the one from 400 ºC showed reduced surface roughness. In particular, the films from 380 or 390 ºC had roughness below 0.4 nm. Considering that their thickness (200 nm) is thicker than the previous films (100 nm), the improvement in surface roughness is remarkable. However, these films contained undesirable deep trenches on the surfaces (distinctly observed at figure A.1b, A.1c, and A.1e). Unfortunately, the trenches were hard to remove from the films prepared with this deposition rate.

The deposition rate was adjusted by changing the source-to-substrate distance. We realized that when using a distance of 17 cm and a deposition rate of 18 Å/s, the trenches nearly disappear while the surface roughness is still low (0.42 nm for the films from 350 ºC). To remove thoroughly the trenches and to obtain smoother surfaces, we introduced pre- and post-annealing processes.[3-4] For pre-annealing, each mica substrate

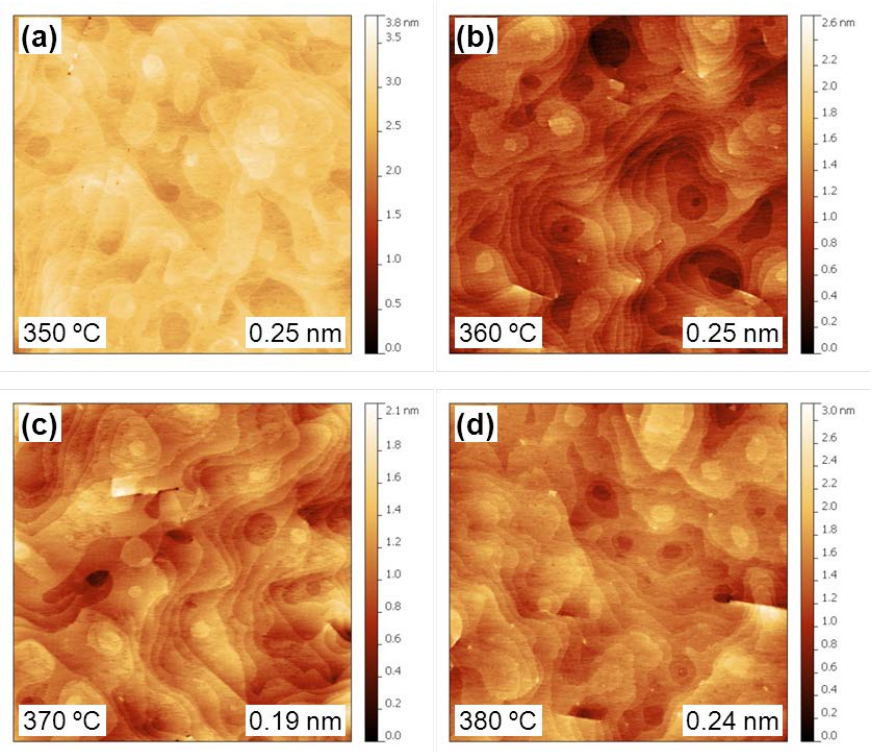

Figure A.2 AFM images of single-crystalline silver films grown on mica substrates at various substrate temperatures with pre- and post-annealing. (a) 350, (b) 360, (c) 370, and (d) 380 ºC. Before and after deposition, the films are annealed at a given temperature for 60 min, respectively. All films are 200 nm thick and the deposition rate is 18 Å/s. All scanned areas are 2.5 × 2.5 μm^2 and each image includes the extracted RMS roughness from the areas.

was heated at a given temperature (350, 360, 370, or 380 ºC) under high vacuum (10^{-6} Torr) for 60 min to remove impurities on the surfaces including adsorbed water molecules. After silver deposition, the films were annealed again for 60 min to make the surfaces smoother. During the pre-annealing, silver deposition, and post-annealing processes, the substrate temperature was constant. The resulting films exhibited extremely flat surfaces without any trenches (figure A.2). Their surface roughness was about 0.2 nm which is smaller than the template-stripped films.[2] The crystalline structure of the films was characterized with X-ray diffraction (XRD). As shown in figure A.3, the films have single-crystalline nature.

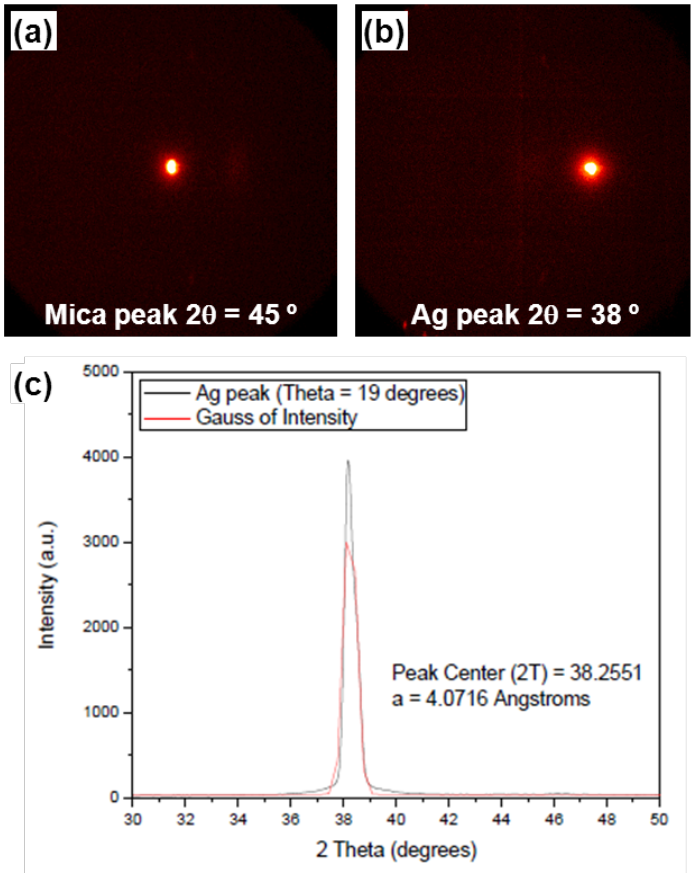

Figure A.3 XRD patterns of a 200-nm-thick c-axis mica/Ag(111) film deposited at 370 °C with pre- and post-annealing. (a) Area-detector image of the highest intensity c-axis mica diffraction peak centered on a 2θ angle of 45° and an X-ray incidence angle of 24.17° (Bragg angle of the mica peak). (b) Area-detector image of Ag(111) peak centered on a 2θ angle of 38° and an X-ray incidence angle of 19.00° (Bragg angle of Ag(111) peak). (c) Integrated XRD pattern of the highest intensity Ag(111) diffraction peak. These XRD data were provided by Palak Ambwani in the Leighton group at the University of Minnesota.

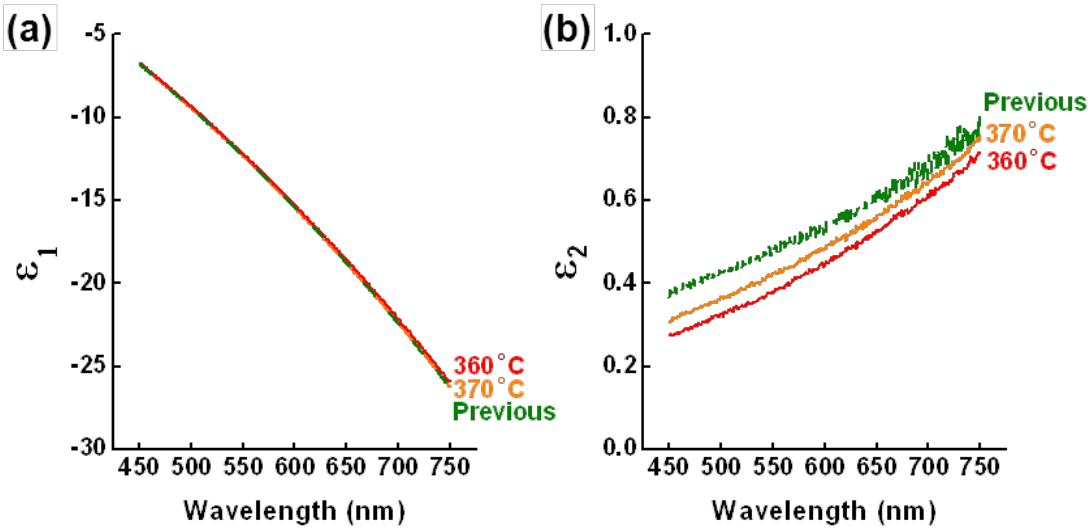

Figure A.4 Real component (a) and imaginary component (b) of the dielectric functions of the new single-crystalline silver films (from 360 and 370 °C) and the previous film (0.8 nm roughness). Polarized incident light in the wavelength range of 450–750 nm was reflected from the films and detected. Three different incidence angles were used: 65, 70, and 75°. The dielectric functions were fitted using numerical iteration and the Fresnel equations.

The dielectric functions of the single-crystalline silver films were measured with ellipsometry. Figure A.4 shows the real and imaginary component of the dielectric functions. Compared to the previous film with roughness of 0.8 nm,[1] new single-crystalline silver films exhibit the almost same real component but smaller imaginary component. This is consistent with our previous results.[2] While the real part is less sensitive to the surface roughness, the imaginary part is largely affected by the roughness. Since the smaller imaginary part implies less optical loss in the films, surface plasmon polaritons (SPPs) in the new films can propagate longer than those in the previous films. Interestingly, in spite of larger roughness, the film from 360 ºC shows a smaller imaginary part than that from 370 ºC. It might be due to the negligible difference in surface roughness between two films (0.06 nm) as well as the influence of possible surface contamination or oxidation during the measurement.

In summary, we found deposition conditions for single-crystalline silver films to further decrease surface roughness. Based on the AFM measurements, the following conditions are desirable to prepare the smoothest surfaces (deposition rate: 18 Å/s, dc

power: 470 W, Ar pressure during deposition: 6 mTorr, substrate temperature: 370 ºC, and source-to-substrate distance: 17 cm). In addition, we proved that pre- and post-annealing processes can improve surface morphology. Under these controlled conditions, extremely flat surfaces with roughnesses of 0.2 nm were obtained. The reduced surface roughness resulted in the improvement in the dielectric functions, leading to an expected increase in the SPP propagation length.

References

[1] J. H. Park, P. Ambwani, M. Manno, N. C. Lindquist, P. Nagpal, S.-H. Oh, C. Leighton, D. J. Norris, "Single-Crystalline Silver Films for Plasmonics," *Adv. Mater.* **2012,** *24*, 3988.

[2] J. H. Park, P. Nagpal, S.-H. Oh, D. J. Norris, "Improved dielectric functions in metallic films obtained via template stripping," *Appl. Phys. Lett.* **2012,** *100*, 081105.

[3] J. A. DeRose, T. Thundat, L. A. Nagahara, S. M. Lindsay, "Gold Grown Epitaxially on Mica: Conditions for Large Area Flat Faces," *Surf. Sci.* **1991,** *256*, 102.

[4] M. H. Dishner, M. M. Ivey, S. Gorer, J. C. Hemminger, F. J. Feher, "Preparation of Gold Thin Films by Epitaxial Growth on Mica and the Effect of Flame Annealing," *J. Vac. Sci. Technol. A* **1998,** *16*, 3295.

Appendix B.
Free-Standing Patterned Films of Refractory Metals

In general, patterned metallic structures for plasmonic applications have been fabricated by two methods, (i) deposition of a metallic layer on a flat substrate followed by patterning or (ii) deposition of a metallic layer on a pre-patterned substrate. However, since the resulting structures from these methods necessarily needed a backing substrate, their applications have been restricted. For example, at high temperatures the metal film can delaminate as shown in chapter 5. To address this issue, we demonstrated that the template-stripping method can provide smooth patterned noble-metal structures as a form of free-standing films. While our recent research showed that template stripping is also applicable to a variety of materials such as refractory metals, semiconductors and oxides (chapter 4), the approach has not yet been utilized to obtain free-standing films of such materials. In this study, we fabricated the free-standing patterned films of refractory metals via template stripping. A ruthenium release layer and a tantalum layer were sequentially deposited on a silicon template. The weak adhesion between the release layer and the template allows stripping the deposited metal layers from the templates. Since the ruthenium release layer is removable by wet etching, tantalum free-standing patterned films could be obtained. We also proved that nickel can be stripped from a silicon template without any release layer and thus nickel free-standing patterned films can be prepared by electroplating on the template and following stripping. The tantalum and nickel structures on the free-standing films showed smooth surfaces and precisely patterned dimensions which are desirable for manipulating surface plasmon polaritons.

In chapter 5, tailored thermal emission at high temperatures was demonstrated. We showed that surface plasmon polaritons (SPPs) created by thermal excitation can be successfully manipulated and re-radiated with patterned metallic structures. This result implies that SPP engineering can be a promising solution for tailored thermal emission and thereby efficient conversion of thermal energy. However, since conventional metal structures should lie on a backing substrate, their operating temperature has been restricted by the relatively low thermal stability of a substrate or the difference in thermal expansion between a metal layer and a substrate. For example, we annealed tungsten bull's-eye structures on a silicon substrate (prepared in chapter 5) at 1200 ºC for 2 hours under vacuum and then observed their morphology with scanning electron microscopy (SEM). As shown in figure B.1, the tungsten structures collapsed because at high temperatures, the volume of the tungsten layer expanded much more than that of the silicon substrate.[1] In particular, the tungsten layer in the flat region was wrinkled and delaminated from the silicon substrate (figure B.1a). Even though the tungsten layer in the patterned region has a relatively large contact area and thereby stronger adhesion with the substrate, some of the tungsten grains were detached from the structures as well (figure B.1b). Therefore, the patterned metallic structures should not be supported by any substrate. In other words, free-standing patterned films of refractory metals are necessary to enhance the performance of thermal emitters.

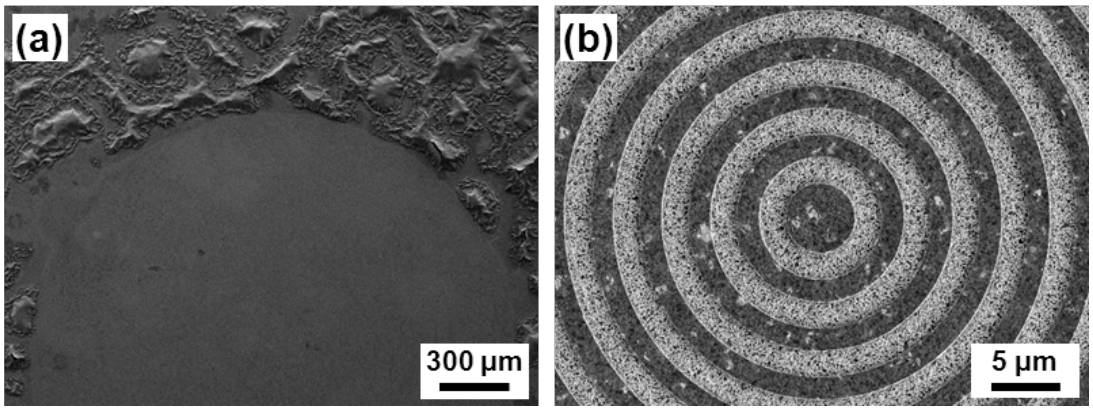

Figure B.1 SEM images of tungsten bull's-eye structures on silicon substrates. The structures were heated at 1200 ºC for 2 hours under vacuum. (a) Low (×50) and (b) high (×3000) magnification images of the structures.

We utilized the template-stripping method to prepare free-standing patterned films of refractory metals[2] because this approach is a low-cost and high-throughput process compared to conventional fabrication methods.[3-4] The key component of the approach is a thin release layer of noble metals between a refractory metal film and a silicon template. Since the surfaces of the template are completely covered with the release layer, the refractory metal film does not touch the template. The weak adhesion between the release layer and the template allows stripping the entire stack of the deposited metal layers. However, we realized that a gold release layer employed in previous research[2] is not suitable for making free-standing films. While the deposited metal should be thick enough to guarantee the mechanical strength of free-standing films, thick films on the gold release layer were spontaneously detached from the template during the deposition. Consequently, an alternative release layer was required which is more adhesive on the template than gold but still strippable. Based on the examination of many noble metals, ruthenium showed the best performance as a release layer for free-standing films.

Tantalum was chosen for a main layer of free-standing patterned films due to the high melting point of about 3000 ºC and the good compatibility with a ruthenium release layer. A 20-nm-thick ruthenium layer and a 20-μm-thick tantalum layer were sequentially deposited on pre-patterned silicon templates via dc magnetron sputtering. Then, the entire stack of the deposited metal layers was peeled off the templates. To avoid deforming the films during stripping, a glucose backing layer was employed. Specifically, glucose was melted on the deposited tantalum layer by heating at 200 ºC and then covered with a glass substrate. Since the melted glucose can act as an adhesive at room temperature, the deposited metal layers can be stripped along with the glass substrate. After stripping, the ruthenium release layer was selectively removed with an aqueous solution containing 0.36 M ceric ammonium nitrate and 0.8 M acetic acid and the glucose layer was dissolved in water. As a result, tantalum free-standing patterned films could be obtained.

Nickel is another attractive material for free-standing patterned films because thick films can be easily obtained via electroplating. In addition, nickel is strippable from a silicon substrate without any release layer. Moreover, nickel is much cheaper and

relatively stable at high temperatures compared to gold and silver. Accordingly, nickel free-standing patterned films will be desirable for a variety of applications including thermal emitters. The free-standing patterned films of nickel were prepared by the following process. First, a 200-nm-thick nickel film was deposited on a pre-patterned silicon template via evaporation. To add a thick nickel layer on the deposited film, electroplating was performed. The nickel film on the template acted as a cathode and a Ti/TiO_2 mesh electrode was employed as an anode. Both electrodes were connected with a DC power supply and then immersed in the electrolyte, an aqueous solution containing 1.08 M nickel(II) sulfamate tetrahydrate, 0.04 M nickel(II) chloride hexahydrate, and 0.65 M boric acid. During electroplating, the electrolyte was gently stirred at 30 rpm and the temperature was maintained at 50 ºC. The distance between the cathode and the anode was fixed at 6 cm and 1.4 A/dm^2 of current density was applied. Electroplating for 80 min produced a 20-μm-thick nickel layer and then nickel free-standing patterned films could be obtained by template stripping.

The surface morphology of the free-standing metal films via template stripping was observed with atomic force microscopy (AFM). Figure B.2 shows the unpatterned areas in the free-standing films of tantalum and nickel. Both films are extremely flat with a root mean square (RMS) roughness below 0.2 nm. The roughness value is smaller than that of conventional stripped surfaces.[2, 5] We believe that these smoother surfaces are resulted from the better wettability of the ruthenium release layer or nickel layer on silicon substrates compared to noble metals. Since the more wettable metals can be more compatible with silicon substrates, the stripped films reveal highly replicated surfaces with silicon substrates, leading to very small roughness of the metal surfaces.

Figure B.3 shows photographs of the free-standing metal films with bull's-eye patterns. We proved that the template-striping method can provide bull's-eye structures of tantalum and nickel as a form of free-standing films without any backing layer (figure B.3b and B.3d). In addition, as shown in figure B.4, the bull's-eye structures on the free-standing films can have smooth surfaces as well as accurate dimensions with nanometer-scale fidelity. These structures will be highly useful to achieve tailored thermal emission (chapter 5).

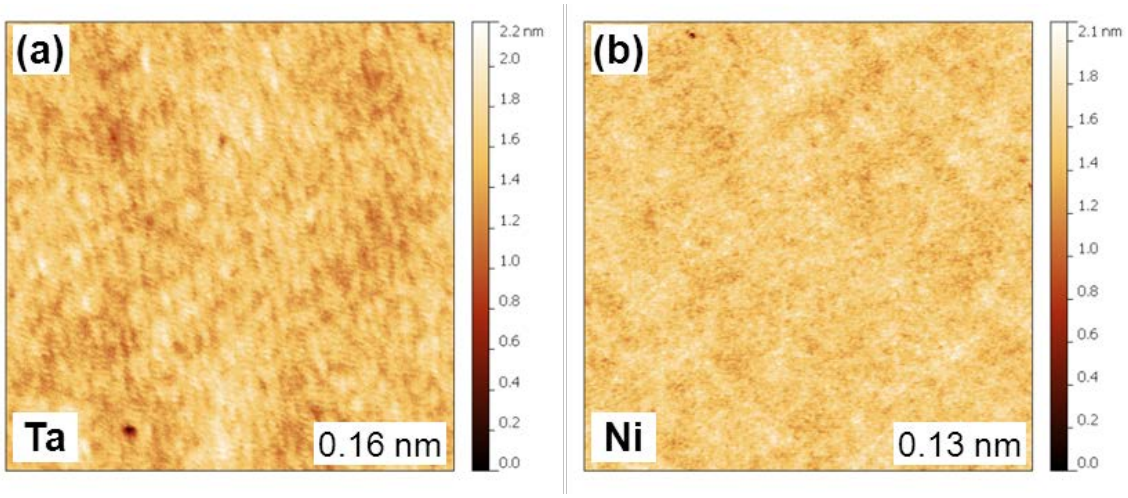

Figure B.2 AFM images of flat surfaces of free-standing metal films prepared by template stripping. (a) Tantalum and (b) nickel films. All scanned areas are 2.5 × 2.5 μm^2 and each image includes the extracted RMS roughness from the areas.

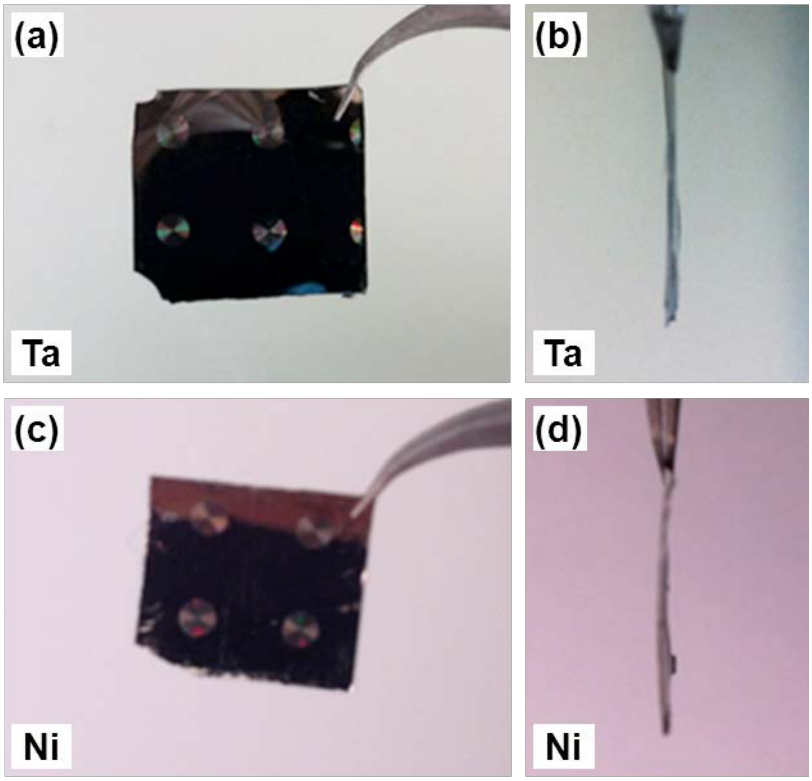

Figure B.3 Photographs of free-standing metal films with bull's-eye patterns prepared by template stripping. (a) Top and (b) side views of the tantalum film. (c) Top and (d) side views of the nickel film. Both films are about 20 μm thick and the diameter of bull's-eye patterns is 2 mm. The films look black because the color of the camera is reflected.

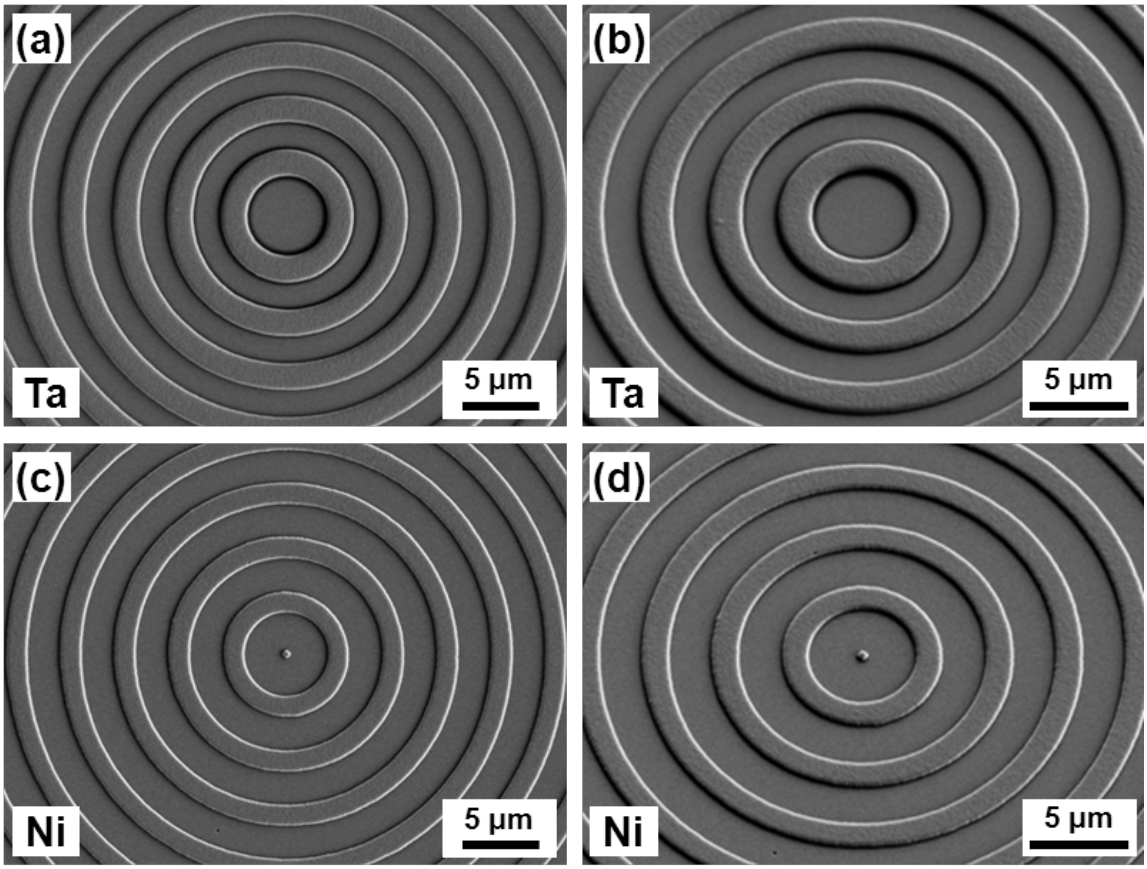

Figure B.4 SEM images of bull's-eye structures on free-standing metal films prepared by template stripping. (a) Top and (b) 30º tilted views of tantalum bull's eyes. (c) Top and (d) 30º tilted views of nickel bull's eyes.

In summary, we demonstrated that free-standing patterned metallic films can be obtained by the template-stripping method. A ruthenium release layer allows tantalum films to be stripped from a silicon template and thus tantalum free-standing patterned films could be prepared. Nickel films deposited on a silicon template via electroplating were readily stripped without any release layer, resulting in nickel free-standing patterned films. The tantalum and nickel films with a thickness of 20 μm were mechanically strong enough to support a form of free-standing films. These films showed extremely flat surfaces in unpatterned areas. Moreover, the bull's-eye structures on the free-standing films exhibited smooth patterns without defects. The free-standing patterned metallic films will be desirable to improve the performance of thermal emitters leading to efficient conversion of thermal energy.

References

[1] D. R. Lide, *CRC Handbook of Chemistry and Physics*. CRC Press: 2012.

[2] J. H. Park, P. Nagpal, K. M. McPeak, N. C. Lindquist, S.-H. Oh, D. J. Norris, "Fabrication of Smooth Patterned Structures of Refractory Metals, Semiconductors, and Oxides via Template Stripping," *unpublished*.

[3] S. Y. Lin, J. Moreno, J. G. Fleming, "Three-Dimensional Photonic-Crystal Emitter for Thermal Photovoltaic Power Generation," *Appl. Phys. Lett.* **2003,** *83*, 380.

[4] S.-Y. Lin, J. G. Fleming, I. El-Kady, "Experimental observation of photonic-crystal emission near a photonic band edge," *Appl. Phys. Lett.* **2003,** *83*, 593.

[5] P. Nagpal, N. C. Lindquist, S.-H. Oh, D. J. Norris, "Ultrasmooth Patterned Metals for Plasmonics and Metamaterials," *Science* **2009,** *325*, 594.